CWP-495
December 2004

Processing and inversion of mode-converted waves using the PP+PS=SS method

Pawan Dewangan

— Doctoral Thesis —

Geophysics

Defended on November 30, 2004

Committee Chair:	Prof. John Warme
Advisor:	Prof. Ilya Tsvankin
Committee members:	Prof. Ken Larner
	Prof. Tom Davis
	Prof. Luis Tenorio

Center for Wave Phenomena
Colorado School of Mines
Golden, Colorado 80401
(1) 303 273-3557

Abstract

Multicomponent seismic is an effective technology for risk reduction in exploration and development. In an exploration setting multicomponent measurements offer improved imaging, direct hydrocarbon and lithology indication, and multiple attenuation over conventional P-wave seismic. Processing of converted (PS) waves currently adopted by the exploration industry is essentially based on resorting PS data into common-conversion-point (CCP) gathers and using them for velocity analysis. Here, I show that PS-waves can be recompiled into the so-called pseudo-shear (ΨS) waves by integrating specially designed convolutions of PP and PS traces (the so-called PP+PS=SS method). Conventional velocity analysis applied to the constructed ΨS data results in an effective SS-wave velocity model because ΨS-waves possess the kinematics of pure shear-wave primaries. This method helps to avoid such complexities of converted waves as moveout asymmetry, reflection-point dispersal, and polarity reversal.

While the replacement of converted waves with pure-mode SS reflections is convenient for processing purposes, it removes the PS-wave moveout asymmetry that may carry useful information for parameter estimation. Therefore, I modified the PP+PS=SS method by supplementing the output SS traces with the moveout asymmetry attributes of PS-waves. The importance of including the PS-wave asymmetry attributes in anisotropic velocity analysis is demonstrated for two typical transversely isotropic models with a tilted symmetry axis (TTI). The first model is a horizontal TTI layer, and the second is a dipping TI layer with the symmetry axis orthogonal to the bedding. The inversion algorithm combines the asymmetry attributes of the PSV-wave with the pure-mode attributes (NMO velocities, zero-offset traveltimes, and reflection slopes) to estimate the model parameters. The numerical and physical-modeling examples show that 2D measurements of the PS-wave asymmetry attributes can help to reconstruct the TTI model in depth using only surface reflection data. The proposed algorithm is also extended to a multilayered model by devising a layer-stripping technique for PS-waves.

Table of Contents

Acknowledgments

I am grateful to my advisor, Dr. Ilya Tsvankin, for providing the opportunity to work on this challenging and difficult problem. I am thankful to all my committee members, Dr. Ken Larner, Dr. John Warme, Dr. Tom Davis, and Dr. Luis Tenorio, for their generous support. I would like to extend my thanks to the Center for Wave Phenomena (CWP) for financial support. The reviews by Ilya and Ken have improved the quality of the thesis.

I appreciate the assistance of Dr. Vladimir Grechka (Shell) with whom I worked on my first comprehensive project on 3D VSP. I would like to thank Dr. Max Peeters and Dr. David Wright (USGS) for helping me to tackle the problem of ground penetrating radar in a borehole environment as my second comprehensive project.

Many thanks to Joe Dellinger (BP) and Helmut Jakubowicz (Veritas) for suggesting the idea of convolution approach to the PP+PS=SS method at the CWP meeting in 2001. I am grateful to members of the PSDM team at Bellaire Technology Center (Shell) and to members of the A(nisotropy)-Team at CWP for their helpful discussions. I thank Vladimir Grechka, Adam Chow and Jon Sheiman (all Shell) for their help with the field data discussed in the thesis.

The presented experimental work was done in the Institute for Experimental Geophysics (IEG). The experimental work was supported by the National Science Foundation (EAR-0111804, EAR-0337379) and the Army Research Office (DAAG55-98-1-0277,DAAD19-03-1-0292). I would not have been able to complete the work without the help of Dr. Mike Batzle, who assisted me with building the model and conducting the experiment. The support by Dr. Kasper van Wijk in collecting the laboratory data is highly appreciated. Kasper stood beside me as both a friend and a mentor during the entire project. I would like to thank Matt Haney, who brought a new perspective to the project through his numerical modeling by the Spectral Element Method.

Graduate studies at CSM would not have been fun without my friends, Alison Malcolm, Yaping Zhu, Dongjie Cheng, Ivan Vasconcelos, David Eckert, Matt Reynolds, Ramzy Al-Zayer, Huub Douma, Xiaoxia Xu, Jyoti Behura, Kumar Gautam, Kurang Mehta, and the Geophysics community at Mines. I am in debt to Michelle Szobody, Lela Webber, Barbara McLenon, and Sara Summers for their help. The life in Golden would be boring without my friends at CSM, especially Rajinder Pal Singh, Arvind Gupta, Praveen Jha, Gaurav Gupta, and Ananth Srinivasan. I would also like to thanks my batch mates Dhananjay Kumar and Priyank Jaiswal (IIT Kharagpur) for discussions of Geophysics and philosophy.

Finally, I would to thank my parents for their unwavering support and my girlfriend Aarti Mehar for her patience during my stay at CSM.

Chapter 1

Introduction

Conventional surface seismic surveys record only compressional, or P-waves. Multicomponent seismic surveys record both P-waves and converted (PS) waves, which is achieved by recording all components of the returning wavefield. P-waves are detected primarily by the vertical Z-component geophone and the hydrophone in marine settings, while PS-waves are detected primarily by the horizontal X- and Y-component geophones. Due to the relatively high cost and often poor quality of SS-wave data excited on land and the absence of shear sources for marine surveys, converted waves are often used to infer shear-wave velocities in the subsurface.

Multicomponent seismic technology can be applied to many seismic and geological challenges, including:

- Strong P-wave multiples: The combination of the signals recorded by the hydrophone and the Z-component geophone can help to reduce water-borne multiple contamination.

- Fracture density and orientation: As a result of S-wave anisotropy S-waves usually split into two waves, a fast and a slow mode, these split S-waves are very sensitive to fractures and can provide information about fracture density (fracture porosity) and orientation (directions of preferred permeability).

- Gas seepages: P-wave reflections may be disturbed by gas leakage in the subsurface. S-waves can be used to help clarify the subsurface image because they are unaffected by pore fluids, an important attribute that can improve seismic imaging and highlight information valuable for reservoir characterization, reservoir monitoring, and well planning.

- Direct hydrocarbon and lithology indication: S-waves can provide valuable insights into the nature of subsurface lithologies and pore-saturating fluids, highlighting reservoirs not previously visible using only P-waves.

Processing of reflection PS data, however, is not straightforward. Here, I discuss some complications involving processing of mode-converted waves and the so-called "PP+PS=SS" method (Grechka & Tsvankin, 2002b) designed to replace PS-waves with pure-mode SS reflections.

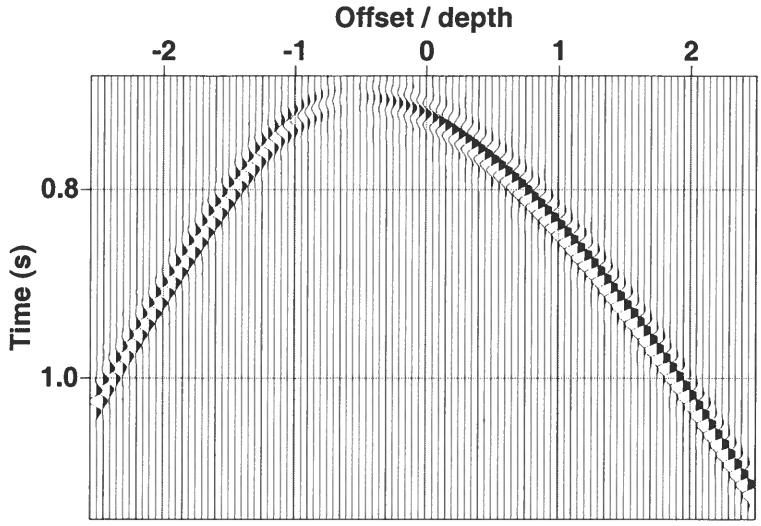

Figure 1.1. CMP gather of PS-waves in a laterally homogeneous, horizontal TTI layer.

1.1 Problem in processing of PS-waves

The main obstacle that precludes applying conventional velocity-analysis techniques to converted waves is the asymmetry of PS-wave reflection moveout on common-midpoint (CMP) gathers (e.g., Thomsen, 1999). If the medium is either laterally heterogeneous or anisotropic without a horizontal symmetry plane, the traveltime of PS-waves does not remain the same when the source and receiver are interchanged (Pelissier et al., 1991; Thomsen, 1999; Tsvankin & Grechka, 2000). For example, PS-wave moveout becomes asymmetric in a laterally homogeneous, horizontal TTI layer (Figure 1.1). As a consequence, neither a hyperbolic nor nonhyperbolic moveout equation routinely used for moveout correction of P-waves generally will flatten PS data. Therefore, any technique designed for velocity estimation from reflected PS-waves should take into account the presence of odd terms in offset in the moveout equations. This invariably complicates the moveout-estimation procedure for converted waves compared to that for pure modes and decreases its robustness in the presence of noise. PS-wave processing is further compounded by polarity reversal (Figure 1.1) and reflection (or conversion) point dispersal – phenomena that are far less common for conventional P-waves.

1.2 PP+PS=SS method: A possible solution

Grechka & Tsvankin (2002b) proposed a solution to the above problems. Their "PP+PS=SS" method uses traveltime picks of reflected PP and PS primaries from se-

lected horizons to reconstruct the traveltimes of the corresponding pure shear (SS) waves. Since the obtained SS-wave moveout is symmetric on CMP gathers, conventional velocity analysis can be applied to them. Implementation of the original, kinematic version of the method has two key elements: identifying PP and PS events reflected from the same interfaces (which requires only indirect velocity information) and picking traveltimes from PP and PS prestack data.

In Chapter 2, I show that the PP+PS=SS method can be implemented without time picking. Although the interpretive step of establishing the correspondence of PP and PS events cannot be avoided, traveltime picking can be replaced with a specially designed convolution of the original PP and PS traces. The resulting data, which I call *pseudo-shear* (ΨS) wave, have the kinematics of pure SS-wave primaries and, therefore, represent an appropriate input for conventional velocity analysis. The proposed technique allows one to generate ΨS-waves from reflection PP and PS data in an automatic fashion and apply the existing velocity-analysis tools devised for pure modes.

After formulating this procedure, I examine its performance on synthetic and field data. In particular, I demonstrate that the method is robust in the presence of random noise. Application of this technique to a 2D multicomponent line acquired in the Gulf of Mexico indicates the presence of anisotropy, thus requiring building of at least a VTI (transversely isotropic with a vertical symmetry axis) velocity model. Although the narrow-azimuth nature of the data and the absence of substantial dip leads to a family of kinematically equivalent subsurface models (Grechka et al., 2002a,b), none of them can be isotropic.

1.3 Asymmetry of PS-waves and its application for parameter estimation

While replacing PS-waves with pure SS reflections is advantageous from the processing viewpoint, the PP+PS=SS method does not preserve the information about the asymmetry of PS moveout. This moveout asymmetry of PS reflections was shown by Tsvankin & Grechka (2000, 2002) to provide critically important attributes for parameter estimation in a VTI media. In the PP+PS=SS method (Grechka & Tsvankin, 2002b), however, the traveltime of the constructed SS arrival for each source-receiver pair is obtained from the *sum* of the "reciprocal" PS-wave times corresponding to same reflection point. (By "reciprocal" times I mean the times of the PS-waves that have the same absolute value but opposite signs of the projection of the slowness vector onto the reflector.) As a result, the *difference* between the reciprocal times, which quantifies the moveout asymmetry, does not contribute to the computed SS data and cannot be used in the subsequent velocity analysis.

In Chapter 3, I demonstrate that supplementing the output of the PP+PS=SS method (i.e., PP and SS data) with the moveout asymmetry attributes of PS-wave data can help to build an anisotropic velocity field in the depth domain without *a priori* information. I consider the model of a horizontal transversely isotropic layer with a tilted symmetry axis (TTI), which describes, for example, obliquely dipping, rotationally invariant fractures embedded in isotropic host rock. Other examples of subsurface TTI formations include progradational clastic or carbonate sequences (e.g., Sarg & Schuelke, 2003) and dipping shale layers in fold-and-thrust belts (e.g., in the Canadian Foothills) and near salt domes.

Another possible reason for the PS-wave moveout asymmetry is lateral heterogeneity

in the form of lateral velocity variations or dipping reflectors. For example, PS move-out becomes asymmetric even in an isotropic or VTI layer above a plane dipping reflector (Tsvankin & Grechka, 2000, 2002). In active tectonic areas, originally horizontal TI layers are often rotated such that the symmetry axis remains orthogonal to the layer boundaries. Dipping shale layers of this type are commonly observed in the fold-and-thrust region of the Canadian Foothills (e.g., Isaac & Lawton, 1999) and near salt domes (Tsvankin, 2001). Ignoring anisotropy in dipping TTI beds can cause significant mispositioning of reflection events in both vertical and horizontal directions (Isaac & Lawton, 1999; Vestrum et al., 1999; Lawton et al., 2001). Although migration algorithms can be readily extended to TTI media, accurate estimation of the required anisotropic parameters for imaging purposes remains a difficult problem. In Chapter 4, I extend the methodology introduced in Chapter 3 to the inversion of multicomponent (PP and PSV) data acquired above a TTI layer with the symmetry axis orthogonal to the layer's bottom. Chapter 4 discusses simple analytic approximations for the asymmetry factors of the PSV-wave and demonstrates that independent information for the inversion is contained in higher-order terms in offset.

1.4 Physical modeling and layer stripping

In order to verify the parameter-estimation algorithm introduced in Chapter 3, I conduct a physical modeling experiment. The material used to simulate the TTI medium is XX-paper-based phenolic. Chapter 5 demonstrates on a physical model that PP and PS data indeed constrain all the model parameters in a horizontal TTI layer. The inverted model is validated by comparison with the results of a transmission experiment.

In Chapter 6, I show that the interval asymmetry attributes of PS-wave can be obtained from the effective ones for a layer-cake model and for a model with a dipping interface beneath a stack of laterally homogeneous layers. The proposed layer-stripping technique works with the traveltimes rather than NMO velocities and is exact for all offsets. It can also be used to extract interval traveltime and offset for pure modes. I also obtain the small-offset approximation for the time asymmetry in heterogeneous, arbitrarily anisotropic media and derive a constraint on pure-mode attributes (zero-offset traveltimes and reflection slopes) for a homogeneous layer above a planar reflector (the incidence plane is assumed to coincide with a vertical symmetry plane of the model). These theoretical results will become important for extending the proposed parameter-estimation algorithm to lower-symmetry anisotropic media.

Chapter 2

Full-waveform version of the PP+PS=SS method

2.1 Overview of the PP+PS=SS method

A natural starting point for my development is the kinematic formulation of the PP+PS=SS method (Grechka & Tsvankin, 2002b). Figure 2.1 shows PP and PS ray trajectories identified by the method from 2D split-spread PP and PS reflection data. Three rays $\left(x^{(1)}Rx^{(2)},\ x^{(1)}Rx^{(3)},\ \text{and}\ x^{(2)}Rx^{(4)}\right)$ have exactly the same reflection point R when the PP and PS reflection slopes coincide at the P-wave source and receiver locations $x^{(1)}$ and $x^{(2)}$. Since the slope $p(x^{(s)}, x^{(r)})$ measured at the source location $x^{(s)}$ on the common-receiver gather located at $x^{(r)}$ is

$$p(x^{(s)}, x^{(r)}) = \frac{\partial t(x^{(s)}, x^{(r)})}{\partial x^{(s)}} \tag{2.1}$$

for any reflection mode, the requirement of equal PP and PS slopes yields

$$\frac{\partial t_{PP}(x^{(1)}, x^{(2)})}{\partial x^{(1)}} = \frac{\partial t_{PS}(x^{(1)}, x^{(3)})}{\partial x^{(1)}} \tag{2.2}$$

and

$$\frac{\partial t_{PP}(x^{(2)}, x^{(1)})}{\partial x^{(2)}} = \frac{\partial t_{PS}(x^{(2)}, x^{(4)})}{\partial x^{(2)}}\,. \tag{2.3}$$

Here t_{PP} and t_{PS} are the traveltimes of PP- and PS-waves, $x^{(j)}$ $(j = 1, 2, 3, 4)$ denote the source and receiver coordinates, and

$$t_{PP}(x^{(1)}, x^{(2)}) = t_{PP}(x^{(2)}, x^{(1)})$$

due to reciprocity. The construction in Figure 2.1 produces the traveltime of the pure-S reflected ray, $x^{(3)}Rx^{(4)}$,

$$t_{SS}(x^{(3)}, x^{(4)}) = t_{PS}(x^{(1)}, x^{(3)}) + t_{PS}(x^{(2)}, x^{(4)}) - t_{PP}(x^{(1)}, x^{(2)})\,. \tag{2.4}$$

Clearly, one needs to pick prestack reflection traveltimes t_{PS} and t_{PP} along a selected horizon to calculate t_{SS} from equations (2.2)–(2.4). Although this is feasible and was shown to work on field data (Grechka et al., 2002b), prestack traveltime picking is tedious, labor-intensive, and noise and error prone. Below, I describe a technique that makes traveltime picking unnecessary and produces seismograms that resemble pure shear-wave reflection data for all horizons.

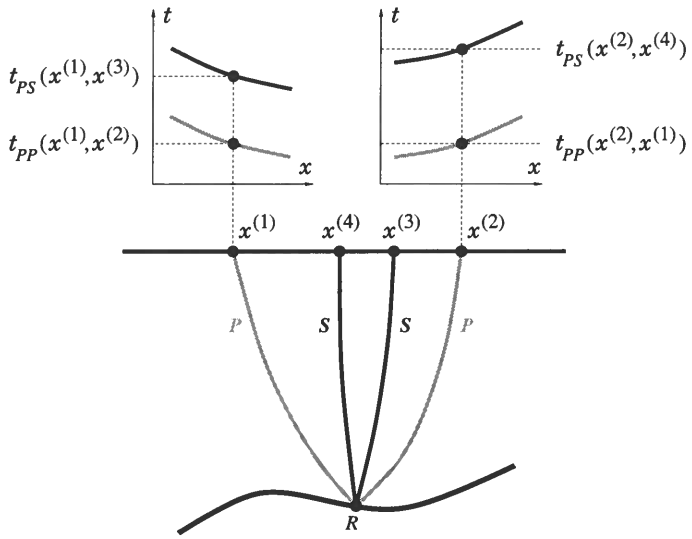

Figure 2.1. Ray diagram of the $PP + PS = SS$ method in 2D (after Grechka & Tsvankin, 2002b).

2.2 Theoretical aspects of generating ΨS data

The traveltime of pure SS-wave data can be reconstructed by combining the traveltime of P-wave data with the mode-converted waves.

2.2.1 General integral expression

Seismogram of ΨS-waves that have the kinematics of SS-wave primaries can be computed from the integral (AppendixA),

$$w_{\Psi S}(t, x^{(3)}, x^{(4)}) = \iint \Big[w_{PS}(t, x^{(1)}, x^{(3)}) * w_{PP}(-t, x^{(1)}, x^{(2)}) * w_{PS}(t, x^{(2)}, x^{(4)}) \Big] \, dx^{(1)} \, dx^{(2)} \, . \tag{2.5}$$

Here w_{PP} and w_{PS} are the PP and PS traces, t is time, and asterisks denote convolutions in time. The PP traces are taken in reverse time because the P-wave time gets subtracted in equation (2.4) to produce the pure-shear time. Integration is performed over the P-wave source and receiver coordinates $x^{(1)}$ and $x^{(2)}$. The result of integration (2.5) is the ΨS trace for the source and receiver located at $x^{(3)}$ and $x^{(4)}$.

Evaluation of integral (2.5) using the stationary phase method (Appendix A) shows that if the traces w_{PP} and w_{PS} consist of PP and PS primaries corresponding to a selected reflector, the trace $w_{\Psi S}$ contains the pure S-wave primary from the same reflector. The fact that the proof in Appendix A is valid only for an isolated interface indicates the necessity for

windowing the input w_{PP} and w_{PS} traces around events of interest. This, in turn, requires establishing the correspondence of PP and PS events prior to evaluating integral (2.5).

2.2.2 Amplitudes of ΨS-waves

Although integral (2.5) produces ΨS data that should have traveltimes of pure S-waves, their amplitudes do not correspond to those of shear-wave primaries. This is immediately clear from equation (2.5). Indeed, the ΨS-wave amplitudes are directly inferred from those of the PP and PS events and are functions of the PP- and PS-wave amplitudes [see equation (2.6)] rather than the pure SS-wave amplitudes. This is not surprising because, as follows from the reciprocity theorem, PP and PS data generally do not contain enough information for reconstructing the true S-wave amplitudes.

This last statement can be illustrated by considering zero-offset PP and PS reflections from a single, sufficiently thick horizontal layer. The amplitude of the reflected P-wave in this model is proportional to the P-wave impedance contrast at the interface, while the amplitude of the converted wave is zero. Clearly, no information about the shear-wave impedance contrast, which governs the amplitude of the pure SS-wave, can be extracted from the zero-offset PP and PS traces.

On the other hand, ΨS-wave amplitudes are obtained in a deterministic way from those of PP and PS reflections. The benefits of using ΨS-waves instead of PS-waves include the simplicity of their moveouts and usually higher signal-to-noise ratio than that of the original PP and PS data (see Figure 2.8 as an example). The amplitude of ΨS-wave can be obtained by evaluating the asymptotic expression for the integral (A.4) due to the contribution of the stationary points ($\boldsymbol{x}_0$):

$$W_{\Psi S}(\omega, x^{(3)}, x^{(4)}) \sim \frac{2\pi}{i\omega\sqrt{|\lambda_1 \lambda_2|}} F_{PS}^2(\omega)\, F_{PP}^{\star}(\omega) \times A_{PS}(x^{(1)}, x^{(3)})\, A_{PP}^{\star}(x^{(1)}, x^{(2)})\, A_{PS}(x^{(2)}, x^{(4)}), \tag{2.6}$$

where ω is radial frequency, A_{PP} and A_{PS} represent the amplitudes of reflected PP- and PS-waves due to the propagation effect, F_{PP} and F_{PS} denote the spectra of their source wavelets, star denotes complex conjugate, and λ_1 and λ_2 are the eigenvalues of the matrix,

$$\Phi_{ij} = \left.\frac{\partial^2 \tau}{\partial x^{(i)}\, \partial x^{(j)}}\right|_{\boldsymbol{x}=\boldsymbol{x}_0}, \tag{2.7}$$

evaluated at the stationary points. Under the assumption that the PP and PS data are corrected for geometrical spreading, the simplified expression for the ΨS-wave amplitudes can be represented as

$$R_{\Psi S}(x^{(3)}, x^{(4)}) \propto R_{PS}(x^{(1)}, x^{(3)})\, R_{PP}^{\star}(x^{(1)}, x^{(2)})\, R_{PS}(x^{(2)}, x^{(4)}), \tag{2.8}$$

where R_{PP} and R_{PS} are the reflection coefficients of the P- and PS-waves from a common reflection point R (Figure 2.1). Note that equation (2.8) is valid for large offsets, where the

reflection coefficients can become complex.

In order to understand the amplitudes of ΨS-waves, I analyze the weak-contrast, small-offset approximation for the ΨS-wave amplitudes in a homogeneous isotropic half-space (Appendix B). Since the output is in SS-wave offset, it is convenient to express the PP- and PS-wave reflection coefficients in terms of S-wave incidence angle, which yields (Appendix B)

$$\begin{aligned} R_{\Psi S} \quad &\approx \quad \left[\frac{1}{8}\left(g\,\frac{\Delta\rho}{\bar{\rho}} + 2\,\frac{\Delta G}{\bar{G}}\right)^2 \frac{\Delta Z}{\bar{Z}}\right] \sin^2 j \\ &+ \quad \frac{\Delta G}{\bar{G}}\,T_{22}\,\sin^4 j + \frac{\Delta G}{\bar{G}}\,T_{33}\,\sin^6 j, \end{aligned} \tag{2.9}$$

where Z, G, and ρ are the values of the P-wave impedance, shear modulus, and density, respectively. The bar and 'Δ' refer to mean value and difference between the properties of the two halfspaces, respectively. The ratio of P-wave velocity to S-wave velocity is denoted by g. Since the higher-order terms in equation (2.9) are proportional to the jump in the shear modulus (ΔG), the amplitudes of ΨS-wave will be linear in $\sin^2 j$ for a small contrast in G.

To test the accuracy of equation (2.9), I obtained the exact (solid lines) PP- and PS-wave reflection coefficients (Aki & Richards, 1980) in a two-layer model with the parameters given in the caption of Figure 2.2. The approximate (dashed lines in Figure 2.2a) PP- and PS- wave reflection coefficients [equations (B.3) and (B.4)] are accurate for small offsets. The ΨS-wave amplitudes (Figure 2.2b), obtained by multiplying the exact PP- and PS-wave reflection coefficients [equation (2.8)] and from the approximation [equation (2.9)] are in good agreement. For anisotropic models, the amplitudes of ΨS-wave become more complicated and difficult to interpret.

2.2.3 Extension to 3D

Similarly to the original $PP + PS = SS$ method of Grechka & Tsvankin (2002b), integral (2.5) can be extended to 3D multiazimuth reflection data. If the sources and receivers are allowed to cover a certain area, their coordinates $\boldsymbol{x} \equiv [x_1, x_2]$ become two-dimensional vectors. The ΨS traces are formally given by the same equation (2.5)

$$\begin{aligned} w_{\Psi S}(t, \boldsymbol{x}^{(3)}, \boldsymbol{x}^{(4)}) = \iiiint \Big[\quad & w_{PS}(t, \boldsymbol{x}^{(1)}, \boldsymbol{x}^{(3)}) * w_{PP}(-t, \boldsymbol{x}^{(1)}, \boldsymbol{x}^{(2)}) * \\ & w_{PS}(t, \boldsymbol{x}^{(2)}, \boldsymbol{x}^{(4)}) \Big]\, d\boldsymbol{x}^{(1)}\, d\boldsymbol{x}^{(2)}, \end{aligned} \tag{2.10}$$

where all $\boldsymbol{x}^{(j)}$ ($j = 1, 2, 3, 4$) become 2D vectors and, therefore, the integration becomes four-fold.

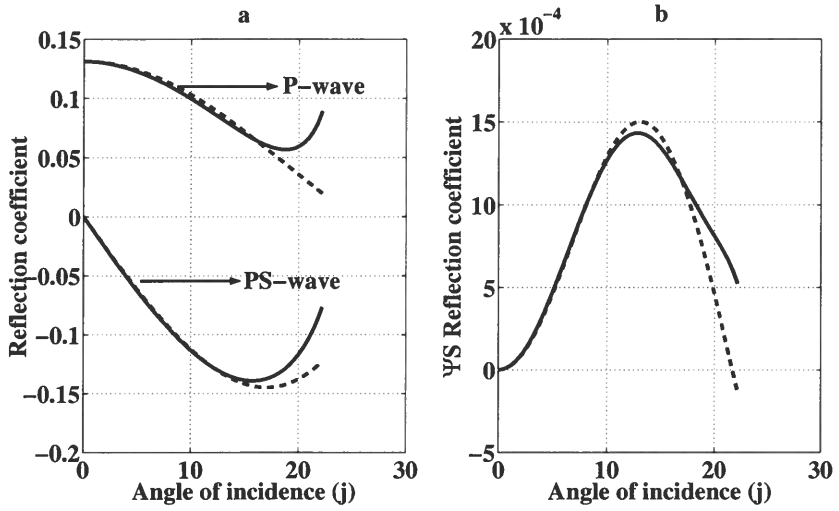

Figure 2.2. Reflection coefficients for an isotropic half-space as a function of the S-wave incidence angle (j). The P-wave velocity, S-wave velocity, and density are 4 km/s, 2 km/s, 2.40 gm/cm^3 for the first layer and 5 km/s, 2.8 km/s, 2.5 gm/cm^3 for the second layer: (a) PP- and PS-wave exact (solid lines) and approximate (dashed lines) reflection coefficients, (b) ΨS-wave exact (solid line) and approximate (dashed line) amplitudes.

2.3 Synthetic examples

Here I present numerical tests that illustrate the above outlined theory for generating ΨS data in 2D. I begin with examining the time function τ [equation (A.5)] whose extrema determine the kinematics of ΨS-waves, then compute integral (2.5) to study features of ΨS-data, and finally analyze the performance of the algorithm in the presence of random noise.

2.3.1 Time function τ

As follows from Appendix A, the ability of integral (2.5) to represent the kinematics of SS-waves depends upon the existence of the roots $x^{(1)}$ and $x^{(2)}$ of equations (A.6). Clearly, the PP and PS data are supposed to be physically recorded at the source and receiver locations $x^{(1)}$ and $x^{(2)}$ to contribute to the integral. Since the number of roots $x^{(1)}$ and $x^{(2)}$ and their very existence are unknown in advance, I present two examples that demonstrate how the procedure might work in practice.

Defining the P-wave half-offset h_{PP} and the midpoint y_{PP} as

$$h_{PP} \equiv \frac{x^{(2)} - x^{(1)}}{2} \quad \text{and} \quad y_{PP} \equiv \frac{x^{(2)} + x^{(1)}}{2},$$

I plot the time functions $\tau(h_{PP}, y_{PP})$ for a plane homogeneous isotropic layer (Figure 2.3).

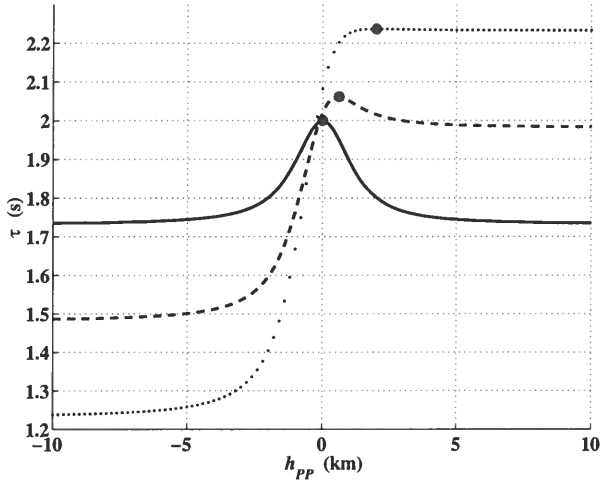

Figure 2.3. Time functions τ in a horizontal homogeneous isotropic layer that has thickness $D = 1$ km and velocities $V_P = 2$ km/s and $V_S = 1$ km/s. The solid line corresponds to ΨS-wave half-offset $h_{\Psi S} = 0$, dashed line to $h_{\Psi S} = 0.25$ km, and dotted line to $h_{\Psi S} = 0.5$ km. Large dots indicate the stationary values of τ.

The PP- and ΨS-wave midpoints, y_{PP} and

$$y_{\Psi S} \equiv \frac{x^{(3)} + x^{(4)}}{2},$$

coincide because the layer is horizontal. As a consequence, the curves in Figure 2.3 were computed for the correct, i.e., stationary values $y_{PP} = y_{\Psi S}$. Figure 2.3 displays two clear maxima[1] of $\tau(h_{PP})$ for ΨS half-offsets $h_{\Psi S} = (x^{(3)} - x^{(4)})/2 = 0$ and $h_{\Psi S} = 0.25$ km (solid and dashed lines), and a poorly defined one for $h_{\Psi S} = 0.5$ km (dotted line). Those maxima, marked with large dots, produce stationary points that yield pure shear-wave reflection traveltimes. This statement can easily be verified by computing the S-wave moveout in this model (the parameters are given in the caption of Figure 2.3).

Note that the curves in Figure 2.3 flatten out at large P-wave half-offsets h_{PP} suggesting that the time function τ has extrema at $h_{PP} \to \pm\infty$. Although these extrema might seem irrelevant for the problem at hand because data are never acquired at infinite offsets, we will see that both the flatness of the time function τ and the finite frequency bandwidth of seismic data lead, unfortunately, to noticeable contributions associated with those distant extrema even at relatively moderate h_{PP}.

The extrema at $h_{PP} \to \pm\infty$ relate to the critical offsets of shear waves (Figure 2.4). The P-wave incident and S-wave reflection angles, θ_P and θ_S, respectively, satisfy Snell's

[1]They are actually saddle points. To show this, one needs to plot $\tau(h_{PP}, y_{PP})$ in the $[h_{PP}, y_{PP}]$ coordinates as done in Figure 2.5 below.

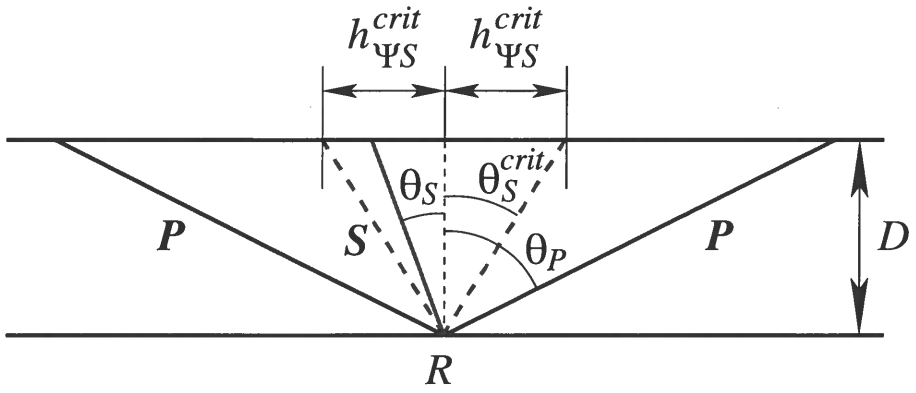

Figure 2.4. Critical ΨS-wave offset ($h_{\Psi S}^{crit}$).

law

$$\frac{\sin\theta_P}{V_P} = \frac{\sin\theta_S}{V_S},$$

where V_P and V_S are the P- and S-wave velocities. Therefore, the maximum reflection angle of shear waves is $\theta_S^{crit} = \sin^{-1}(V_S/V_P)$. This yields the critical half-offset

$$h_{\Psi S}^{crit} = D \tan\left[\sin^{-1}\left(\frac{V_S}{V_P}\right)\right] \tag{2.11}$$

for the simple model in Figure 2.4; D is the layer thickness. Since the P-wave half-offset corresponding to $h_{\Psi S}^{crit}$ is infinite, equation (2.11) establishes a physical limit of the maximum ΨS offset that can be obtained from PP and PS reflection data regardless of the original offsets. Clearly, a low V_S/V_P velocity ratio results in a small spread of the ΨS data, thus increasing the uncertainty of shear-wave velocity analysis. The method introduced here reveals the dependence of the accuracy of the estimated shear-wave velocities on the V_S/V_P ratio, an issue that does not directly follow from direct analysis of converted waves.

Figure 2.3 indicates that waves corresponding to the contributions of the flat areas of the time function $\tau(h_{PP})$ at $h_{PP} \to \pm\infty$ propagate with the P-wave rather than shear-wave velocity because $\theta_S \to \theta_S^{crit}$ = constant for large h_{PP}. For this reason, they can be called the ΨP-waves. Figure 2.3 also shows that the extrema of $\tau(h_{PP})$ corresponding to the ΨS- and ΨP-waves approach each other in a continuous fashion and become indistinguishable for $h_{\Psi S} \to h_{\Psi S}^{crit}$ (dotted line). Since the ΨS and ΨP arrivals have different kinematics, mixing them together (under the improper name ΨS) will invariably lead to errors in the estimated S-wave velocities. The only remedy against that is to restrict the integration in (2.5) to half-offsets $h_{\Psi S} \leq h_{\Psi S}^{crit}$.

Figure 2.5 gives an example of the time function $\tau(h_{PP}, y_{PP})$ for a dipping layer. The stationary (saddle) point corresponding to the ΨS arrival is located at $h_{PP} = 0.5$ km and $y_{PP} = -0.1$ km (the cross in Figure 2.5); the midpoints $y_{\Psi S}$ and y_{PP} are different because of the reflector dip. The flattening of the time function in the bottom corners of Figure 2.5

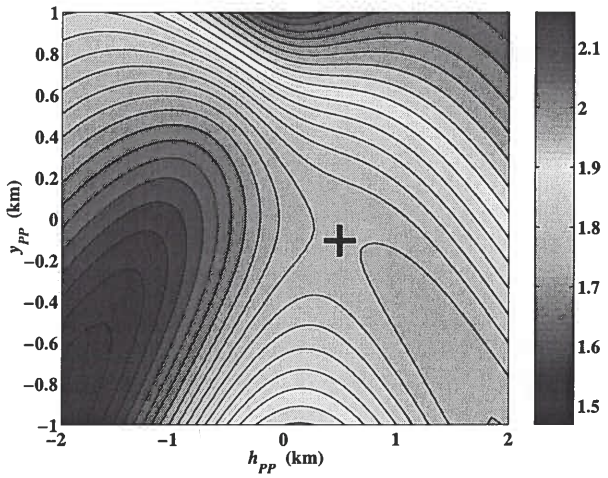

Figure 2.5. Time function $\tau(h_{PP}, y_{PP})$ (in s) for a dipping isotropic layer that has vertical thickness $D = 1$ km (under the coordinate origin $h_{PP} = y_{PP} = 0$), dip $\psi = 30°$ and the same velocities as those in Figure 2.3. The ΨS-wave midpoint and half-offset are $y_{\Psi S} = 0$ and $h_{\Psi S} = 0.2$ km, respectively.

indicates the extrema associated with ΨP-waves.

2.3.2 Common-midpoint (CMP) gathers of ΨS-waves

Because of the flattening, the integration limits in equation (2.5) need to be chosen properly to avoid mutual contamination of ΨS and ΨP data and the convolutions have to be performed within time gates that enforce accurate correlation of PP and PS events. Next, I proceed with actual computation of ΨS seismograms.

Figures 2.6a and 2.6b show the input PP and PS traces of synthetic CMP gathers for a model of three homogeneous, isotropic dipping layer. Figure 2.6c demonstrates the result – a computed ΨS CMP gather. The PP and PS data have the following features:

- PP and PS wavelets differ in both the shape and frequency content; the ratio of the dominant frequencies of the PP- and PS-waves is 1.5.
- The polarity of the reflected PS-waves flips at zero offset.
- The converted-wave moveouts corresponding to dipping reflectors are asymmetric with respect to the source and receiver positions (Figure 2.6b). This phenomenon, as discussed above, precludes application of conventional velocity analysis to PS data.

Figure 2.6c illustrates that the above features, which are usually troublesome for conventional converted-wave processing, do not prevent us from reconstructing useful ΨS data. The observation of primary importance in Figure 2.6c is that the reconstructed ΨS events

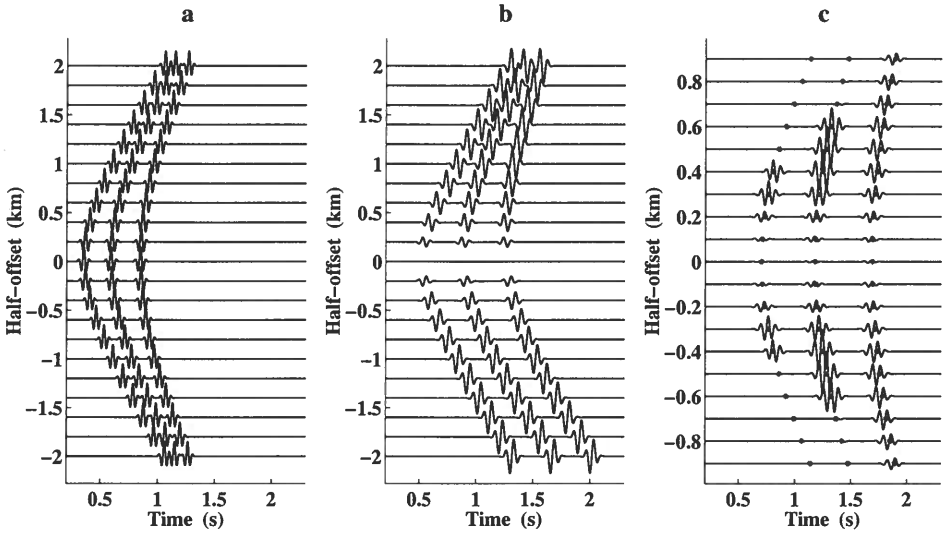

Figure 2.6. Input (a) PP, (b) PS, and (c) generated ΨS CMP gathers. The model is homogeneous and isotropic with $V_P = 4$ km/s and $V_S = 2$ km/s. Three planar reflectors have the depths $D = 0.7$, 1.2, and 1.8 km beneath the CMP; their dips are 0°, 10°, and 20°. The dots indicate the correct SS-wave reflection traveltimes.

follow the correct (i.e., those computed by ray tracing) SS-wave moveouts. Some other features of ΨS are as follows:

- As expected from the nature of convolution in equation (2.5), the ΨS wavelets are longer and have more lobes than do those of either PP- or PS- waves. Their dominant frequency lies between those of the PP- and PS-waves.

- The ΨS CMP gather does not have polarity reversals. This follows from formulation (2.5), which uses PS data twice so that the sign of the PS wavelet cancels out.

- Weak amplitudes of ΨS-waves reconstructed at small offsets relate to the correspondingly weak PS signals. In particular, the PS amplitude is zero at $x^{(1)} = x^{(2)} = 0$. Since this is the stationary point for the output offset $X_{\Psi S} \equiv 2\,h_{\Psi S} = x^{(3)} - x^{(4)} = 0$, the zero-order term of the stationary phase method predicts a vanishing ΨS-wave amplitude. The weak, but finite, ΨS arrivals observed at $h_{\Psi S} = 0$ in Figure 2.6c correspond to the contributions of higher-order terms in the stationary-phase expansion.

- The absence of ΨS-waves at large offsets is a result of limiting integration (2.5) to pre-critical offsets only. Specifically, the algorithm checks the value of $h_{\Psi S}$ and evaluates integral (2.5) only if $h_{\Psi S} \leq h_{\Psi S}^{crit}$; otherwise it fills the output ΨS trace with zeros. The termination points for the two shallow reflections in Figure 2.6c suggest that ΨS-waves can be reconstructed only for offset-to-depth ratios smaller than $X_{\Psi S}/D \approx$

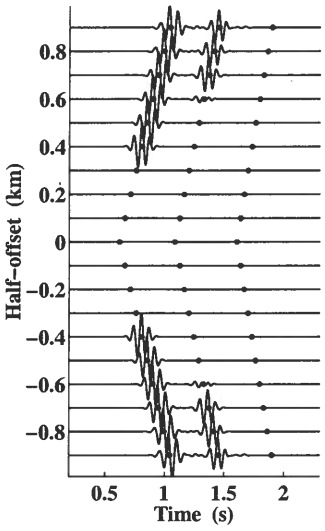

Figure 2.7. CMP gather of ΨP-waves generated from PP and PS data in Figure 2.6. The dots indicate the linear moveout of P-wave.

1. This observation is in agreement with the theoretical result (2.11), which yields $X^{crit}_{\Psi S}/D = 2\,h^{crit}_{\Psi S}/D = 1.15$.

Following the above discussion, one might wonder what happens if the same computation is performed at half-offsets $h_{\Psi S} > h^{crit}_{\Psi S}$. Figure 2.7 shows that in this case the algorithm produces events whose moveouts are approximately linear with the slopes $dt/dh_{\Psi S} \approx 2/V_P$ or $dt/dX_{\Psi S} \approx 1/V_P$. Clearly, their kinematics has nothing to do with that of reflected SS-waves. This explains why these arrivals can be called ΨP-waves. Only the changes in the lengths of the P-wave segments of the converted-wave ray trajectories contribute to the moveouts in Figure 2.7 because the S-wave segments remain constant for any half-offset $h_{\Psi S} > h^{crit}_{\Psi S}$.

Since the ΨP-wave traveltimes are smaller than those associated with ΨS-waves (compare Figures 2.6c and 2.7), mixing the two events together and performing conventional velocity analysis may bias the estimated S-wave velocities towards higher values. As was already mentioned, this bias can be removed by restricting the integration in equation (2.5) to half-offsets $h_{\Psi S} \leq h^{crit}_{\Psi S}$.

2.3.3 Influence of random noise

Since the discussed procedure is designed for field data, it is important to examine its robustness with respect to noise. Figures 2.8a and 2.8b show PP and PS traces similar to those in Figures 2.6a and 2.6b but contaminated with Gaussian noise that has standard deviation equal to the maximum amplitude in the data. Even though the PP and PS reflections are barely recognizable in Figures 2.8a and 2.8b, Figure 2.8c displays remarkably clean

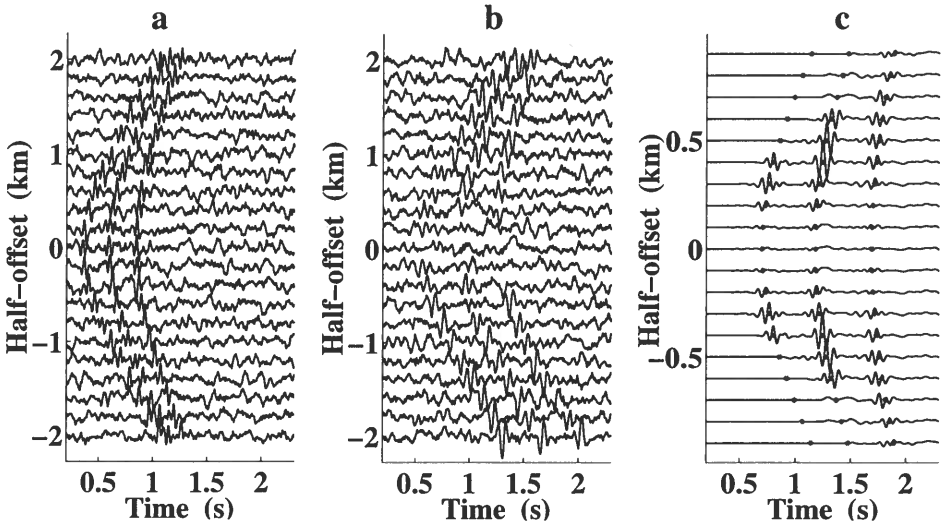

Figure 2.8. Same as Figure 2.6 but for PP and PS data contaminated with Gaussian noise that has signal-to-noise ratio equal to 1. Dots indicate correct S-wave reflection traveltimes.

ΨS traces. This result is a direct consequence of applying convolutions, which efficiently attenuate random noise.

2.4 Gulf of Mexico case study

The methodology was applied to a multicomponent (hydrophone, vertical geophone, and inline horizontal geophone) 2D line acquired in the Gulf of Mexico. First, the PP-to-PS event correspondence was established. This gave us the relationship between the PP and PS zero-offset times, t_{PP0} and t_{PS0}, which were used to compute the shear-wave traveltimes t_{SS0} and the ratios g_0 as

$$g_0(t_{PP0}) \equiv \frac{t_{PP0}}{t_{SS0}} = \frac{t_{PP0}}{2\,t_{PS0} - t_{PP0}}. \tag{2.12}$$

Because of mild lateral heterogeneity of the subsurface, both functions $t_{SS0}(t_{PP0}, Y)$ and $g_0(t_{PP0}, Y)$ [Figure 2.9] have a relatively weak dependence on the CMP coordinate Y.

An important observation that can be made from Figure 2.9b is that the ratio g_0 is quite small (about 0.15) at shallow depths. Ignoring the possible presence of anisotropy, reflector dip, and lateral heterogeneity, and using the value of $g_0 = V_S/V_P = 0.15$ to estimate the critical ΨS-wave offset-to-depth ratio from equation (2.11), I find $X^{crit}_{\Psi S}/D = 2\,h^{crit}_{\Psi S}/D \approx 0.3$. Clearly, shear-wave stacking velocities cannot be picked accurately from such short-spread moveouts. The ratio g_0, however, rapidly increases with depth, reaching the value of $g_0 = 0.35$ at $t_{PP0} \approx 5.5$ s. This yields the ratio $X^{crit}_{\Psi S}/D \approx 0.75$ which makes the results of ΨS-wave velocity analysis substantially more reliable despite the influence

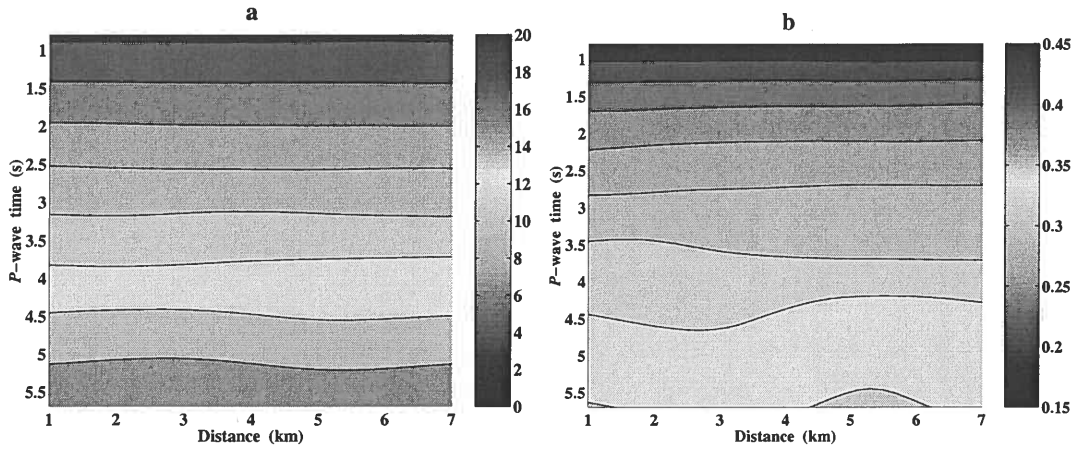

Figure 2.9. Event correlation displayed through (a) the function $t_{SS0}(t_{PP0}, Y)$ and (b) the ratio $g_0(t_{PP0}, Y)$. Here, t_{SS0} and t_{PP0} are the S- and P-wave two-way zero-offset times (in s), respectively, and Y is the distance (in km) along the line (or the CMP coordinate). The color bars refer to the values of t_{SS0} (a) and g_0 (b).

of growing shear-wave velocity $V_S(t_{SS0})$, which tends to reduce the accuracy of velocity picking.

Figure 2.10, which displays the generated ΨS data, confirms a rapid increase of the maximum ΨS-wave offset with time t_{SS0}. Velocity analysis performed on ΨS-wave CMP gathers such as those in Figure 2.10 produces poorly resolved semblance maxima at shear times t_{SS0} smaller than about 5-6 s (not shown). This, however, is a consequence of low V_S/V_P ratios in the shallow layers rather than a deficiency of the applied procedure. The semblance maxima of ΨS-waves become better focused as t_{SS0} exceeds 6-7 s, which corresponds to P-wave times t_{PP0} between 2 and 3 s. The results of velocity analysis on PP- and ΨS-wave CMP gathers (Figure 2.11) are used below to estimate interval velocities.

2.4.1 Evidence for effective anisotropy

Prior to estimating the interval-velocity model, one needs to select its type. Ideally, such a choice should be made based on understanding of which subsurface features are constrained by the available data. Here, I show that the event correlation (Figure 2.9) and the picked normal-moveout (NMO) velocities (Figure 2.11) unambiguously indicate non-negligible anisotropy for the Gulf of Mexico data. To draw such a conclusion, we can use the fact that the subsurface structure, being characterized by weak lateral heterogeneity and mild dips (see Figure 2.14 below), is approximately one-dimensional.

Following Grechka et al. (2002b), let us examine two velocity ratios: g_0, which is equal

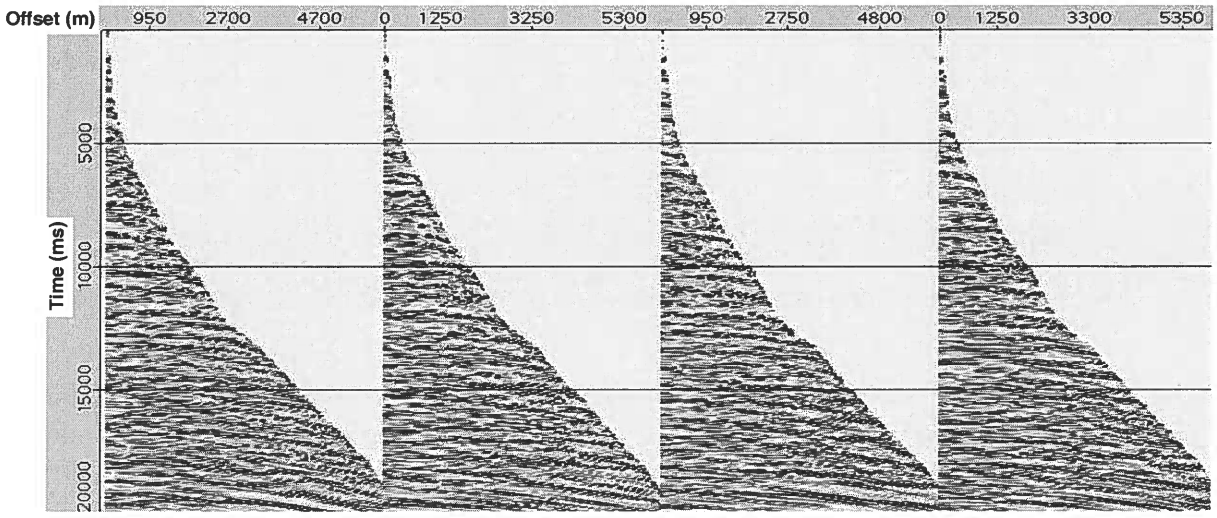

Figure 2.10. Representative CMP gathers of ΨS-waves.

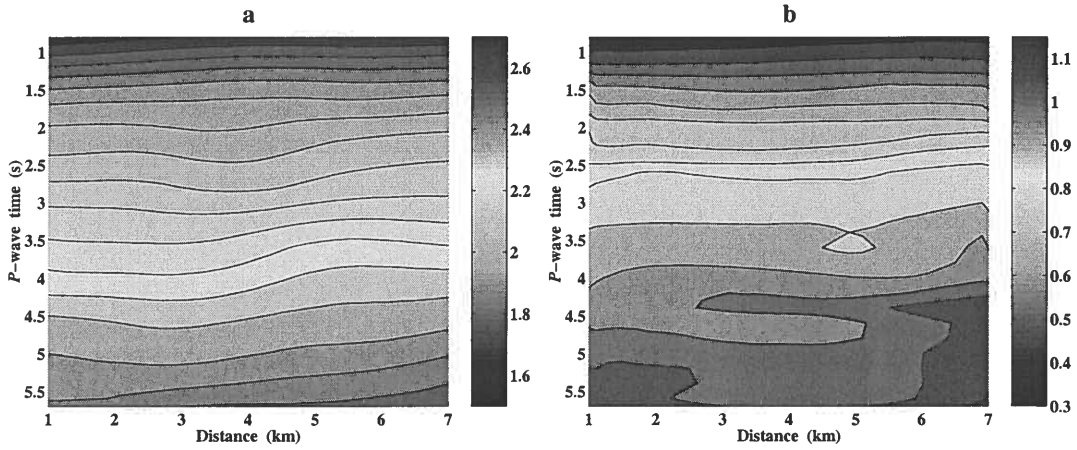

Figure 2.11. Picked (a) PP-wave and (b) ΨS-wave NMO velocities (in km/s).

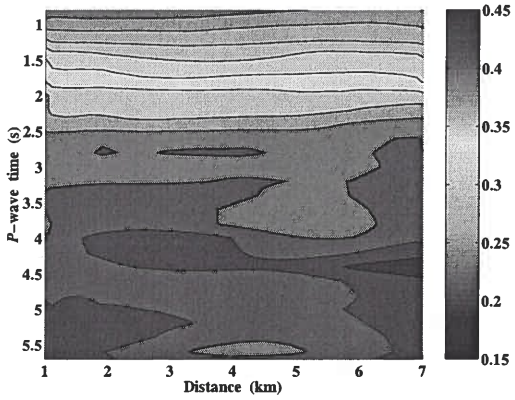

Figure 2.12. Ratio g_{nmo} of the picked ΨS- and P-wave NMO velocities. For comparison, the color scale in this figure is the same as that in Figure 2.9b.

to the ratio of the vertical velocities V_{S0} and V_{P0} for horizontally layered media,

$$g_0 \equiv \frac{t_{PP0}}{t_{SS0}} = \frac{V_{S0}}{V_{P0}}, \tag{2.13}$$

and

$$g_{\text{nmo}} \equiv \frac{V_{S,\text{nmo}}}{V_{P,\text{nmo}}}. \tag{2.14}$$

The ratio g_0, derived from the PP and PS event correlation, is shown in Figure 2.9b, while the ratio of ΨS- and P-wave NMO velocities is given in Figure 2.12. Comparison shows that g_{nmo} is consistently greater than g_0. For the P-wave times $t_{PP0} > 2.5$ s, where the ΨS-wave NMO velocities are sufficiently accurate, $g_0 \approx 0.3$, whereas $g_{\text{nmo}} \approx 0.4$.

In isotropic layered media, g_{nmo} can be greater than g_0 only because of larger vertical variability of S-wave velocities compared to that of the P-wave ones. According to Grechka et al. (2002b), relative vertical changes of V_{S0} would have to be orders of magnitude greater than those of V_{P0} to explain the observed values of g_0 and g_{nmo} for isotropic media. Since such a high vertical variation of shear-wave velocities is not supported by the data, only the presence of anisotropy can give a plausible explanation for the difference between the two velocity ratios. Therefore, the estimated subsurface model has to be anisotropic.

Next, we need to choose the type (symmetry) of anisotropy. This choice is essentially constrained by our ability to estimate relevant anisotropic parameters from the 2D narrow-azimuth data acquired over a relatively simple (close to 1-D) subsurface structure. Taking into account that the study area is located in a sedimentary basin, transversely isotropic model with a vertical symmetry axis (VTI) is a reasonable choice. Also, the constructed ΨS data should represent SV-waves, as appear to SH-waves, because the input converted waves were recorded on the inline horizontal component.

The ratios g_0 and g_{nmo} defined by equations (2.13) and (2.14) can be directly linked

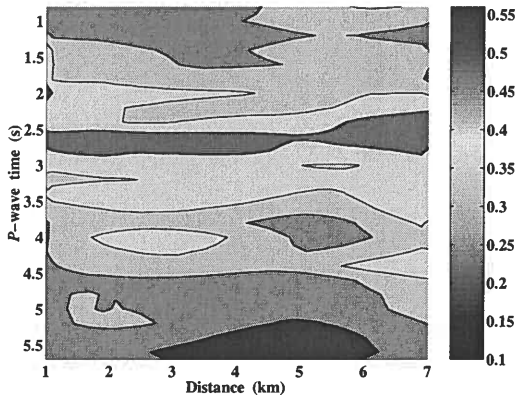

Figure 2.13. Effective χ defined by equation (2.15).

to the anisotropic coefficients δ (Thomsen, 1986) and σ (Tsvankin & Thomsen, 1994) in a single plane VTI layer. Since $V_{P,\mathrm{nmo}} = V_{P0}\sqrt{1+2\,\delta}$ and $V_{S,\mathrm{nmo}} = V_{S0}\sqrt{1+2\,\sigma}$, the combination

$$\frac{1}{2}\left(\frac{g_{\mathrm{nmo}}^2}{g_0^2} - 1\right) = \frac{\sigma - \delta}{1+2\,\delta} \equiv \chi \tag{2.15}$$

depends solely on δ and σ and, therefore, quantifies the effective anisotropy that can be unambiguously estimated from the vertical traveltimes and NMO velocities of P- and SV-waves in a plane homogeneous VTI layer. Because $g_0 > g_{\mathrm{nmo}}$, the parameter $\chi > 0$ (Figure 2.13), which supports the conclusion that the subsurface is effectively anisotropic.

2.4.2 Estimation of interval parameters

The feasibility of estimating anisotropy from reflection seismic data is governed by the extent of angular coverage that can be used in the inversion. Both acquisition design and the presence or absence of dipping structures influence the range of angles of the reflected waves. While 3D, wide-azimuth, long-spread data generally constrain anisotropic parameters better than do 2D, narrow-azimuth, conventional-offset data, all pertinent quantities still cannot be estimated uniquely from PP- and PS-waves in horizontally layered VTI media unless check shots or well logs are available (Grechka & Tsvankin, 2002a; Grechka et al., 2002b). Therefore, it is important to examine whether or not the data contain enough dip information for the inversion.

Figure 2.14 addresses this issue. It shows a histogram of more than one thousand dips ψ automatically picked from the stacked PP data. Even though the dips in Figure 2.14 were estimated using the equation

$$\psi = \tan^{-1}\left[\left|\frac{dt_{PP0}}{dY}\right| \frac{V_{P,\mathrm{nmo}}}{2}\right],$$

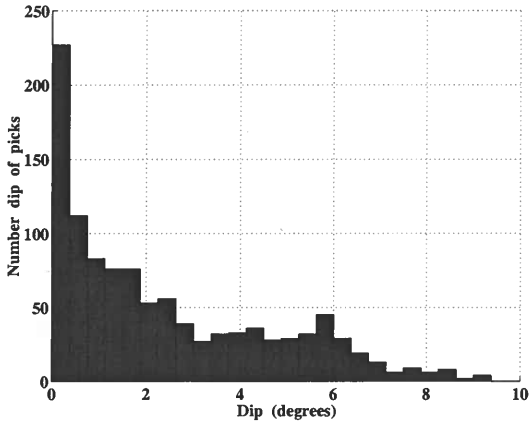

Figure 2.14. Distribution of dips picked from the P-wave zero-offset time section.

which ignores anisotropy and heterogeneity, the message in Figure 2.14 is clear. The subsurface can be treated as horizontally layered for the purpose of anisotropic inversion because the mean absolute dip is about 2.5° and 50% of the picks fall below 1.7°.

As shown by Grechka & Tsvankin (2002a), the true depths in horizontally layered VTI media cannot be estimated from reflected PP- and PS-waves even when long-spread data are available. Therefore, one option is to set either anisotropic coefficient δ or σ to any chosen constant value or any predetermined function and proceed with anisotropic stacking velocity tomography as was done by Grechka et al. (2002a). The arbitrary choice of δ or σ will produce a family of kinematically equivalent VTI depth models. Alternatively, one can perform parameter estimation in the time domain to evaluate the interval NMO velocities $V_{P,\mathrm{nmo}}$ and $V_{S,\mathrm{nmo}}$ and the quantity χ treated as functions of the P-wave vertical time t_{PP0}. This yields a unique VTI time model, with the above mentioned ambiguity hidden in the time-to-depth conversion. I select the second option here.

Figures 2.15a and 2.15b show the interval $V_{P,\mathrm{nmo}}$ and $V_{S,\mathrm{nmo}}$ that were obtained by performing conventional Dix (1955) differentiation of the NMO velocities displayed in Figure 2.11. The interval anisotropy χ in Figure 2.15c was computed from the interval ratios g_{nmo} and the event correspondence (Figure 2.9). Even though the higher χ values for $t_{PP0} < 2.5$ s may be related to inaccuracies in shear-wave velocity picking, the magnitude of anisotropy is substantial.

Note that the inversion produces similar dipping features in the middle of the $V_{P,\mathrm{nmo}}$, $V_{S,\mathrm{nmo}}$, and χ sections. Such general similarity is expected because the three fields correspond to the same area of the subsurface. The sections of $V_{P,\mathrm{nmo}}$, $V_{S,\mathrm{nmo}}$, and χ, however, differ in many details. This also could have been predicted because they represent different physical properties obtained from different components of seismic data, which went through different processing sequences. Still, the three sections in Figure 2.15 complement each other, thus providing information that cannot be extracted from P-wave data alone.

Even though Figure 2.15 displays the final output, it hides a significant depth ambi-

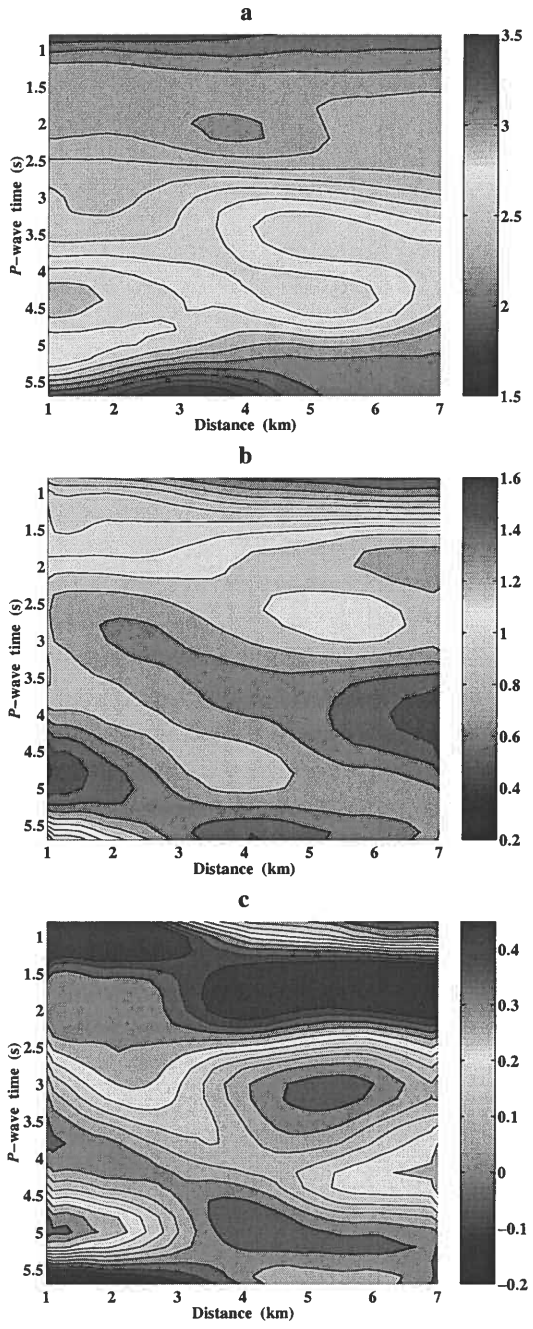

Figure 2.15. Interval (a) PP-wave and (b) ΨS-wave NMO velocities (in km/s), and (c) χ.

guity of the estimated anisotropic model. Neither anisotropic coefficient (δ or σ) needed to perform time-to-depth conversion can be estimated from the data. Instead, one can constrain only their combination $\chi = (\sigma - \delta)/(1 + 2\,\delta)$, which does not allow us to resolve δ and σ individually. One might notice an analogy between this conclusion and the results of nonhyperbolic velocity analysis of P-waves, where the estimated $V_{P,\mathrm{nmo}}$ and the Alkhalifah-Tsvankin (1995) anellipticity coefficient η also do not constrain the depth.

2.5 Summary

In this chapter, I described a processing flow designed for velocity analysis of converted waves. Under the assumptions that (i) both PP and PS reflection data are available and (ii) the PP and PS event correspondence is established, I developed an automatic procedure for generating the ΨS data that are supposed to have the kinematics of pure shear-wave primaries. As a result, conventional velocity analysis performed on ΨS CMP gathers yields S-wave NMO velocities. These velocities, along with those of the P-waves and the corresponding reflection time slopes, can be used for building elastic (usually anisotropic) interval-velocity models.

The methodology was tested on both synthetic and field data. The synthetic examples helped us to establish some data requirements and characteristics (e.g., PP and PS wavelets do not have to be the same, and random noise is not a problem). The presented case study confirmed that this processing flow can yield useful information about the subsurface that cannot be obtained from P-wave data alone.

A modified version of this chapter is already published in Geophysics (Grechka & Dewangan, 2003).

Chapter 3

Parameter estimation using PS-wave moveout asymmetry: Horizontal TTI layer

As discussed above, if the medium is anisotropic without a horizontal symmetry plane, the moveout of PS-waves becomes asymmetric. Applying the PP+PS=SS method to such PS-waves will not preserve the information about the asymmetry of PS moveout. Here, I modify the PP+PS=SS method introduced in Chapter 2 to obtain the asymmetry attributes in addition to the ΨS-wave gathers. Then I present an analytic study of the PSV-wave moveout asymmetry in a horizontal transversely isotropic layer with a tilted symmetry axis (TTI medium) and develop an inversion algorithm that operates with both pure and converted reflection modes. The TTI medium is parameterized here by the velocities of P- and S-waves in the symmetry direction (V_{P0} and V_{S0}, respectively), the tilt of the symmetry axis from the vertical (ν) and Thomsen's (1986) anisotropic coefficients ϵ, δ, and γ defined in the coordinate system associated with the symmetry axis (Tsvankin, 2001).

In principle, the symmetry-axis orientation and the parameters V_{P0}, ϵ, and δ of a horizontal TTI layer can be estimated from P-wave data alone, but this inversion requires the normal-moveout (NMO) ellipses (i.e., wide-azimuth P-wave reflections) from a horizontal and a dipping interface, and both the tilt ν and reflector dip should be no less than 30–40° (Grechka & Tsvankin, 2000). Although the addition of the NMO ellipses of pure SV-waves to those of P-waves makes it possible to invert for the TTI parameters using the reflections from a single interface, the parameter estimation is still ambiguous for a range of small tilts and reflector dips (Grechka & Tsvankin, 2000; Grechka et al., 2002a). Therefore, even wide-azimuth traveltimes of pure reflection modes (P and SV) from subhorizontal interfaces are insufficient for reconstructing the TTI model.

3.1 Modification of the PP+PS=SS method

As discussed in Chapter 2, the construction of SS-waves with the correct kinematics (but not amplitudes) does not require explicit information about the velocity field, but it is necessary to correlate PP and PS arrivals and identify the events reflected from the same interface. Application of equation (2.4) produces reflection SS data with the traveltimes of SS primaries but generally distorted amplitudes. The moveout of the constructed SS-waves in common-midpoint (CMP) geometry is always symmetric, as is the case for any pure reflection mode. Conventional-spread SS traveltimes are described by the NMO velocity (in 2D) and NMO ellipse (in 3D), which can be obtained using algorithms developed for PP-

wave data. The NMO velocities or ellipses of the PP- and SS-waves can then be combined in velocity analysis using, for example, stacking-velocity tomography, which proved to be particularly efficient for anisotropic media (Grechka et al., 2002a).

Still, for many anisotropic models including a horizontal TTI layer, pure reflection modes are insufficient for estimating the vertical velocities and anisotropic coefficients (Grechka & Tsvankin, 2000; Grechka et al., 2002a). In such a case, an important question is whether or not including asymmetry attributes of the recorded PS-waves in the inversion algorithm can help in recovering the medium parameters. From equation (2.4), information about the moveout asymmetry of PS arrivals is not preserved in the computed SS traveltime, which depends on only the *sum* of the traveltimes of the PS-waves converted at point R (Figure 2.1). Below, I add certain measures of the PS-wave moveout asymmetry to the traveltimes of the PP-waves and the constructed SS-waves in the inversion for the parameters of TTI media.

A generalized version of the PP+PS=SS method based on equation (2.4) was introduced in Chapter 2. Instead of operating with prestack PP and PS traveltimes, I applied a particular convolution of PP and PS traces to produce seismograms of the corresponding ΨS-waves [equation (2.5)]. The main contribution to the integral comes from the stationary point that yields the traveltime of the constructed ΨS-wave given by equation (2.4):

$$\begin{aligned} \tau_{SS}(x^{(3)},x^{(4)}) &= \min_{x^{(1)},\,x^{(2)}} \tau(x^{(1)},x^{(2)},x^{(3)},x^{(4)}) \\ \tau(x^{(1)},x^{(2)},x^{(3)},x^{(4)}) &\equiv t_{PS}(x^{(1)},x^{(3)}) + t_{PS}(x^{(2)},x^{(4)}) - t_{PP}(x^{(1)},x^{(2)}), \end{aligned} \tag{3.1}$$

where τ is the traveltime function defined in Appendix A. The stationary points are obtained by equating the first derivative of τ with respect to $x^{(1)}$ and $x^{(2)}$ to zero. Therefore, the points $x^{(1)}$ and $x^{(2)}$ must correspond to any extremum of the time function. To prove, that it will be a minimum, let us consider the second derivative of τ,

$$\frac{\partial^2 \tau}{\partial \left(x^{(j)}\right)^2} = \frac{\partial^2 \left(t_{PS}(x^{(j)},x^{(j+2)}) - t_{PP}(x^{(1)},x^{(2)})\right)}{\partial \left(x^{(j)}\right)^2}, j = 1,2. \tag{3.2}$$

Since the curvature of the PS-wave traveltime will be larger than that of the P-wave traveltime, the second derivative of the time function will be positive. Hence, the stationary points will always correspond to a minimum of the time function. Note that in Figure 2.3, the stationary points are indicated by the maximum value of the time function because it is a 1D plot expressed as a function of the P-wave half-offset rather than $x^{(1)}$ or $x^{(2)}$. The above property is valid only for VTI media while equation (3.1) remains valid for arbitrarily anisotropic media.

To preserve information about the moveout asymmetry of the recorded PS-wave, I suggest to generate an *asymmetry gather* in addition to the ΨS data. When using the PP+PS=SS method, it is natural to define the asymmetry through the difference between

the two PS traveltimes corresponding to the same reflection point (Figure 2.1):

$$\Delta t_{PS}(x^{(3)}, x^{(4)}) = t_{PS}(x^{(1)}, x^{(3)}) - t_{PS}(x^{(2)}, x^{(4)}) . \tag{3.3}$$

I modified the algorithm of Chapter 2 to estimate the stationary points given by equation (3.1). Then the difference between the PS traveltimes (picked on the original data) corresponding to each stationary point could be used to compute the time asymmetry factor from equation (3.3).

If the reflector is horizontal and the overburden is laterally homogeneous as is the case for horizontal TTI layer, the two reciprocal PS-waves in Figure 2.1 have the same magnitude but opposite signs of the ray parameter (horizontal slowness), which corresponds to that for the PP reflection from $x^{(1)}$ to $x^{(2)}$. Hence, equation (3.3) defines the asymmetry of the PS moveout in the slowness domain. Analytic expressions that describe the asymmetry factor Δt_{PS} are given in the next section.

Similar to the original PP+PS=SS method, which can be extended to 3D multiazimuth reflection data, the modified PP+PS=SS method can also be extended to 3D. The stationary points given by equation (3.1) then would correspond to a minimum in the 4D space.

3.2 Asymmetric moveout of PS-waves in TTI media

If the medium is anisotropic without a horizontal symmetry plane or laterally heterogeneous, the moveout of PS-waves becomes asymmetric.

3.2.1 Parametric moveout equations

Consider a PS-wave formed by mode conversion at an interface underlying an arbitrarily anisotropic, homogeneous layer. In general, an incident P-wave in such a model excites two reflected shear modes (PS_1 and PS_2). The traveltime of either PS-wave can be represented in parametric form as (Tsvankin & Grechka, 2002)

$$t_{PS} \equiv t_P + t_S = z\,.\,(q_P - p_{1P}\,q_{,1P} - p_{2P}\,q_{,2P} + q_S - p_{1S}\,q_{,1S} - p_{2S}\,q_{,2S}), \tag{3.4}$$

where t_P and t_S are the traveltimes along the P- and S-legs, respectively, z is the depth of the reflection (conversion) point, p_1 and p_2 are the horizontal components of the slowness vector (the subscripts "P" and "S" indicate the wave type), $q \equiv p_3$ is the vertical slowness, and $q_{,i} \equiv \partial q/\partial p_i$ $(i = 1, 2)$ (Figure C.1). Following Tsvankin & Grechka (2002), the slownesses are computed under the convention that the x_3-axis points up, and both legs of the PS ray represent upgoing waves (i.e., the corresponding group-velocity vectors point toward the earth's surface).

Here, I study a horizontal layer, in which the projections of the slowness vectors of the P- and S-legs onto the horizontal plane have to be identical to comply with Snell's law:

$$p_{1P} \equiv p_1 = -p_{1S}\,; \quad p_{2P} \equiv p_2 = -p_{2S}\,. \tag{3.5}$$

Equation (3.4) then simplifies to

$$t_{PS} = z.[q_P + q_S - p_1 (q_{,1P} - q_{,1S}) - p_2 (q_{,2P} - q_{,2S})]. \tag{3.6}$$

The corresponding source-receiver vector $\boldsymbol{x}$ of PS-waves in an anisotropic, homogeneous layer can be also expressed through the slowness components (Tsvankin & Grechka, 2002):

$$\begin{aligned} \boldsymbol{x}_{PS} = \{x_1, x_2\} &= z.\{(q_{,1P} - q_{,1S}), (q_{,2P} - q_{,2S})\}; \\ x_1 &= z.(q_{,1P} - q_{,1S}), \\ x_2 &= z.(q_{,2P} - q_{,2S}). \end{aligned} \tag{3.7}$$

Equation (3.7) yields the source-receiver offset x and the azimuth α of the source-receiver line with respect to the x_1-axis:

$$x_{PS} = |\boldsymbol{x}_{PS}| = \sqrt{x_1^2 + x_2^2}, \tag{3.8}$$

$$\alpha = \tan^{-1}\left(\frac{x_2}{x_1}\right). \tag{3.9}$$

3.2.2 Moveout asymmetry in the slowness domain

For laterally homogeneous models, such as a horizontal TTI layer, the moveout of converted waves becomes asymmetric only if the medium does not have a horizontal symmetry plane (e.g., Tsvankin, 2001). Conventionally, the moveout asymmetry is estimated in the offset domain by interchanging the source and receiver positions. Here, however, I define the traveltime asymmetry factor in the slowness domain:

$$\Delta t_{PS} = t_{PS}(p_1, p_2) - t_{PS}(-p_1, -p_2) = \Delta t_P + \Delta t_S, \tag{3.10}$$

where Δt_P and Δt_S represent the contributions to Δt_{PS} from the P- and S-legs of the PS ray, respectively. Equation (3.10) describes the difference between the traveltimes of the PS arrivals excited by incident P-waves that have the same magnitude but opposite signs for the horizontal projection of the slowness vector.

If the moveout of PS-waves is symmetric, then changing the sign of the horizontal slowness reverses the direction of the source-receiver vector $\boldsymbol{x}$ [equation (3.7)] with no change in the absolute value of offset. Hence, the measure of asymmetry for $\boldsymbol{x}$ can be defined in the following way:

$$\boldsymbol{\Delta x}_{PS} = \boldsymbol{x}_{PS}(p_1, p_2) + \boldsymbol{x}_{PS}(-p_1, -p_2). \tag{3.11}$$

The main advantage of treating the asymmetry in the slowness domain is that, for a laterally homogeneous medium, both Δt_{PS} and $\boldsymbol{\Delta x}_{PS}$ can be obtained directly from the PP+PS=SS method [see equation (3.3) and Figure 2.1].

Equations (3.6), (3.10), (3.7), and (3.11) give an exact representation of the moveout asymmetry of PS-waves for any horizontal anisotropic layer. Next, I apply this formulation

to study the dependence of Δt_{PS} on the parameters of TI media with an arbitrary tilt of the symmetry axis. The factor $\boldsymbol{\Delta x}_{PS}$ is discussed later on, after the introduction of the offset, $x_{\min}$, of the PS-wave moveout minimum in CMP geometry.

Since the contributions of the symmetry-axis orientation and anisotropic parameters to the time asymmetry factor Δt_{PS} are hidden in the components of the slowness vector, in Appendix C I estimate those contributions by linearizing equation (3.10) with respect to ϵ and δ under the assumption of weak anisotropy ($|\epsilon| \ll 1$ and $|\delta| \ll 1$). The derivation is carried out for the PS mode that is polarized in the plane formed by the slowness vector and the symmetry axis. Note that although I will denote this wave "PSV," its polarization vector lies in the vertical incidence plane only if that plane contains the symmetry axis.

The coordinate system is chosen in such a way that the symmetry axis is confined to the $[x_1, x_3]$-plane, which represents the only vertical symmetry plane of the model and will be called here the *symmetry-axis plane* (Figure C.1). The sign of the time difference in equation (3.10) is specified by assuming that the symmetry axis is dipping in the positive x_1-direction.

Substituting equations (C.5) and (C.6) into equation (3.10), I obtain a linearized expression for the moveout asymmetry factor of the PSV-wave:

$$\Delta t_{PS} = -8\,\eta\, z\, V_{P0}^2\; p_1\, [p_2^2 + (2p_1^2 + p_2^2)\cos 2\nu]\, \sin 2\nu\,, \tag{3.12}$$

where $\eta \equiv (\epsilon - \delta)/(1 + 2\delta) \approx \epsilon - \delta$ is the "anellipticity" coefficient responsible for time processing of P-wave data in VTI media (Alkhalifah & Tsvankin, 1995). In the symmetry-axis plane $[x_1, x_3]$, the slowness component p_2 vanishes, and equation (3.12) simplifies to

$$\Delta t_{PS}(p_2 = x_2 = 0) = -8\,\eta\, z\, V_{P0}^2\; p_1^3\, \sin 4\nu\,. \tag{3.13}$$

Based on equations (3.12) and (3.13), the main properties of the PSV-wave time asymmetry in the slowness domain can be summarized as follows:

- The asymmetry factor Δt_{PS} vanishes for VTI ($\nu = 0°$) and HTI ($\nu = 90°$) media because these two models have a horizontal symmetry plane. In the symmetry-axis plane, the linearized expression for Δt_{PS} [equation (3.13)] also goes to zero for $\nu = 45°$. The higher-order terms in ϵ and δ, however, do not vanish, which makes the moveout weakly asymmetric.

- The contributions to the asymmetry factor from the P-leg [equation (C.5)] and S-leg [equation (C.6)] of the converted wave are identical. Although this result was proved here in the weak-anisotropy approximation, numerical tests show that it remains valid for arbitrary strength of the anisotropy.

- The asymmetry in the slowness domain depends only on the *difference* $\eta = \epsilon - \delta$, and therefore vanishes if the anisotropy is elliptical ($\epsilon = \delta$). Since for elliptical media there is no SV-wave velocity anisotropy, the S-leg of the converted wave does not produce any moveout asymmetry. This means that the P-leg cannot cause the asymmetry either (see the previous item).

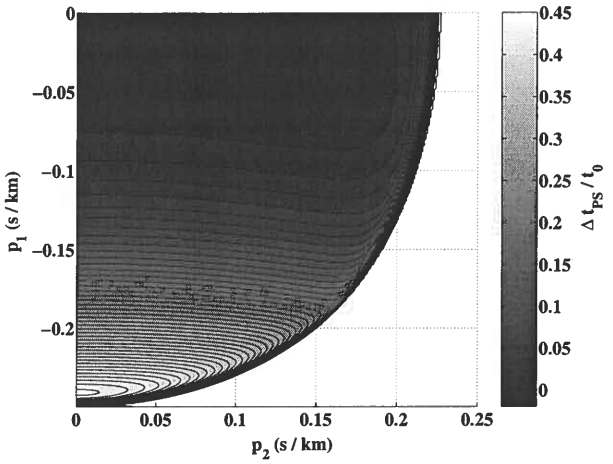

Figure 3.1. Exact asymmetry factor Δt_{PS} in the slowness domain for the PSV-wave in a horizontal TTI layer. Δt_{PS} is normalized by the zero-offset traveltime t_0 of the PSV-wave. The asymmetry for negative slowness p_2 is not shown because $\Delta t_{PS}(p_1, -p_2) = \Delta t_{PS}(p_1, p_2)$. The medium parameters are $V_{P0} = 4$ km/s, $V_{S0} = 2$ km/s, $\epsilon = 0.1$, $\delta = -0.1$, $\nu = 70°$, and $z = 1$ km.

- The magnitude of the asymmetry factor in the symmetry-axis plane [equation (3.13)] reaches its maximum for the tilts $\nu = 22.5°$ and $\nu = 67.5°$. Therefore, Δt_{PS} is quite sensitive to the deviation of the symmetry axis from the vertical and horizontal directions.

The azimuthally-varying asymmetry factor Δt_{PS} computed for a typical TTI model from exact equations (3.6) and (3.10) is displayed in Figure 3.1. There is a substantial variation of Δt_{PS} with the slowness component p_1 (e.g., in the x_1-direction where $p_2 = 0$), while the influence of p_2 is much weaker. Therefore, Figure 3.1 indicates that most of the 3D (wide-azimuth) moveout asymmetry information can be obtained in the symmetry-axis plane $[x_1, x_3]$.

Note that the line $p_1 = 0$ in Figure 3.1 where $\Delta t_{PS} = 0$ *does not* correspond to acquisition in the $[x_2, x_3]$-plane. Since $[x_2, x_3]$ is not a symmetry plane, downgoing P rays with $p_1 = 0$ deviate from the vertical incidence plane $[x_2, x_3]$, and the source-receiver direction of the reflected PS-wave is not parallel to the x_2-axis.

Figure 3.2 shows, in more details, the function $\Delta t_{PS}(p_1)$ in the symmetry-axis plane. Both the PP+PS=SS method and parametric equation (3.10) should to produce exact values of Δt_{PS}, which is confirmed by my numerical results. The magnitude of the asymmetry factor is quite substantial – it exceeds 40% of the zero-offset time before rapidly decreasing for large values of p_1.

The accuracy of the weak-anisotropy approximation (3.13) in Figure 3.2 is quite satisfactory considering that it incorporates the contribution of the S-leg of the converted wave. Typically, the weak-anisotropy approximation is much less accurate for SV-waves

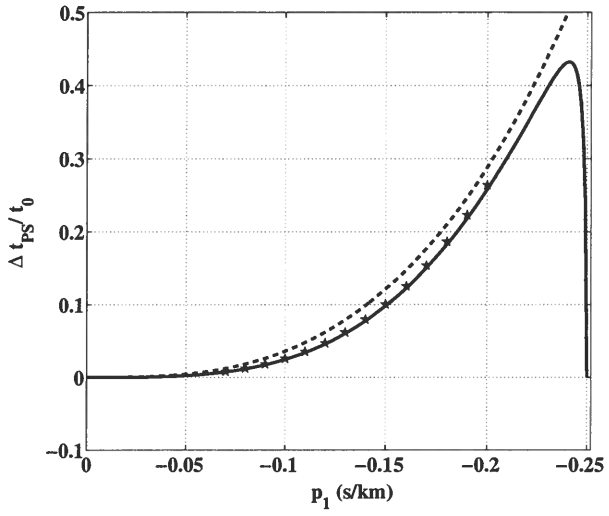

Figure 3.2. Asymmetry factor from Figure 3.1 in the $[x_1, x_3]$-plane ($p_2 = 0$). The solid line is obtained from the exact parametric equation (3.10); the dashed line is the weak-anisotropy approximation (3.13); the stars mark the output of the PP+PS=SS method. The maximum offset-to-depth ratio of the PP and PS data is close to two.

than it is for P-waves because of the large magnitude of the anisotropic parameter $\sigma \equiv (V_{P0}^2/V_{S0}^2)(\epsilon - \delta)$ (Tsvankin & Thomsen, 1994; Tsvankin, 2001). For the type of computation here, however, the anisotropy-related asymmetry factors for the P- and S-legs are equal to each other (see the second item), and the error of the weak-anisotropy approximation is the same for both P- and S-waves.

3.2.3 Moveout asymmetry in the offset domain

Most existing results on the moveout asymmetry of PS-waves are obtained in the offset domain (Thomsen, 1999; Tsvankin & Grechka, 2000, 2002). If the source and receiver positions are interchanged, the traveltime of the converted wave does not remain the same unless the reflector is horizontal and the medium above it is laterally homogeneous and has a horizontal symmetry plane. For PS data collected in a CMP gather centered at the origin of the coordinate system, the asymmetry factor in the offset domain is defined as

$$\Delta t_{PS} \equiv t_{PS}(\boldsymbol{x}_{PS}) - t_{PS}(-\boldsymbol{x}_{PS}), \tag{3.14}$$

where $\boldsymbol{x}_{PS}$ is the offset vector of the PS-wave given by equation (3.7).

Azimuthally varying minimum-time offset $x_{\min}$.– If reflection moveout is asymmetric, the minimum of the traveltime curve in a common-midpoint gather is shifted from the CMP location. The offset corresponding to the traveltime minimum (I denote it by $x_{\min}$) is a convenient measure of the asymmetry that depends on the reflector orientation

and anisotropic parameters. Analytic expressions for $x_{\min}$ in a VTI layer above a dipping reflector are given by Tsvankin & Grechka (2000, 2002) and Tsvankin (2001). In a horizontal TTI layer, $x_{\min}$ carries useful information about the tilt of the symmetry axis and the anisotropic parameters.

In Appendix D, I use equations (3.7)–(3.9) for the offset $\boldsymbol{x}$ in terms of the ray parameter to obtain the following simple expression for the azimuthal variation of $x_{\min}$:

$$x_{\min}(\alpha) \;=\; x_0 \cos\alpha\,, \tag{3.15}$$

where $x_0 = x_{\min}(\alpha = 0^\circ)$ is the offset of the traveltime minimum in the symmetry-axis plane $[x_1, x_3]$, given in equation (D.5):

$$x_0 = x_{\min}(\alpha = 0^\circ) = -z\left[\epsilon \sin 2\nu - \frac{\eta}{2}\left(1 + \frac{V_{P0}^2}{V_{S0}^2}\right)\sin 4\nu\right]. \tag{3.16}$$

According to equation (3.15), $x_{\min}(\alpha)$ reaches its maximum in the symmetry-axis plane and vanishes in the orthogonal direction. If $x_{\min}$ is plotted as the radius vector for each azimuth α, it traces out a circle with radius $x_0/2$ and center $(x_0/2, 0)$ on the x_1-axis. While equation (3.16) for x_0 is valid only in the weak-anisotropy limit, the azimuthal dependence of $x_{\min}$ is described by equation (3.15) for any strength of the anisotropy (Figure 3.3; similar results were obtained for much larger magnitudes of ϵ and δ). Hence, the azimuthal variation of $x_{\min}$ can help to estimate the symmetry-axis azimuth from converted-wave data, but it does not provide additional information about the anisotropic coefficients.

The offset $x_{\min}$ is not only responsible for the shape of the PS-wave moveout in CMP geometry, it also largely controls the asymmetry measure $\boldsymbol{\Delta x}_{PS}$ [equation (3.11)] defined in the slowness domain. In the symmetry-axis plane, $\boldsymbol{\Delta x}_{PS}$ can be written as

$$\boldsymbol{\Delta x}_{PS} = \boldsymbol{x}_{PS}(p_1, 0) + \boldsymbol{x}_{PS}(-p_1, 0). \tag{3.17}$$

Linearizing equation (3.17) in the anisotropic coefficients using equation (3.7) yields the projection of the vector $\boldsymbol{\Delta x}_{PS}$ onto the x_1-axis in the form

$$(\Delta x_{PS})_{x_1} \;=\; 2\,x_0 \;+\; 12\,\eta\,z\,V_{P0}^2\,p_1^2\,\sin 4\nu\,, \tag{3.18}$$

where x_0 is given by equation (3.16). According to equation (3.18), the quantity $|\boldsymbol{\Delta x}_{PS}|$ can be approximated by a hyperbolic function of the slowness p_1 with the value at the apex determined by $2\,x_0$. Indeed, when $p_1 = 0$, the PS-rays corresponding to both p_1 and $-p_1$ coincide and have the same offset x_0 (Figure 3.4). If the PS moveout were symmetric, the offsets for p_1 and $-p_1$ (circles and diamonds, respectively, in Figure 3.4) would have identical absolute values but *opposite* signs, and the zero-offset PS-ray would have the slowness $p_1 = 0$. Figure 3.4 also confirms that the linearized equation (3.18) is sufficiently accurate for weak and moderate anisotropy.

Therefore, an alternative way of estimating x_0 is to fit a hyperbolic function to the slowness-dependent factor $(\Delta x_{PS})_{x_1}$ and find its intercept for $p_1 = 0$. It is interesting that the coefficient of the quadratic term of the hyperbola (3.18) is formed by the same

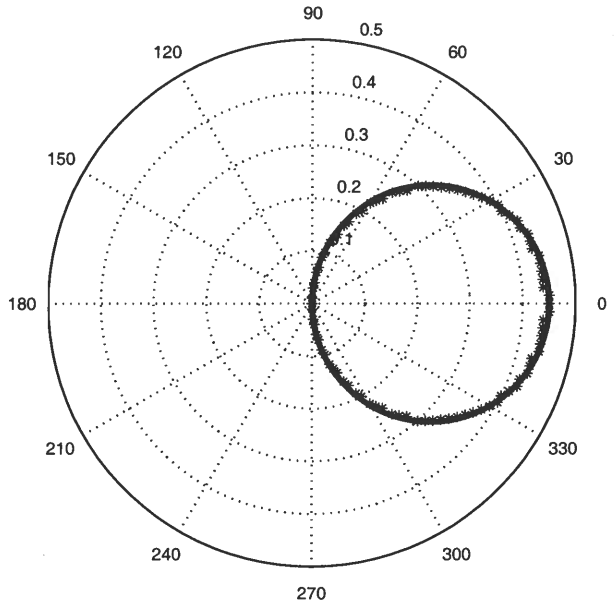

Figure 3.3. Polar plot of the offset $x_{\min}(\alpha)$ for the model from Figure 3.1. The stars mark values obtained from anisotropic ray tracing of PS-waves and the solid line is computed from equation (3.15) with the exact value of x_0.

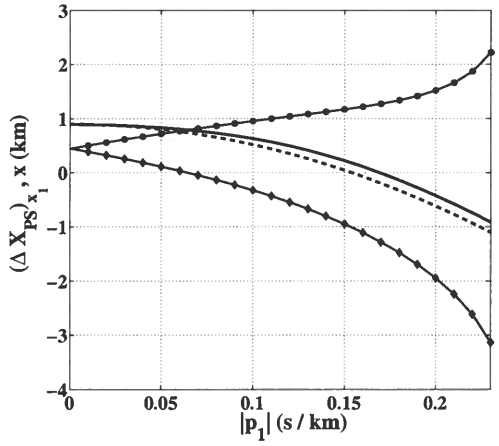

Figure 3.4. Slowness-domain factor $(\Delta x_{PS})_{x_1}$ and PS-wave offsets in the symmetry-axis plane of a TTI layer with the same parameters as those in Figure 3.1. The solid line marks exact values of $(\Delta x_{PS})_{x_1}$ from equation (3.17), and the dashed line is the weak-anisotropy approximation (3.18). Exact PS-wave offsets for positive slownesses p_1 are marked by circles, offsets for negative slownesses by diamonds; the offset is considered positive if the vector $\boldsymbol{x}_{PS}$ points in the x_1-direction.

combination of the medium parameters that governs the traveltime asymmetry factor (3.13).

Asymmetry factor in the offset domain To give an analytic description of the factor Δt_{PS} [equation (3.14)] in the offset domain, I expanded the traveltime in a double Taylor series around the offset $x_{\min}$ (see Appendix E). The result is convenient to represent in terms of the offset x and the azimuth α of the source-receiver line. The linearized expression (E.14) for Δt_{PS} contains linear and cubic terms in the offset x and is sufficiently accurate for relatively small offsets.

This approximation can be extended to larger offsets by adapting the approach of Tsvankin & Thomsen (1994), who developed a highly accurate nonhyperbolic moveout equation for P-waves by modifying the $t^2(x^2)$ Taylor series in such a way that it became convergent at $x \to \infty$. For long-offset converted PS-waves, the incident P-wave travels almost horizontally and accounts for most of the total reflection traveltime. The contribution of the S-leg then becomes negligible, and the asymmetry factor at infinite offset goes to zero. To ensure that Δt_{PS} vanishes for $x \to \infty$, I add a denominator $(1 + Cx^2)$ to the cubic term in equation (E.14):

$$\begin{aligned} \Delta t_{PS} &= A\,x + \frac{B\,x^3}{1 + C\,x^2}\,; \\ A &= -\frac{2\,x_0\,\cos\alpha}{z\,(V_{P0} + V_{S0})}\,, \\ B &= -\frac{4\,\eta\,V_{P0}^2\,\sin 2\nu\,\cos\alpha}{z^2\,(V_{P0} + V_{S0})^3}\left(2\cos 2\nu\,\cos^2\alpha + \sin^2\alpha\right), \\ C &= -\frac{B}{A}\,. \end{aligned} \tag{3.19}$$

In the symmetry-axis plane ($\alpha = 0°$) the coefficients A and B in equation (3.19) become

$$A = -\frac{2\,x_0}{z\,(V_{P0} + V_{S0})}\,, \tag{3.20}$$

$$B = -\frac{4\,\eta\,V_{P0}^2\,\sin 4\nu}{z^2\,(V_{P0} + V_{S0})^3}\,. \tag{3.21}$$

The initial slope A of the asymmetry factor for any azimuth α is governed by the term $(x_0\,\cos\alpha)$ that represents the offset $x_{\min}(\alpha)$ of the local traveltime minimum [equation (3.15)]. The higher-order coefficient B depends on the parameter $\eta \approx \epsilon - \delta$ and the tilt ν, and, in principle, can be combined with A for the purpose of parameter estimation. Analysis of equation (3.19), however, shows that the moveout asymmetry in the offset domain can be expressed through the time-asymmetry factor Δt_{PS} in the slowness domain and the offset $x_{\min}(\alpha)$.

The azimuthally varying asymmetry factor in the offset domain in Figure 3.5 exhibits a pattern generally similar to that of Δt_{PS} in the slowness domain. The most rapid change in Δt_{PS} is observed in the $[x_1, x_3]$-plane (see also Figure 3.6), while in the plane $[x_2, x_3]$

the PS-wave moveout is symmetric ($\Delta t_{PS} = 0$). The absence of the moveout asymmetry for acquisition in the x_2-direction is predicted by equation (3.19), which yields $\Delta t_{PS} = 0$ for $\alpha = 90°$. Note that, as discussed above, PS-waves recorded in the $[x_2, x_3]$-plane have out-of-plane slowness vectors with $p_1 \neq 0$. Therefore, the lines $x_1 = 0$ in Figure 3.5 and $p_1 = 0$ in Figure 3.1 correspond to PS arrivals with different azimuthal orientations of the source-receiver vector.

The error of the weak-anisotropy approximation (3.19) increases with offset before flattening out at intermediate x (Figure 3.6) and eventually going to zero for infinitely large offsets. Overall, equation (3.19) gives an adequate qualitative description of the moveout asymmetry, including a maximum of $\Delta t_{PS}(x)$ at offsets close to the reflector depth (Figure 3.6). By design, equation (3.19) also converges toward the correct value $\Delta t_{PS} = 0$ for $x \to \infty$. However, I choose to setup the parameter-estimation algorithm using the asymmetry attributes obtained from the modified PP+PS=SS method because of the following reasons:

- Since the PP+PS=SS method removes reflection-point dispersal, the time and offset asymmetry attributes obtained from this method are less influenced by lateral heterogeneity. In contrast, the asymmetry defined by equation (3.14) does not account for conversion-point dispersal and may be significantly distorted in the presence of lateral heterogeneity.

- The reconstructed SS-wave traveltimes can be approximated with a hyperbola, which yields the shear-wave NMO velocity. Since the PP+PS=SS method is required to generate SS data, the asymmetry attributes can also be estimated in a straightforward way using the modified PP+PS=SS method.

- The analytic expression for the time and offset asymmetry attributes defined in the slowness domain are concise and may help in evaluating the effectiveness of the parameter-estimation algorithm in the presence of noise.

- Some convenient properties of the asymmetry attributes are valid only if we define these attributes in the slowness domain.

3.3 Parameter estimation

The goal of the inversion algorithm introduced here is to estimate the parameters of a horizontal TTI layer from PP and PS (PSV) reflection events. As emphasized by Grechka & Tsvankin (2002b) and Grechka & Dewangan (2003), effective application of the PP+PS=SS method requires acquisition of long-offset (i.e., offsets should reach at least twice the reflector depth) PP and PS data. If the offset-to-depth ratio for the recorded arrivals is less than two, the range of offsets for the constructed SS data is insufficient for obtaining a reliable estimate of the S-wave stacking velocity.

The numerical tests below show that for a wide range of the tilt angles ν of the symmetry axis the inversion can be performed using 2D data in the symmetry-axis plane.

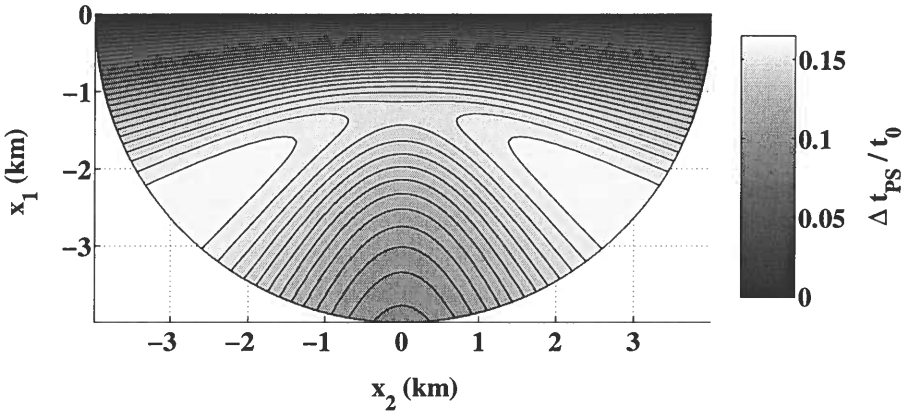

Figure 3.5. Exact normalized asymmetry factor Δt_{PS} in the offset domain [equation (3.14)]. The data were generated by anisotropic ray tracing for the model from Figure 3.1. After the initial increase with offset, the asymmetry decreases for large offsets and goes to zero for $x \to \infty$.

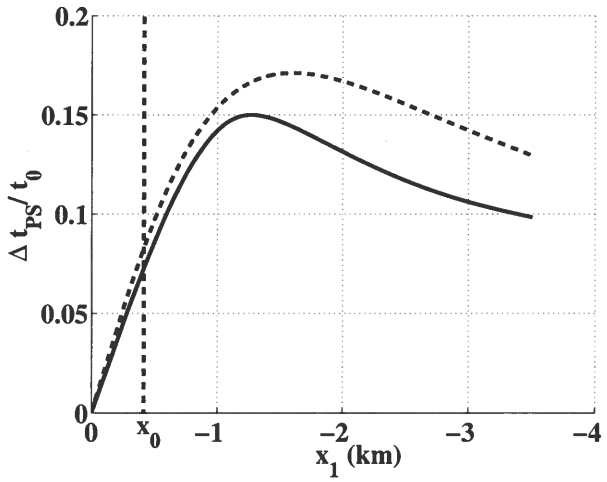

Figure 3.6. Asymmetry factor from Figure 3.5 in the symmetry-axis plane $x_2 = 0$. The solid line is the ray-tracing result; the dashed line is the weak-anisotropy approximation (3.19). Also marked is the offset $x_0 = x_{\min}(\alpha = 0°)$ of the traveltime minimum.

Full-azimuth acquisition, however, is necessary to find the orientation of this plane unless it is known, for example, from geological information. Another possible way to estimate the azimuth of the symmetry-axis plane is by analyzing the polarization direction of PS-waves at small source-receiver offsets.

3.3.1 Data processing

Conventional hyperbolic velocity analysis of the PP data yields their stacking velocity ($V_{\mathrm{nmo,P}}$) and zero-offset reflection traveltime (t_{P0}). Then, application of the PP+PS=SS method to the PP and PS records produces traces of "quasi-shear" waves that have the kinematics of the pure SS (SVSV) reflections (Grechka & Tsvankin, 2002b; Grechka & Dewangan, 2003). Therefore, processing of the constructed SS arrivals can be used to estimate the stacking velocity ($V_{\mathrm{nmo,S}}$) and zero-offset traveltime (t_{S0}) of the SS-waves that were not physically excited in the survey. If the data have a wide range of source-receiver azimuths, it may be possible to obtain the NMO ellipses of the PP- and SS-waves (Grechka & Tsvankin, 1998; Grechka et al., 2002a).

The above methodology, described in detail by Grechka et al. (2002a), is designed to avoid complications associated with the processing of mode-converted waves. For some anisotropic models, the combination of PP- and SS-waves is sufficient to estimate the medium parameters without additional information. For TTI media, however, the joint inversion of PP- and SS-waves is feasible only for substantial reflector dips or near-horizontal orientations of the symmetry axis (Grechka et al., 2002a).

Here, I supplement the moveouts of the PP-waves and constructed SS-waves in parameter estimation with the PS-wave asymmetry attributes obtained from the PP+PS=SS method. For laterally homogeneous media, the traveltime asymmetry $\Delta t_{PS}(x^{(3)}, x^{(4)})$ produced by the PP+PS=SS method [equation (3.3)] coincides the asymmetry factor defined in the slowness domain [equation (3.10)]. Another reason to work with the asymmetry attributes in the slowness domain is the relative simplicity of the corresponding analytic expressions.

The offset $x_{\min}(\alpha = 0)$ of the PS-wave traveltime minimum in the symmetry-axis plane $[x_1, x_3]$ can also be obtained from the PP+PS=SS method. Picking the offsets (along with the traveltimes) of the two PS-waves corresponding to the same reflection point for a range of the slownesses p_1 allows me to build the function $(\Delta x_{PS})_{x_1}(p_1)$ [equation (3.18)]. This function can then be approximated with a hyperbola whose apex yields the value of x_0. Alternatively, it can be shown that the offset x_0 corresponds to the PS-wave with $p_1 = 0$, whose legs coincide with the zero-offset PP and PS reflections.

3.3.2 Inversion algorithm

I assume that the azimuth of the symmetry-axis plane has been established, for example, from azimuthally varying moveout of P-waves. The general equation of the NMO ellipse has the following form (Grechka & Tsvankin, 1998):

$$V_{\mathrm{nmo}}^{-2}(\alpha) = W_{11}\cos^2\alpha + 2\,W_{12}\sin\alpha\cos\alpha + W_{22}\sin^2\alpha\,, \tag{3.22}$$

where $W_{ij} \equiv \tau_0 \, \partial p_i / \partial x_j$ $(i,j = 1,2)$, $\tau_0 \equiv t_0/2$ is the one-way zero-offset traveltime, and p_1 and p_2 are the horizontal slowness components for one-way rays from the zero-offset reflection point to the surface; all derivatives are evaluated at the CMP location. For a homogeneous horizontal layer, the matrix $\boldsymbol{W}$ can be represented as (Grechka et al., 1999a)

$$\boldsymbol{W} = \frac{-q}{q_{,11}\, q_{,22} - q_{,12}^2} \begin{pmatrix} q_{,22} & q_{,12} \\ -q_{,12} & q_{,11} \end{pmatrix}, \tag{3.23}$$

where $q \equiv q(p_1, p_2)$ is the vertical slowness and $q_{,ij} \equiv \partial^2 q / (\partial p_i \partial p_j)$. As mentioned above, the slowness vector of the zero-offset ray for a horizontal layer is vertical, so the derivatives are computed for $p_1 = p_2 = 0$.

If the medium has a vertical symmetry plane, one of the axes of the NMO ellipse is parallel to the symmetry-plane direction (Grechka & Tsvankin, 1998). For a TTI layer with the symmetry axis confined to the $[x_1, x_3]$-plane, the terms $q_{,12}$ and W_{12} [equation (3.23)] vanish, while W_{11} and W_{22} define the semiaxes of the NMO ellipse (3.22). Therefore, the orientation of the NMO ellipse of the recorded PP-waves or constructed SS-waves can be used to find the azimuth of the symmetry-axis plane $[x_1, x_3]$.

Then, as described above, processing of 2D multicomponent data in the symmetry-axis plane produces the following data vector $\boldsymbol{d}$:

$$\boldsymbol{d} \equiv \left\{ V_{\mathrm{nmo,P}}\,,\; t_{P0}\,,\; V_{\mathrm{nmo,S}}\,,\; t_{S0}\,,\; \Delta t_{PS}(p_1, 0)\,,\; x_{\min}(\alpha = 0^\circ) \right\}, \tag{3.24}$$

where the NMO velocities of pure modes are measured in the symmetry-axis plane. Although $\Delta t_{PS}(p, 0)$ denotes multiple measurements of the asymmetry factor for the available range of the horizontal slownesses p_1, equation (3.13) indicates that the moveout asymmetry in the $[x_1, x_3]$-plane may constrain only one combination of the layer parameters.

Analytic expressions for $\Delta t_{PS}(p_1, 0)$ and $x_0 = x_{\min}(\alpha = 0^\circ)$ needed to model these quantities in the inversion algorithm were introduced in the previous section. The NMO velocities $V_{\mathrm{nmo,P}}$ and $V_{\mathrm{nmo,S}}$ in the x_1-direction $(\alpha = 0^\circ)$ can be computed from equation (3.23) with $q_{,12} = 0$:

$$V_{\mathrm{nmo}} = \frac{1}{\sqrt{W_{11}}} = \sqrt{-\frac{q_{,11}}{q}}. \tag{3.25}$$

The model vector $\boldsymbol{m}$ includes the following parameters of the TTI layer:

$$\boldsymbol{m} \equiv \left\{ V_{P0}\,,\; V_{S0}\,,\; \epsilon\,,\; \delta\,,\; \nu,\; z \right\}. \tag{3.26}$$

Thus, six or more [if $\Delta t_{PS}(p_1, 0)$ constrains more than one parameter] independent measurements [equation (3.24)] are controlled by the six model parameters in equation (3.26). To estimate the vector $\boldsymbol{m}$, I applied nonlinear inversion (the Gauss-Newton method) based on exact equations for all components of the data vector (3.24). The misfit (objective)

function minimized by the inversion algorithm is defined as

$$\begin{aligned}\mathcal{F} \equiv\ & w_1 \frac{(V^{\text{calc}}_{\text{nmo,P}} - V^{\text{meas}}_{\text{nmo,P}})^2}{(V^{\text{meas}}_{\text{nmo,P}})^2} + w_2 \frac{(V^{\text{calc}}_{\text{nmo,S}} - V^{\text{meas}}_{\text{nmo,S}})^2}{(V^{\text{meas}}_{\text{nmo,S}})^2} + w_3 \frac{(t^{\text{calc}}_{P0} - t^{\text{meas}}_{P0})^2}{(t^{\text{meas}}_{P0})^2} \\ +\ & w_4 \frac{(t^{\text{calc}}_{S0} - t^{\text{meas}}_{S0})^2}{(t^{\text{meas}}_{S0})^2} + w_5 \frac{\sum_0^p (\Delta t^{\text{calc}}_{PS} - \Delta t^{\text{meas}}_{PS})^2}{(\sum_0^p \Delta t^{\text{meas}}_{PS})^2} + w_6 \frac{(x^{\text{calc}}_0 - x^{\text{meas}}_0)^2}{(x^{\text{meas}}_0)^2},\end{aligned} \tag{3.27}$$

where the superscripts "calc" and "meas" denote the calculated and measured quantities, respectively, and p is the maximum value of the horizontal slowness p_1. The weighting coefficients w_i were generally set to unity. I observed, however, that assigning substantially larger weights to the asymmetry attributes typically leads to a faster convergence of the algorithm.

Since the exact equations for the model parameters are nonlinear and the misfit function contains local minima, selection of the starting model may have a significant influence on the performance of the algorithm. I based the initial guesses for the vertical velocities and anisotropic coefficients on the isotropic relationships,

$$V_{P0} = V_{\text{nmo,P}}\,,\ V_{S0} = V_{\text{nmo,S}}\,,\ \epsilon = 0,\ \delta = 0,\ z = V_{\text{nmo,P}}\, t_{P0}/2\,. \tag{3.28}$$

My numerical tests show that if the starting model is isotropic [equation (3.28)] and the initial tilt ν is set to 0° or 90°, the algorithm either does not converge toward the correct solution or the convergence is extremely slow. This happens because the initial values of the partial derivatives of the objective function (3.27) with respect to several model parameters go to zero. The convergence can be significantly improved by keeping the initial $\epsilon = \delta = 0$, but starting with an intermediate tilt ν that is as close as possible to the actual value. For example, if the anisotropy is known to be caused by subvertical fractures, a good choice of the initial tilt is $\nu = 70 - 80°$.

3.3.3 Numerical examples

I examined the uniqueness and stability of the inversion by applying the algorithm to noise-contaminated input data. I analyzed a representative set of TTI models with a wide range of the tilt angles ν of the symmetry axis.

Models with tilt $\nu > 60°$.- TTI models with a significant tilt of the symmetry axis can be considered typical for dipping fracture sets because fracture planes seldom deviate far from the vertical (Angerer et al., 2002). For a system of *vertical* penny-shaped cracks in isotropic host rock, the symmetry axis is horizontal ($\nu = 90°$), and the medium becomes HTI.

The tilt $\nu = 70°$ of the symmetry axis in Figure 3.7 is quite favorable for the inversion based on the moveout asymmetry attributes of PS-waves. Here and in the other examples below, the data vector $\boldsymbol{d}$ [equation (3.24)] was generated using the exact equations and contaminated by Gaussian noise. The inversion was carried out for 100 realizations of the

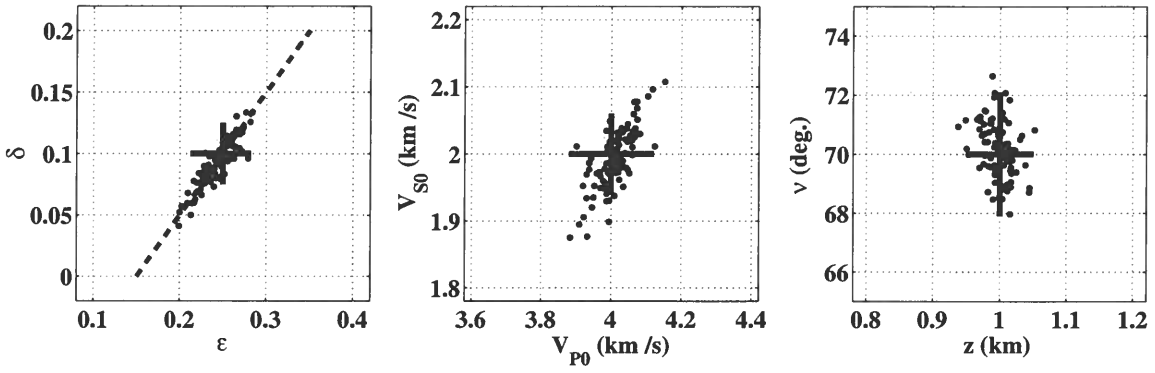

Figure 3.7. Inverted parameters (dots) of a horizontal TTI layer obtained from 2D PP and PS data in the symmetry-axis plane. The correct model parameters ($V_{P0} = 4$ km/s, $V_{S0} = 2$ km/s, $\epsilon = 0.25$, $\delta = 0.1$, $\nu = 70°$, $z = 1$ km) are marked by the crosses. The dashed line on the $[\epsilon, \delta]$ plot corresponds to the correct value of the difference $(\epsilon - \delta)$. The input data were contaminated by Gaussian noise with the standard deviations of 2% for the NMO velocities, 0.5% for the zero-offset traveltimes, and 2% for the PS-wave asymmetry attributes.

input data, which allowed me to compute the standard deviations of the estimated parameters. The initial guess was based on equation (3.28), with the tilt picked randomly from the interval $50° - 85°$. The model vector $\boldsymbol{m}$ [equation (3.26)] was estimated by minimizing the objective function specified in equation (3.27), as discussed in the previous section.

Figure 3.7 indicates that the inversion results are unbiased, and the noise is not amplified by the parameter-estimation procedure. The standard deviations are close to 0.02 for ϵ and δ, 1% for V_{P0}, 2% for V_{S0} and z, and 1° for ν. The best-constrained parameter combination is the difference $(\epsilon - \delta)$, which controls the time-asymmetry factor in the slowness domain [equations (3.12) and (3.13)] and has a strong influence on the NMO velocity of the constructed SS-waves. Although the traveltimes of the PP- and PS-waves in the symmetry-axis plane are sufficient for estimating all relevant TTI parameters, the addition of wide-azimuth data increases the accuracy of the inversion in the presence of noise.

It should be emphasized that the parameter estimation is feasible only if the asymmetry information of the PS-wave is included in the inversion algorithm. The offset x_0 of the PS-wave moveout minimum for the model from Figure 3.7 reaches about 1/3 of the depth z, and the asymmetry factor Δt_{PS} for the offset $x = 2z$ is about 15% of the zero-offset PS traveltime. Such a large magnitude of the traveltime asymmetry helps to constrain the tilt of the symmetry axis and the anisotropic coefficients. Without the asymmetry information the inversion becomes unstable, even if the 2D data in the vertical symmetry plane are supplemented with the NMO ellipses of the PP- and SS-waves (Grechka & Tsvankin, 2000; Grechka et al., 2002a).

Since the traveltime asymmetry is estimated from the relatively small difference of two time measurements, it is important to evaluate the sensitivity of the inversion results to

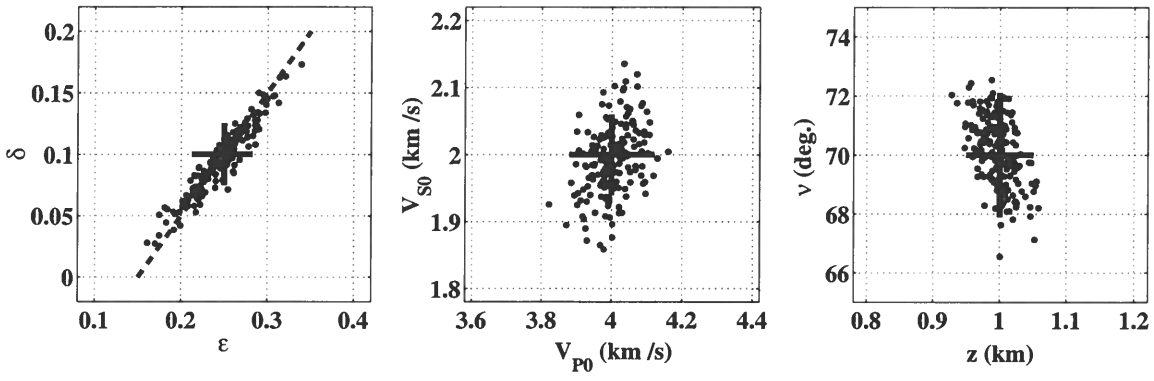

Figure 3.8. Same as Figure 3.7, but the standard deviations of the Gaussian noise are increased to 1% for the zero-offset traveltimes and 4% for the asymmetry attributes of PS-waves (the standard deviations for the NMO velocities remain unchanged at 2%).

larger errors in the PS-wave asymmetry attributes. For the test in Figure 3.8 the standard deviations of Δt_{PS} and x_0 were increased from 2% to 4% (also, the deviations of the zero-offset times were increased to 1%). Despite the somewhat higher scatter of the inverted parameters, the standard deviations do not exceed 0.03 for ϵ and δ, 2% for V_{P0}, 3% for V_{S0} and z, and 1° for ν. Clearly, the inversion remains sufficiently stable for realistic levels of distortions in the asymmetry attributes.

For HTI media ($\nu = 90°$) the PS-wave moveout is symmetric, and the 2D inversion in the symmetry-axis plane cannot constrain the medium parameters. However, even a small (10°) deviation of the symmetry axis from the horizontal plane creates a measurable moveout asymmetry. For the model from Figure 3.9, the offset x_0 is close to 20% of the depth z, and the factor Δt_{PS} reaches about 7% of the zero-offset PS traveltime for $x = 2z$. Since the magnitude of the asymmetry attributes is small compared to the model with $\nu = 70°$, the error in the asymmetry attributes is expected to be higher. Figure 3.9 shows the inversion result when the error in Δt_{PS} and x_0 is increased from 2% to 6%. Still, the model parameters are reasonably well constrained with the standard deviations less than 0.04 for ϵ and δ, 2% for V_{P0}, 3% for V_{S0} and z, and 1° for ν. If the axis deviates by less than 10° from either the vertical or horizontal direction, then the asymmetry attributes are too small to be estimated with reasonable accuracy, and the inversion breaks down. In all numerical tests below, the standard deviation of the noise is the same as that in Figure 3.7.

Models with intermediate tilt .- The moveout asymmetry factor in the slowness domain is small not only for near-vertical and near-horizontal orientations of the symmetry axis, but also for tilts ν close to 45° [equation (3.13)]. The model of a horizontal TTI layer with $35° < \nu < 55°$ can be used to describe reflections from a horizontal interface beneath dipping shale layers in fold-and-thrust belts, such as the Canadian Foothills (e.g., Isaac & Lawton, 1999).

Figure 3.10 helps to assess the feasibility of the inversion for a tilt of 50°. Although the

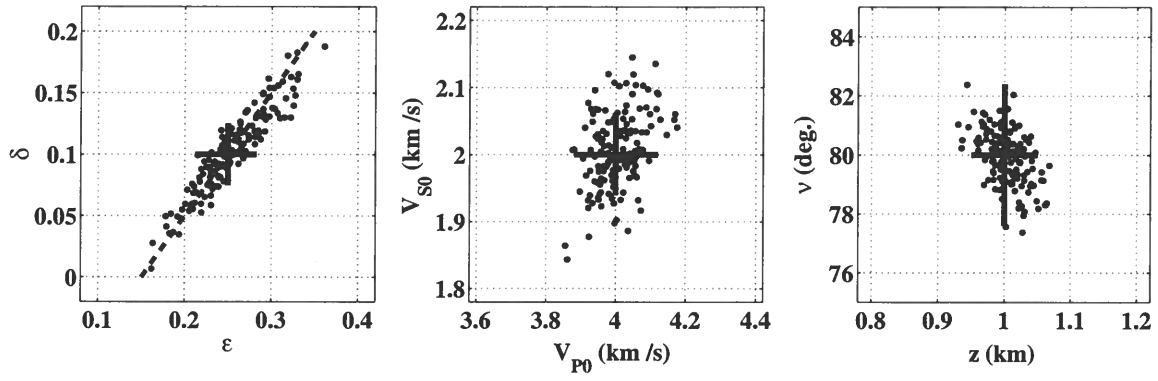

Figure 3.9. Inversion results for a model with the same parameters as those in Figure 3.7 except for the tilt $\nu = 80°$. The standard deviations of Gaussian noise here are 2% for the NMO velocities, 0.5% for the zero-offset traveltimes, and 6% for the PS-wave asymmetry attributes.

asymmetry in the offset domain for intermediate tilts is substantial (x_0 is about 34% of z), the inverted parameters are biased and exhibit significant scatter. Analysis of the inversion results shows that many estimated models correspond to local minima of the objective (misfit) function and do not fit the input data within the noise level.

I addressed the problem with local minima by modifying the inversion algorithm. If the search stops at a minimum where the model does not fit the data within the standard deviation of the noise (2% for the NMO velocities and the asymmetry attributes and 0.5% for the zero-offset traveltimes), then the model is perturbed to resume the search from a different point in the parameter space. Figure 3.11 shows that the modified algorithm produces stable inversion results for $\nu = 50°$, with standard deviations comparable to those for $\nu = 70°$ (Figure 3.7).

Models with mild tilt .- For completeness, here I discuss the parameter-estimation results for mild tilts ν. While such models are not plausible if the anisotropy is caused by dipping fractures, they may be adequate for effective TTI models formed by progradational sequences (e.g., Sarg & Schuelke, 2003).

The scatter in the inversion results for a tilt of 20° is slightly higher than that for large tilts, but the standard deviations are still less than 0.03 for ϵ and δ, 3% for V_{P0}, V_{S0} and z, and 2° for ν (Figure 3.12). As expected, the parameter estimation breaks down as the model approaches VTI, and the tilt ν becomes smaller than 10°. Not only do the standard deviations rapidly increase when $\nu \to 0°$, but the parameter estimates become noticeably biased. For the model with $\nu = 5°$ in Figure 3.13, the bias is about 0.05 for ϵ, 0.03 for δ, and 4% for V_{P0}, V_{S0}, and z. Only the tilt is relatively well-constrained by the data because of the sensitivity of the asymmetry attributes to ν.

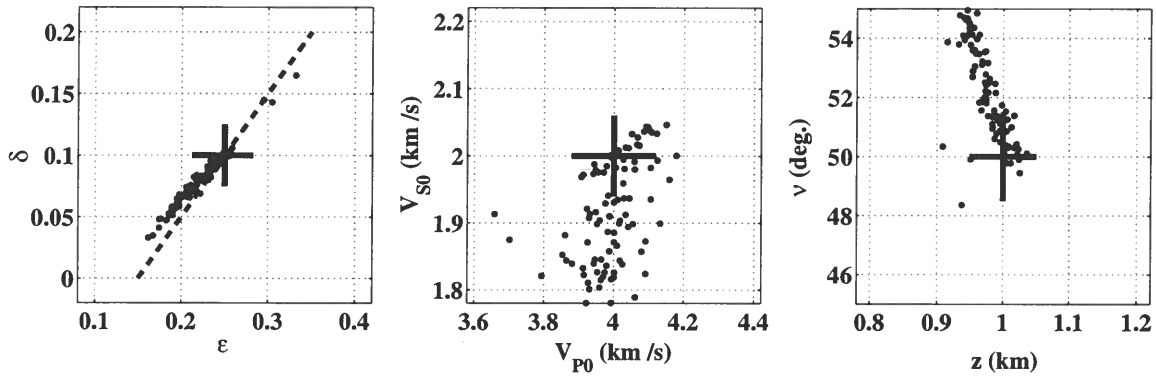

Figure 3.10. Inversion results for a model with the same parameters as those in Figure 3.7 except for the tilt $\nu = 50°$.

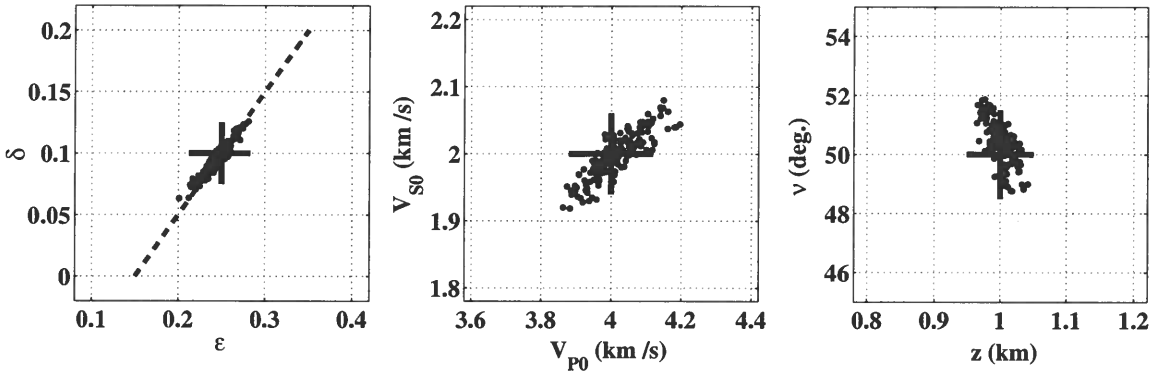

Figure 3.11. Same as Figure 3.10, but the inversion algorithm is modified to avoid local minima.

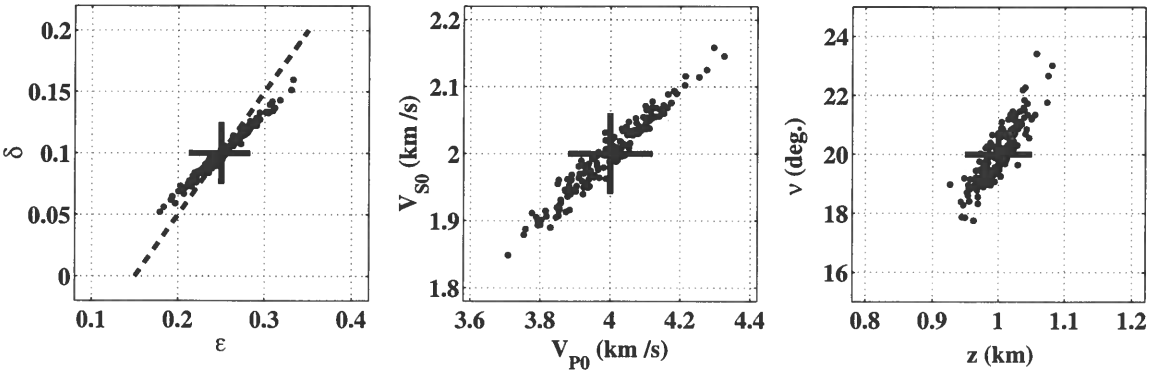

Figure 3.12. Inversion results for a model with the same parameters as those in Figure 3.7 except for the tilt $\nu = 20°$.

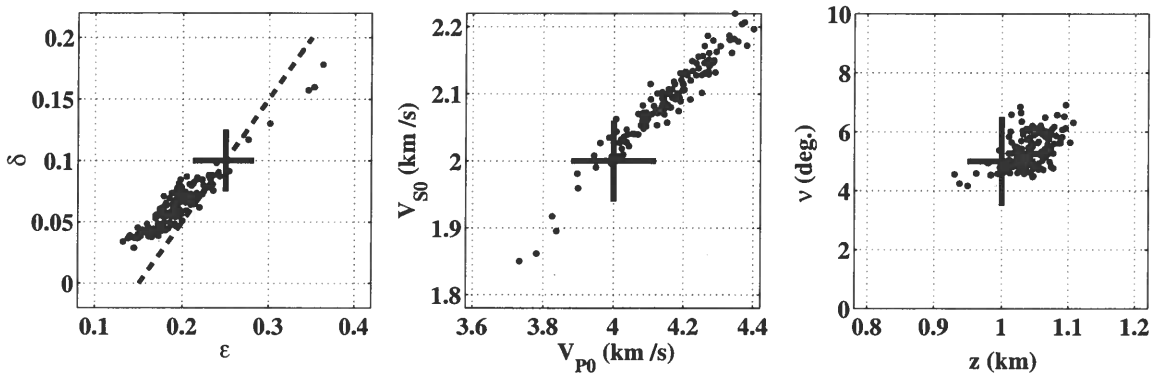

Figure 3.13. Inversion results for a model with the same parameters as those in Figure 3.7 except for the tilt $\nu = 5°$.

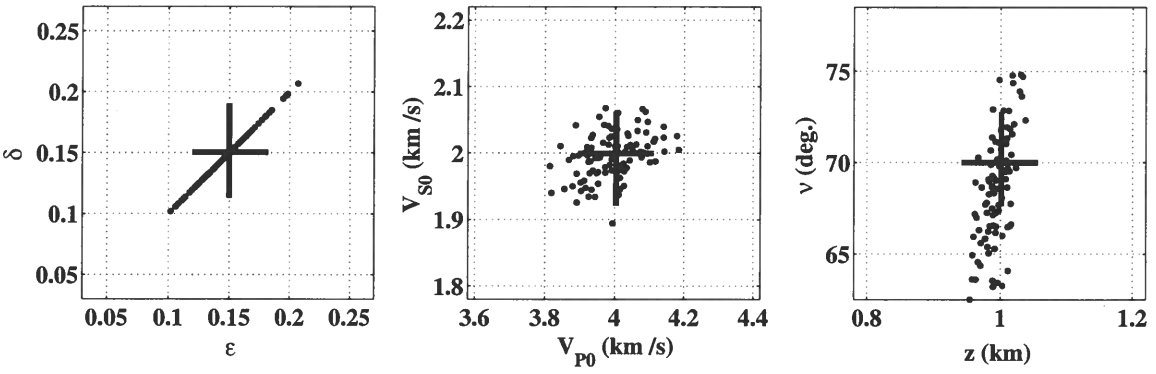

Figure 3.14. Inversion results for an elliptically anisotropic TTI layer with the same parameters as those in Figure 3.7 except for $\epsilon = \delta = 0.2$.

Elliptically anisotropic models .- According to my analytic results, the moveout asymmetry of PS-waves in the slowness domain vanishes if the medium is elliptically anisotropic (i.e., $\epsilon = \delta$). In the offset domain, however, PS moveout in elliptical media remains asymmetric, and the offset $x_0 \neq 0$. Therefore, the combination of the asymmetry attributes used in my inversion algorithm can help to separate elliptical TTI models from VTI and HTI, for which PS moveout is symmetric in any domain. As illustrated by Figure 3.14, all parameters of an elliptically anisotropic layer except for the tilt (70°) are well constrained, and the standard deviations are less than 0.03 for $\epsilon = \delta$ and less than 2% for V_{P0}, V_{S0}, and z. The points on the $[\epsilon, \delta]$ plot are almost perfectly aligned along the $\epsilon = \delta$ line, which indicates that the algorithm is able to identify elliptical anisotropy. The estimates of ν, however, are more scattered (the standard deviation reaches 5°) than those for anelliptical models with the same tilt, and the average ν is biased by about 2°.

3.4 Summary

Here, I presented a modification of the PP+PS=SS method designed to supplement the computed SS data with such asymmetry attributes of the converted waves as the difference Δt_{PS} between the "reciprocal" traveltimes in the slowness domain and the offset $x_{\min}$ of the traveltime minimum in CMP geometry. The new algorithm was applied to the inversion of multicomponent data for a horizontal TTI (transversely isotropic with a tilted symmetry axis) layer – the model used to describe the effective anisotropy caused by parallel, dipping, penny-shaped cracks, dipping shale beds, or progradational sequences.

The weak-anisotropy approximation helped to obtain concise expressions for the azimuthally varying asymmetry attributes of PSV-waves in terms of the tilt ν of the symmetry axis and the anisotropic coefficients ϵ and δ. For VTI ($\nu = 0°$) and HTI ($\nu = 90°$) media these asymmetry attributes vanish. The asymmetry factor Δt_{PS} includes equal contributions from the P- and S-legs of the PS-wave and, in the linear approximation, is proportional to the parameter $\eta \approx \epsilon - \delta$. Therefore, it vanishes for elliptical media ($\epsilon = \delta$). In contrast, the offset $x_{\min}$ of the minimum traveltime that quantifies the PS-wave offset asymmetry (Δx_{PS}) depends on ϵ and δ individually and does not go to zero in elliptical media. The asymmetry attributes also exhibit a pronounced azimuthal variation from the maximum in the symmetry-axis plane to vanishing values in the orthogonal direction. The azimuthal variation of $x_{\min}$ is described by a circle with the center in the symmetry-axis plane.

The asymmetry attributes of PS(PSV)-waves were combined with the NMO velocities and zero-offset traveltimes of PP-waves and the constructed SS-waves in a nonlinear inversion algorithm. Although it is desirable to have a wide range of source-receiver azimuths, the parameter estimation can be performed using just 2D data acquired in the symmetry-axis plane. The orientation of this plane, however, has to be determined beforehand from either the pure-mode NMO ellipses (i.e., from wide-azimuth data) or the PS-wave polarization at small offsets.

To assess the stability of the inversion, the algorithm was applied to multiple realizations of the input data contaminated by zero-mean Gaussian noise. Without the asymmetry information the parameter estimation for this model is strongly nonunique, and a wide range of vastly different models can fit the input data (Grechka & Tsvankin, 2000). Including the PS-wave moveout asymmetry attributes removes this ambiguity and makes the 2D inversion sufficiently stable if the symmetry axis deviates by 10° or more from the vertical (VTI) and horizontal (HTI) directions. Note while PP and PS reflection data do not constrain the vertical velocities, ϵ, and δ in a horizontal VTI layer (Grechka & Tsvankin, 2002b), the inversion for an HTI layer can be accomplished using wide-azimuth PP and PS (or SS) reflection traveltimes (Tsvankin, 1997; Bakulin et al., 2000; Grechka et al., 2002a). Wide-azimuth data also help to obtain more accurate estimates of the tilt for elliptical ($\eta = 0$) TTI models.

This chapter has been submitted for publication in Geophysics (Dewangan & Tsvankin, 2004a).

Chapter 4

Parameter estimation using PS-wave moveout asymmetry: Dipping TTI layer

Here, the methodology introduced in Chapter 3 is extended to the inversion of multi-component (PP and PSV) data acquired above a TTI layer with the symmetry axis orthogonal to the layer's bottom. The moveout asymmetry of PS-waves in this model is caused by both the reflector dip ϕ and the tilt ν of the symmetry axis, which are set equal to each other. The modified PP+PS=SS method yields the PSV-wave asymmetry attributes, which I combine in the inversion procedure with the NMO velocities, zero-offset traveltimes, and reflection time slopes of the pure PP and SS reflections. The inversion algorithm is designed to estimate the P- and S-wave velocities in the symmetry direction (V_{P0} and V_{S0}, respectively), Thomsen (1986) anisotropic parameters ϵ and δ, the tilt ν, and the thickness of the layer using solely reflection traveltimes. Simple analytic approximations for the time and offset asymmetry factors of the PSV-wave demonstrate that independent information for the inversion is contained in higher-order terms in offset. Numerical tests for various errors in the asymmetry attributes help to evaluate the stability of estimating each parameter for a wide range of plausible TTI models.

2D inversion of P-wave normal-moveout (NMO) velocities for the parameters of dipping TTI layers with the symmetry axis perpendicular to the bedding was discussed by Grechka et al. (2001). Although their method performed well on physical-modeling data, it is based on a number of simplifying assumptions about the model (e.g., the medium around the TTI layer has to be isotropic and homogeneous). Also, in addition to reflections from the TTI layer itself, the algorithm of (Grechka et al., 2001) requires reflection data from a deeper horizontal interface. It should be emphasized that, if the dip and tilt of the symmetry axis are smaller than 40°, none of the existing methods can yield stable parameter estimates using PP and PS reflections from a TTI layer.

4.1 Asymmetric PS-wave moveout in a dipping TTI layer

If the medium is anisotropic without a horizontal symmetry plane or laterally heterogeneous, the moveout of PS-waves becomes asymmetric.

4.1.1 Moveout asymmetry from the PP+PS=SS method

For laterally heterogeneous models, such as a layer above a dipping reflector, the moveout of converted waves becomes asymmetric even in the absence of anisotropy (e.g.,

Tsvankin & Grechka, 2000). In principle, the time asymmetry can be measured in the offset domain by interchanging the source and receiver positions. However, since these *reciprocal* traveltimes correspond to different conversion points, offset-domain measurements of the moveout asymmetry may be distorted by the influence of the reflector shape.

An important advantage of estimating the asymmetry from the modified PP+PS=SS method is that each of the reciprocal PS events is guaranteed to have the same conversion point. Indeed, the method is designed to identify two PS-waves converted at the reflection point of a given PP-arrival (see Figure 2.1 in Chapter 2). I consider a homogeneous TTI layer with the axis of symmetry orthogonal to the layer's bottom (reflector), which may have an arbitrary dip. Then the symmetry axis is confined to the dip plane of the reflector, which represents the only vertical symmetry plane of the model. The x_1-axis of the Cartesian coordinate system points in the updip direction of the reflector (Figure F.1).

According to Snell's law, the projection of the slowness vector onto the reflector should be the same for all reflected waves. If the slowness components in the dip and strike directions of the reflecting interface are denoted by p_{int1} and p_{int2} (both p_{int1} and p_{int2} are confined to the reflector plane), the difference between the traveltimes of the two PS-waves with the same conversion point can be represented as

$$\Delta t_{PS} = t_{PS}(p_{\text{int1}}, p_{\text{int2}}) - t_{PS}(-p_{\text{int1}}, -p_{\text{int2}}) = \Delta t_P + \Delta t_S, \tag{4.1}$$

where Δt_P and Δt_S are the contributions to Δt_{PS} from the P- and S-legs of the PS ray, respectively. Equation (4.1) has the same form as the expression for Δt_{PS} in Chapter 3, where the slowness components are computed for a *horizontal* interface.

Following Chapter 3, I also define the measure of asymmetry in the offset $\boldsymbol{x}$ [equation (F.4)] using the two PS-waves with the opposite signs of the slowness projection onto the reflector:

$$\boldsymbol{\Delta x}_{PS} = \boldsymbol{x}_{PS}(p_{\text{int1}}, p_{\text{int2}}) + \boldsymbol{x}_{PS}(-p_{\text{int1}}, -p_{\text{int2}}). \tag{4.2}$$

To gain insight into the influence of the model parameters on the time and offset asymmetry factors, I analyze approximate expressions for Δt_{PS} and $\boldsymbol{\Delta x}_{PS}$ obtained in Appendices F and G under the assumption of weak anisotropy ($|\epsilon| \ll 1$ and $|\delta| \ll 1$) and small offset-to-depth ratio ($|p_{\text{int1}} V_{P0}| \ll 1$ and $|p_{\text{int2}} V_{P0}| \ll 1$). As shown in Appendix F, the approximate time asymmetry factor Δt_{PS} for the PSV-wave in the symmetry-axis plane (i.e., for the azimuth $\alpha = 0$) is given by

$$\Delta t_{PS} = \frac{-2 \sin\nu}{V_{S0}} \chi \, x_{SS} + \frac{(1+4\epsilon) V_{P0}^2 \sin\nu \cos^2\nu}{4 (1+2\sigma)^3 V_{S0}^3 z_d^2} \, x_{SS}^3, \tag{4.3}$$

where $\sigma \equiv (V_{P0}/V_{S0})^2 (\epsilon - \delta)$, and $\chi \equiv (\sigma - \delta)/(1+2\sigma)$ are the anisotropic parameters that can be obtained from the zero-offset traveltimes and NMO velocities of P- and SV-waves in layer-cake VTI media as discussed in Chapter 2, and z_d is the normal distance from the common midpoint (CMP) to the reflector. As expected, the asymmetry factor Δt_{PS} vanishes for zero tilt and dip ($\nu = 0$) when the medium becomes VTI. Note that PS moveout is asymmetric even in a dipping isotropic layer, where the cubic [equation (4.3)]

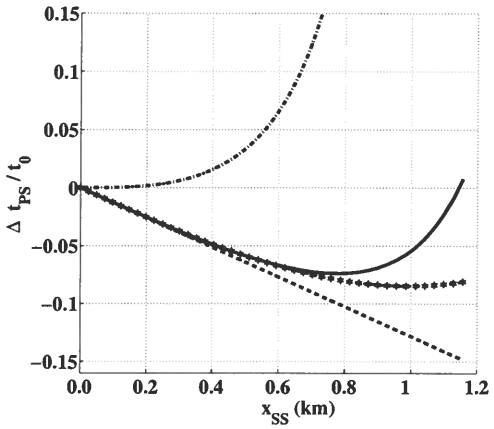

Figure 4.1. Time asymmetry factor Δt_{PS} for the PSV-wave in the symmetry-axis plane of a dipping TTI layer. The exact Δt_{PS} is marked by the solid line, the weak-anisotropy approximation (4.3) by the dashed line with stars, the linear term in equation (4.3) by the dashed line, and Δt_{PS} in the reference isotropic model by the dash-dotted line. The factor Δt_{PS} is normalized by the zero-offset traveltime of the PS-wave. The medium parameters are $V_{P0} = 4$ km/s, $V_{S0} = 2$ km/s, $\epsilon = 0.25$, $\delta = 0.1$, $\nu = 25°$, and $z_d = 1$ km. The maximum offset-to-depth ratio of the PP and PS data is close to two.

and higher-order terms in x_{SS} do not go to zero.

Figure 4.1 shows the factor Δt_{PS} computed for a typical dipping TTI model from the exact equations (4.1) and (F.1), as well as from the weak-anisotropy approximation (4.3). While the initial slope of the factor Δt_{PS} is well-described by the linear term in equation (4.3) even for large absolute values of δ and σ, the cubic and higher-order terms make a significant contribution at far offsets that correspond to offset-to-depth ratios of about two for the PP and PS data. Although the accuracy of the weak-anisotropy approximation (4.3) decreases with offset, it correctly reproduces the trend of $\Delta t_{PS}(x_{SS})$ for moderate offset-to-depth ratio.

The weak-anisotropy approximation for the azimuthally-varying offset asymmetry factor [equation (4.2)] is derived in Appendix G. In the symmetry-axis plane ($\alpha = 0$), the approximate Δx_{PS} takes the following form:

$$\Delta x_{PS} = \frac{\sin\nu}{2\,z_d}\left[\frac{(1+4\delta)\,V_{P0}^2}{(1+4\sigma)\,V_{S0}^2} - 1\right] x_{SS}^2 \,. \tag{4.4}$$

Equation (4.4) indicates that for typical TI models with $\sigma \gg \delta$, the influence of anisotropy *reduces* the offset asymmetry factor, which is confirmed by the numerical results in Figure 4.2. Weak-anisotropy approximation (4.4) deteriorates with increasing offset because the exact solution is influenced by the quartic term in x_{SS} even for offset-to-depth ratios of the PS-wave close to two. For the moderately anisotropic model in Figure 4.2, the magni-

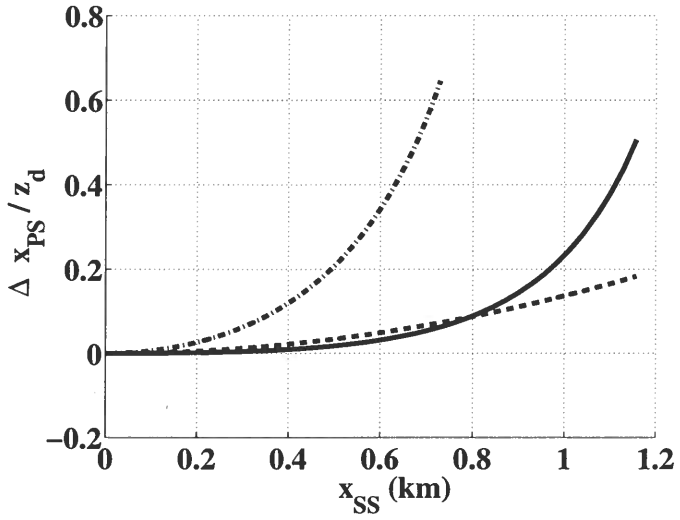

Figure 4.2. Offset asymmetry factor Δx_{PS} for the PSV-wave in the symmetry-axis plane. The exact Δx_{PS} is marked by the solid line, the weak-anisotropy approximation (4.4) by the dashed line, and Δx_{PS} in the reference isotropic model by the dash-dotted line. The factor Δx_{PS} is normalized by the distance z_d between the CMP and the reflector. The medium parameters are the same as those in Figure 4.1.

tude of the factor Δx_{PS} reaches up to 50% of the CMP–to–reflector distance. As discussed below, however, the leading (x_{SS}^2) term in equation (4.4) does not contain independent information for estimating the model parameters.

Because of the influence of moveout asymmetry, the minimum traveltime of PS-wave on a CMP gather is not recorded at zero offset (Tsvankin & Grechka, 2000, Chapter 3). An analytic expression for the azimuthally-dependent offset $x_{\min}(\alpha)$ of the traveltime minimum is obtained in Appendix G by assuming a small dip ν and linearizing the exact equation in the anisotropic parameters. In the symmetry-axis plane, the approximation for $x_{\min}$ reduces to

$$x_{\min}(\alpha = 0) = \frac{z_d}{2\,\cos^2\nu}\left[\frac{\sin\nu}{V_{P0}} - \frac{\sin\nu}{V_{S0}}\right]\Big[V_{P0}\,(1+2\delta) + V_{S0}\,(1+2\sigma)\Big]. \qquad (4.5)$$

Although anisotropy does make a substantial contribution to $x_{\min}(\alpha = 0)$, all terms in equation (4.5) can be found from the NMO velocities, zero-offset traveltimes, and reflection time slopes of the pure (PP and SS) reflection modes (see below).

4.2 Parameter estimation

The effectiveness of parameter-estimation algorithm is evaluated in the presence of random Gaussian noise.

4.2.1 Data processing

As discussed in Chapter 3, the main prerequisite for successful application of the inversion algorithm introduced here is acquisition of long-offset PP and PS data. First, offset-to-depth ratios of at least two for the recorded PP- and PS-waves are needed for stable estimation of the NMO velocity for the constructed SS arrivals. Second, acquiring PS data for a wide range of offsets ensures a sufficiently large magnitude of the moveout asymmetry attributes used in the parameter estimation.

The data processing flow is similar to that described in Chapter 3. The PP+PS=SS method yields quasi-shear data, whose reflection moveout can be used to estimate the stacking (NMO) velocity ($V_{\text{nmo,S}}$), zero-offset traveltime (t_{S0}), and time slope on zero-offset section (i.e., the ray parameter p_{S0}) for the SS-waves. The same parameters for the recorded PP-waves ($V_{\text{nmo,P}}$, t_{P0}, and p_{P0}) can be obtained from conventional hyperbolic semblance analysis. For wide-azimuth data, the NMO velocities of the PP- and SS-waves are replaced by the NMO ellipses determined from azimuthal moveout analysis (Grechka & Tsvankin, 1999, Chapter 3). Then I combine the moveout parameters of the pure PP ad SS reflections with the two PS-wave asymmetry attributes obtained from a modified PP+PS=SS method: Δt_{PS} [equations (4.1) and (4.3)] and Δx_{PS} [equations (4.2) and (4.4)]. The offset x_{min} [equation (4.5)] that was used in Chapter 3 does not contain any additional information about the model and, therefore, is not included in the inversion.

4.2.2 Inversion algorithm

Suppose that both PP and PSV reflection data are acquired in a 3D survey for a wide range of azimuths, and the PP+PS=SS method is used to generate SS reflections and the asymmetry attributes of the PSV-wave. Then the orientation of the symmetry-axis plane can be established from the NMO ellipses of the pure modes, whose axes are aligned with the dip and strike directions of the reflector. Processing of the PP-waves yields the semi-axes of the P-wave NMO ellipse ($V^{\text{dip}}_{\text{nmo,P}}$ and $V^{\text{strike}}_{\text{nmo,P}}$), zero-offset traveltime, and time slope on the zero-offset section:

$$V^{\text{dip}}_{\text{nmo,P}} = \frac{V_{P0}\sqrt{1+2\delta}}{\cos\nu}, \quad V^{\text{strike}}_{\text{nmo,P}} = V_{P0}\sqrt{1+2\delta}, \tag{4.6}$$

$$t_{P0} = \frac{z_d}{V_{P0}}, \tag{4.7}$$

$$p_{P0} = \frac{\sin\nu}{V_{P0}}. \tag{4.8}$$

The velocity $V^{\text{dip}}_{\text{nmo,P}}$ for the TTI model with the symmetry axis orthogonal to the reflector is derived in Tsvankin (1995, 2001); I found the strike component of the NMO ellipse in a similar way. The expressions for t_{P0} and p_{P0} are obtained using the fact that the zero-offset ray in my model travels along the symmetry axis.

The corresponding attributes for the SS-wave can be estimated from the computed SS

data:

$$V_{\rm nmo,S}^{\rm dip} = \frac{V_{S0}\sqrt{1+2\sigma}}{\cos\nu}, \quad V_{\rm nmo,S}^{\rm strike} = V_{S0}\sqrt{1+2\sigma}, \tag{4.9}$$

$$t_{S0} = \frac{z_d}{V_{S0}}, \tag{4.10}$$

$$p_{S0} = \frac{\sin\nu}{V_{S0}}. \tag{4.11}$$

The model vector for the TTI layer includes the following components:

$$\boldsymbol{m} \equiv \left\{V_{P0}\,,\, V_{S0}\,,\, \epsilon\,,\, \delta\,,\, \nu=\phi,\, z_d\right\}, \tag{4.12}$$

where the tilt ν of the symmetry axis is taken to be equal to the reflector dip ϕ. For noise-free data, all six model parameters can be recovered uniquely using the NMO velocities, zero-offset traveltimes, and zero-offset time slopes of the PP- and SS-waves. Indeed, the tilt ν can be found from the ratio of the NMO velocities of either wave in the dip and strike directions, which allows me to obtain the vertical velocities V_{P0} and V_{S0} from the ray parameters p_{P0} and p_{S0}. Finally, the distance z_d and parameters ϵ and δ can be inferred from the zero-offset times and NMO ellipses. In the presence of noise, however, estimation of the tilt from the ratio of the NMO velocities is highly unstable for small and moderate values of ν.

This instability can be illustrated by computing the range of possible tilt values for the NMO velocities contaminated by Gaussian noise with a standard deviation of 2% (Figure 4.3). The estimation of tilt is unbiased with the distribution centered at the correct value ($\nu = 25°$), and has standard deviation of about 3.5°. According to the sensitivity plots in Figure 4.4 below, such a scatter in ν is sufficient to cause unacceptably large errors in the parameters ϵ and V_{P0} reaching 0.3 and 15%, respectively. Thus, a realistic distortion of 1–2% in the NMO velocities propagates with a significant amplification into the other parameters. This conclusion is also supported by the results of Grechka et al. (2002a), who found the inversion of the PP and SS (SVSV) NMO ellipses, zero-offset times, and reflection time slopes in a dipping TTI layer to be nonunique for tilts and dips smaller than 30–40°.

It is important for practical applications to study the inverse problem for the common case when only 2D data in the symmetry-axis plane are available. The pure-mode data vector in this case has six elements ($V_{\rm nmo,P}^{\rm dip}$, t_{P0}, p_{P0}, $V_{\rm nmo,S}^{\rm dip}$, t_{S0}, and p_{S0}) but only five of them are independent because of the constraint,

$$\frac{p_{S0}}{p_{P0}} = \frac{t_{S0}}{t_{P0}}. \tag{4.13}$$

Since the model vector (4.12) has six parameters, 2D inversion cannot be carried out without additional information, such as the asymmetry attributes of the PS-wave. The results of the previous section, however, indicate that the leading terms in the expressions for asymmetry attributes depend on just the moveout parameters of the pure (PP and SS) modes. Indeed, rewriting equations (4.3), (4.4), and (4.5) in terms of NMO velocities, zero-offset times, and

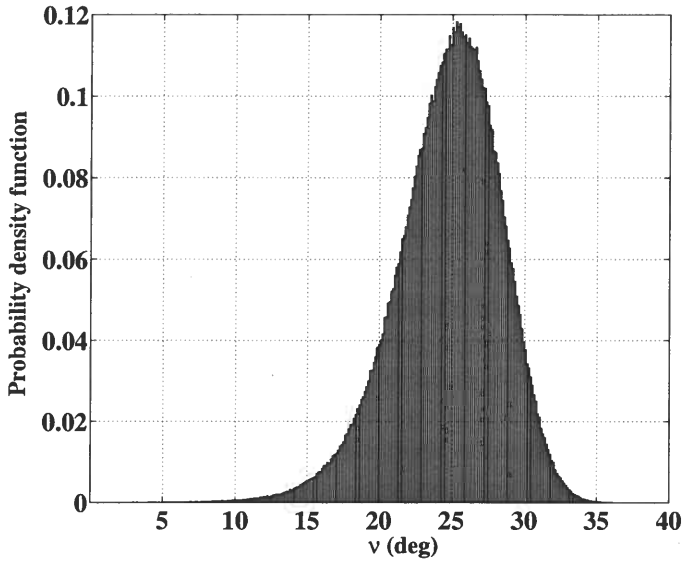

Figure 4.3. Probability density function of the tilt ν computed from equations (4.7) assuming a 2% error in the NMO velocities. The model parameters are the same as those in Figure 4.1.

reflection time slopes of the PP- and SS-waves, I find [only the linear term in equation (4.3) is included]

$$\Delta t_{PS} = p_{S0} \left(\frac{V^2_{\text{nmo,P}}\, t^2_{P0}}{V^2_{\text{nmo,S}}\, t^2_{S0}} - 1 \right) x_{SS} \,, \tag{4.14}$$

$$\Delta x_{PS} = \frac{p_{S0}}{2\, t_{S0}} \left(\frac{V^4_{\text{nmo,P}}\, t^2_{P0}}{V^4_{\text{nmo,S}}\, t^2_{S0}} - 1 \right) x^2_{SS} \,, \tag{4.15}$$

$$x_{\text{min}} = \frac{t_{S0}}{2 p_{S0}} \left(p_{P0} - p_{S0} \right) \left(V^2_{\text{nmo,P}}\, p_{P0} + V^2_{\text{nmo,S}}\, p_{S0} \right) \,, \tag{4.16}$$

The NMO velocities in equations (4.14)–(4.16) are the dip components of the NMO ellipses measured in the symmetry-axis plane.

Clearly, only the departure of the exact asymmetry attributes from the approximations (4.14)–(4.16) can provide independent information for the parameter estimation. As illustrated by Figures 4.1 and 4.2, such departures become substantial at large offsets x_{SS} for both the time and offset asymmetry factors.

I propose the following algorithm to invert the 2D multicomponent data in the symmetry-axis plane for the model vector (4.12):

- For each value of the tilt ν from 0° to 90°, find the model vector using equations (4.6)–(4.11). Restrict the range of plausible tilts by putting reasonable constraints on the

parameter ϵ ($0 \le \epsilon \le 1$; see Figure 4.4 below).

- Taking into account errors in the measured quantities, compute the range of models that fit the data within the noise level for each plausible tilt.

- For each model found in the previous step, compute the asymmetry attributes from the exact equations (4.1) and (4.2).

- Calculate the following misfit function for the asymmetry attributes over the full range of offsets (the maximum offset-to-depth ratio of the PP and PS data should be no smaller than two):

$$\mathcal{F} \equiv \frac{\sum(\Delta t_{PS}^{\text{calc}} - \Delta t_{PS}^{\text{meas}})^2}{(\sum \Delta t_{PS}^{\text{meas}})^2} + \frac{\sum (\Delta x_{PS}^{\text{calc}} - \Delta x_{PS}^{\text{meas}})^2}{(\sum \Delta x_{PS}^{\text{meas}})^2}. \tag{4.17}$$

- Identify the model vector that minimizes this misfit function.

Prior to applying the inversion algorithm, I present the sensitivity analysis for noise-free data. For the test in Figure 4.4, I computed the NMO velocities, zero-offset traveltimes, and reflection time slopes for the PP- and SS-waves from the exact equations for three different values of the tilt ν. Then, for each of the three models I scanned over tilt and computed the model parameters from equations (4.6)–(4.11), as described above. It is clear from Figure 4.4a that the parameter ϵ is highly sensitive to ν, and only a narrow range of tilts produces plausible ϵ values within the interval $0 \le \epsilon \le 1$. The variation of the parameter ϵ with ν is particularly rapid for small tilts corresponding to models approaching VTI. Therefore, putting reasonable constraints on ϵ helps to substantially reduce the range of ν for which I need to compute the asymmetry attributes at the second stage of the inversion procedure.

According to Figure 4.4a, small errors in ν may produce large distortions in estimated ϵ, especially for mild tilts. The problem in resolving ϵ is related to the fact that it contributes to the data vector only indirectly, through the parameter σ [equations (4.6)–(4.11)]. Both σ and δ are more tightly constrained by the input data than is ϵ (see below), with the exception of quasi-VTI models with small ν, for which the inversion as a whole breaks down. In contrast to ϵ, the vertical velocity V_{P0} is much less sensitive to the tilt, especially for moderate and large values of ν (Figure 4.4b). The dependence of the parameters V_{S0} and z_d on ν shows a pattern similar to that for V_{P0}.

To identify the true model from the range of models that fit the pure-mode data, I use the time and offset asymmetry factors in the symmetry-axis plane. Figure 4.5 displays the square-root of the objective (misfit) function [equation (4.17)], which is equivalent to the standard deviation of the error in each of the asymmetry attributes. The expected value of the misfit function can be represented as

$$E[\mathcal{F}] = E\left[\frac{\{\boldsymbol{x} - (\boldsymbol{x} + \alpha\,\boldsymbol{x})\} \cdot \{\boldsymbol{x} - (\boldsymbol{x} + \alpha\,\boldsymbol{x})\}}{\boldsymbol{x} \cdot \boldsymbol{x}}\right] = E[\alpha^2] = \beta_\alpha^2 + (E[\alpha])^2 = \beta_\alpha^2\,,$$

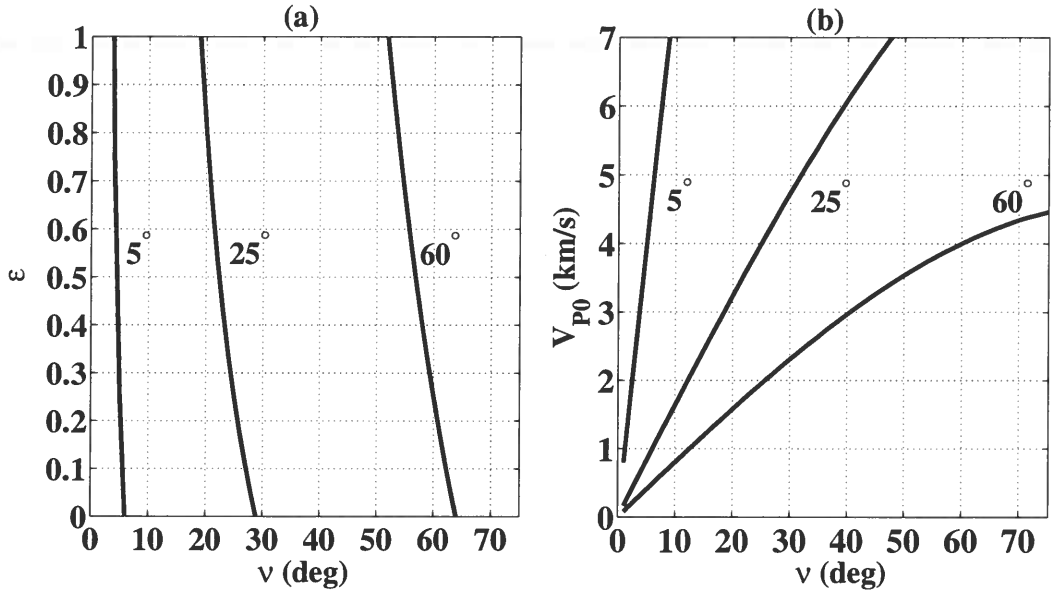

Figure 4.4. Range of possible solutions for the parameters (a) ϵ and (b) V_{P0} obtained from PP- and SS-waves for three values of the tilt: $\nu = 5°$, $25°$ and $60°$. All model parameters except for ν are the same as those in Figure 4.1 ($\epsilon = 0.25$, $V_{P0} = 4$ km/s).

where α is a random variable with zero mean and standard deviation β_α, and $\boldsymbol{x}$ is the vector of either the time or offset asymmetry values for different offsets.

For noise-free data, all model parameters can be estimated uniquely because the misfit function for both Δt_{PS} and Δx_{PS} goes to zero at the correct tilt angle (Figure 4.5). In the presence of noise, the resolution in tilt becomes lower for larger values of ν where the misfit function increases more slowly away from the correct solution. This result is supported by equation (4.3) for the time asymmetry factor Δt_{PS} in which the ratio of the cubic and linear terms in offset decreases with ν. As discussed above, only the cubic and higher-order terms in the equation for Δt_{PS} contain independent information for the inversion. Note that the high resolution in ν for quasi-VTI models with mild tilt does not mean that the rest of the parameters can be estimated with high accuracy. Despite the tight constraints on the tilt provided by both the pure-mode signatures and the asymmetry attributes, not only ϵ, but also δ and the vertical velocities, are too sensitive to tilt for the inversion to be sufficiently stable (see the numerical results below).

Figure 4.5 also shows that the time and offset asymmetry factors provide comparable resolution in tilt, although the factor Δx_{PS} performs somewhat better for relatively large tilts and also for large errors in the asymmetry factors compared to Δt_{PS}. Therefore, the inversion algorithm employs equation (4.17) with equal weights for Δt_{PS} and Δx_{PS}.

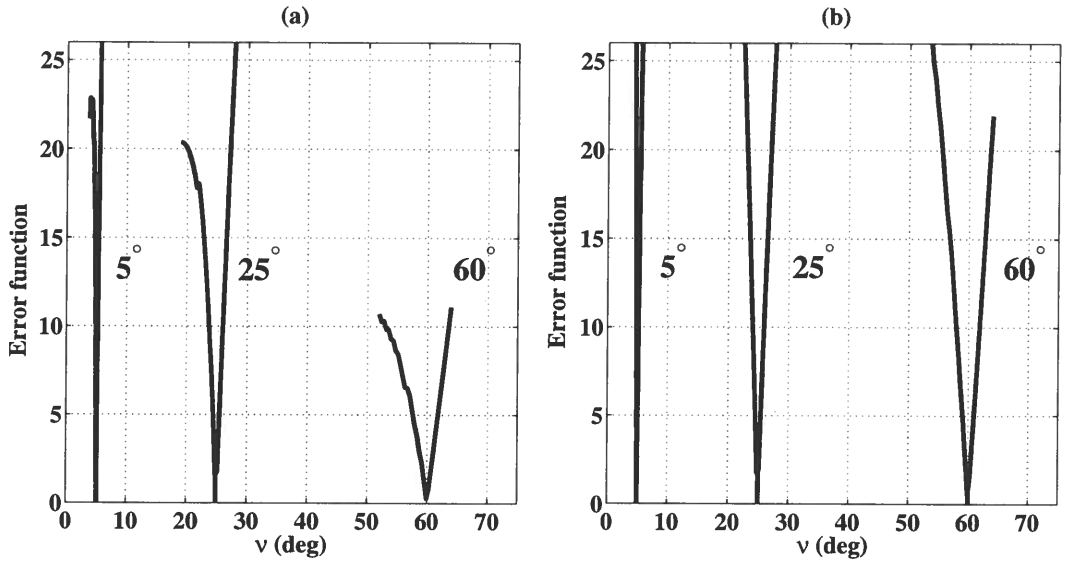

Figure 4.5. Square-root of the misfit function (4.17) for (a) the time asymmetry factor Δt_{PS}; and (b) the offset asymmetry factor Δx_{PS}. The misfit function is computed for the models in Figure 4.4 which fit the pure-mode data and satisfy the constraint $0 \leq \epsilon \leq 1$.

4.2.3 Numerical examples

To evaluate the stability of the parameter estimation, I present a series of numerical tests in which the input data were computed from the exact equations and contaminated by Gaussian noise. For each model, the parameter vector $\boldsymbol{m}$ [equation (4.12)] is obtained for 200 realizations of the input data using the inversion algorithm described above.

In the previous section, I showed that the leading terms in the offset x_{SS} in the equations for the asymmetry attributes do not provide independent information for the parameter estimation. Therefore, to assess the accuracy of the inversion, it is convenient to define the *quality factor* for the time asymmetry Δt_{PS} as

$$Q \equiv \max \left\{ \frac{|\Delta t_{PS}^{\text{lin}} - \Delta t_{PS}^{\text{exact}}|}{|\Delta t_{PS}^{\text{lin}}|} \right\}, \tag{4.18}$$

where $\Delta t_{PS}^{\text{exact}}$ is the exact value and $\Delta t_{PS}^{\text{lin}}$ is the linear term in x_{SS} [equation (4.3)]; Q is computed for the maximum PS-wave offset-to-depth ratio equal to two. Since the sensitivity of the offset asymmetry factor to the model parameters is similar to that for the time asymmetry (see Figure 4.5), I do not include Δx_{PS} in equation (4.18). If the quality factor is large (close to or greater than unity, according to my estimates), nonlinear terms in Δt_{PS} are substantial and the asymmetry attributes typically provide significant independent information for the inversion.

First, I consider TTI media with large tilts of the symmetry axis ($\nu > 40°$), which

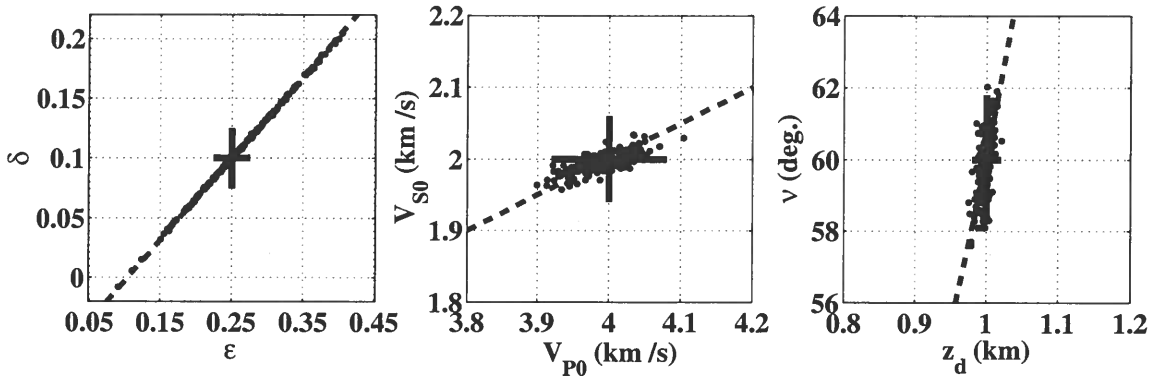

Figure 4.6. Inverted parameters (dots) of a dipping TTI layer with $\nu = 60°$ obtained from 2D PP and PS data in the symmetry-axis plane. The correct model parameters are marked by the crosses. The dashed lines on the $[\epsilon, \delta]$, $[V_{P0}, V_{S0}]$, and $[\nu, z_d]$ plots correspond to the correct values of χ, V_{P0}/V_{S0}, and $\sin\nu/z_d$, respectively. The input data were contaminated by Gaussian noise with standard deviation of 2% for the NMO velocities, 0.5% for the zero-offset traveltimes, 1% for the time slopes, and 2% for the PS-wave asymmetry attributes.

also implies steep reflectors. Such models are typical for the Rocky Mountain Foothills in Western Canada and other fold-and-thrust belts that contain steeply dipping TI shale layers (e.g., Isaac & Lawton, 1999). The inversion for $\nu = 60°$ produces unbiased results, with the mean of each model parameter close to the correct value (Figure 4.6). Whereas the quality factor for the model in Figure 4.6 is smaller than unity ($Q = 0.6$), the moveout asymmetry is quite pronounced, with the maximum of Δt_{PS} reaching 20% of the zero-offset PS traveltime, and the maximum of Δx_{PS} at far offsets reaching 70% of z_d. In comparison, for the reference isotropic medium with $\epsilon = \delta = 0$, the quality factor is infinite, the maximum of Δt_{PS} is also 20% of the zero-offset time, and Δx_{PS} is up to 110% of z_d. Since the magnitude of the asymmetry attributes is relatively large, it should be possible to estimate both Δt_{PS} and Δx_{PS} with high accuracy.

If I assume that the error in the asymmetry attributes is 2%, the parameters V_{P0}, V_{S0}, and z_d are well constrained (the standard deviation is less than 1%), and the standard deviation in ν is only 1° (Figure 4.6). In agreement with the relatively small value of the quality factor, however, the inverted anisotropic parameters ϵ and δ exhibit more scatter, with the standard deviation reaching 0.06 and 0.04, respectively. Also, the estimates of ϵ and δ degrade rapidly as the error in the asymmetry attributes increases, while the deviations in V_{P0}, V_{S0}, and z_d remain small. It is clear from Figure 4.6 that the best-constrained parameter combinations are $\chi \equiv (\sigma - \delta)/(1 + 2\sigma)$, $\sin\nu/z_d$, and V_{P0}/V_{S0}. In principle, ϵ and δ for large tilts can be obtained with sufficient accuracy from wide-azimuth PP and SS data, as demonstrated by Grechka et al. (2002a).

If the tilt for the model from Figure 4.6 is reduced from 60° to 25° (Figure 4.7), the quality factor Q increases to 1.1, which indicates that for the same errors in the input

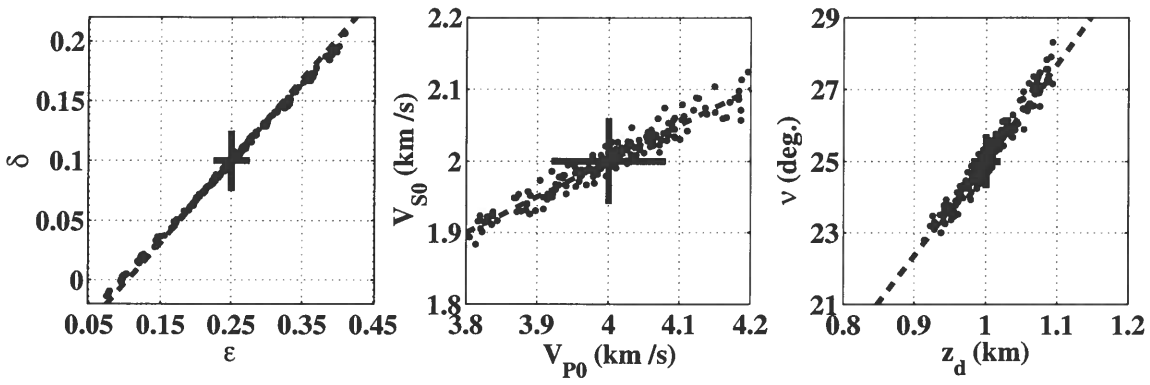

Figure 4.7. Inversion results for a model with same parameters as those in Figure 4.6 except for tilt $\nu = 25°$. The standard deviations in the asymmetry attributes are increased to 6%; the deviations in the NMO velocities (2%), zero-offset traveltimes (0.5%), and time slopes (1%) remain the same.

data the inversion should become more stable (i.e., the model parameters should be better resolved). The magnitude of Δt_{PS} for $\nu = 25°$, however, decreases to just 8% of zero-offset time (the corresponding value for the reference isotropic medium is 14%). Therefore, I expect the uncertainty in the Δt_{PS} and Δx_{PS} to become larger for mild tilts.

If the error in the asymmetry attributes is set to 6%, the standard deviation of the tilt ν is almost the same (1°) as that in Figure 4.6. Despite the high resolution in ν, Figure 4.7 shows that the standard deviations in V_{P0}, V_{S0}, and z_d increase to about 4%; the deviations in ϵ and δ are also substantial (0.08 and 0.05, respectively). Although the accuracy in all model parameters becomes acceptable if the error in the asymmetry attributes is limited to 2%, the small magnitude of Δt_{PS} and Δx_{PS} makes such low error levels unrealistic.

An interesting special case is that of an elliptically anisotropic medium ($\epsilon = \delta$). For the same tilt $\nu = 25°$ as that in Figure 4.7, but with $\epsilon = \delta = 0.2$, the quality factor $Q = 2.1$, which indicates added significance for the higher-order terms in offset in the equations for Δt_{PS} and Δx_{PS}. The magnitude of the time asymmetry factor is also substantial (about 20% of zero-offset time), so the inversion should be stable. It turns out, however, that the parameter estimation is feasible only if the elliptical condition is assumed in advance (i.e., the inversion is performed with $\epsilon = \delta$). If the inversion is carried out without any assumption about ϵ and δ, then the inversion for several model parameters is unstable, even though the tilt is well-constrained.

To understand the influence of the asymmetry error on the inverted parameters, I repeated the inversion for a wide range of the standard deviations in Δt_{PS} and Δx_{PS} (Figures 4.8 and 4.9). Figure 4.8 shows that for the same size errors in the input data, the velocity V_{P0} becomes better constrained for models with larger tilt, whereas for ν the opposite is true. The results for V_{P0} are explained by the much lower sensitivity of this parameter to distortions in tilt for models with large values of ν (Figure 4.4b). The standard

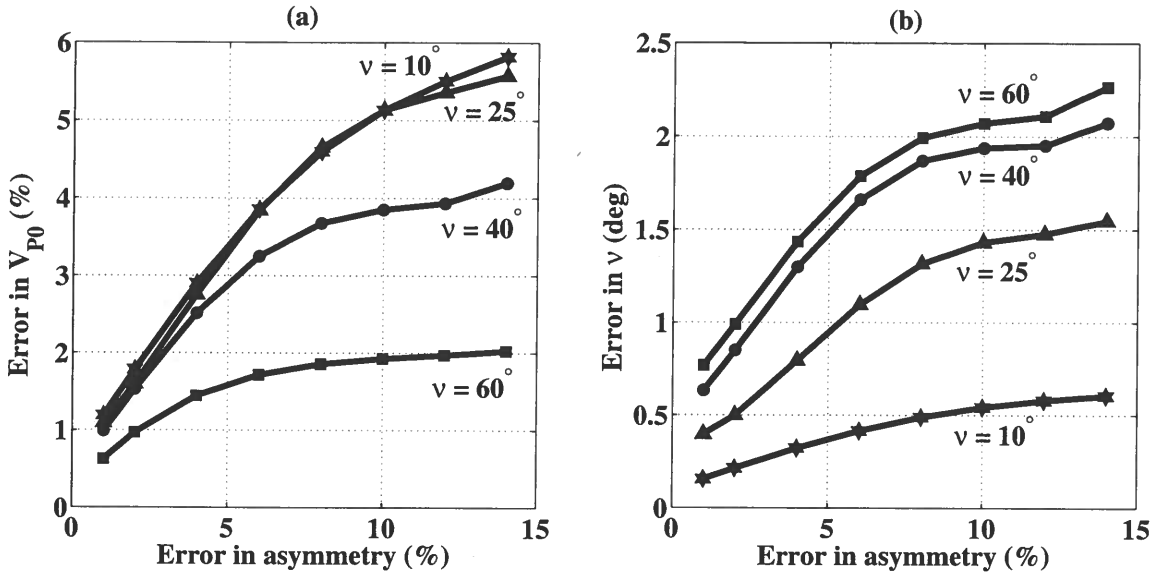

Figure 4.8. Error (the standard deviation) in the velocity (a) V_{P0} and (b) the tilt ν as a function of the standard deviation in the asymmetry attributes. The tilts are 10° (the line with stars), 25° (triangles), 40° (circles), and 60° (squares). The parameters V_{P0}, V_{S0}, ϵ, δ, and z_d and the standard deviations in the NMO velocities, zero-offset times, and time slopes are the same as those in Figure 4.6.

deviations in the shear-wave velocity V_{S0} and the distance z_d are close to those for V_{P0}.

Overall, the tilt remains well resolved for models with $\nu > 10°$ and errors in the asymmetry attributes of up to at least 15% (Figure 4.8b). The accuracy in the parameters V_{P0}, V_{S0}, and z_d, however, is acceptable only for large tilts, over 40° (Figure 4.8a). For moderate values of ν, between 25° and 40°, V_{P0}, V_{S0}, and z_d can be constrained using good-quality converted-wave data that produce small errors in the asymmetry attributes. If the tilt is smaller than 25°, the moveout asymmetry is weak, and the large uncertainty in Δt_{PS} and Δx_{PS} should make the estimates of V_{P0}, V_{S0}, and z_d highly inaccurate.

The standard deviations in the parameters ϵ and δ (Figure 4.9) show a pattern similar to that for the tilt (Figure 4.8b). For the same level of the asymmetry errors, both ϵ and δ are better resolved for smaller values of ν. The error curves in Figures 4.9a and 4.9b have almost the same shape for all ν because the parameter χ, which is well-constrained by the data, is close to a linear combination of ϵ and δ. Since, however, ϵ does not directly contribute to the vector of input data, its standard deviation is about 50% larger (on average) than the deviation in δ. Given the higher asymmetry errors for smaller tilts, the errors in ϵ and δ are expected to be somewhat constant for a wide range of moderate and large tilts and rapidly increase for quasi-VTI models with small values of ν.

If wide-azimuth PP and PS data are available, a similar inversion algorithm can be designed by combining the NMO ellipses, zero-offset traveltimes, and time slopes of the

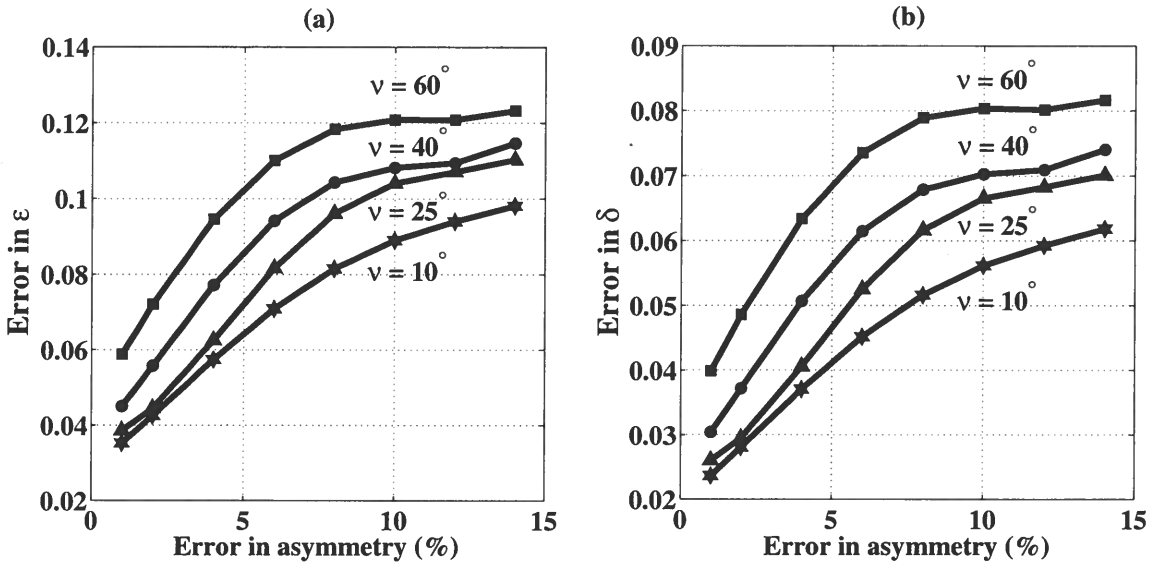

Figure 4.9. Same as Figure 4.8, but for the parameters (a) ϵ and (b) δ.

pure modes with the 3D asymmetry attributes of the PSV-wave. Linearization of equations (F.26) and (G.8) for small tilts ν shows, however, that the azimuthal variation of the asymmetry attributes can be predicted from their dip components ($\alpha = 0$):

$$\Delta t_{PS}(\alpha) = \Delta t_{PS}(0)\,\cos\alpha\,, \tag{4.19}$$

$$\Delta x_{PS}(\alpha) = \Delta x_{PS}(0)\,\cos\alpha\,. \tag{4.20}$$

Hence, the magnitude of the asymmetry attributes decreases away from the dip direction and goes to zero in the $[x_2, x_3]$-plane. The weakened moveout asymmetry for azimuths away from the dip direction means that including the azimuthal variation of Δt_{PS} and Δx_{PS} can increase the signal-to-noise ratio only marginally. An alternative or complementary option for enhancing the signal is to stack the dip components of the asymmetry attributes for adjacent CMP locations under the assumption of weak lateral heterogeneity.

For large tilts ($\nu > 40°$), the azimuthal variation of the moveout attributes becomes more complicated and cannot be described by equations (4.19) and (4.20). Numerical testing indicates that if $\nu > 40°$, the factors $\Delta t_{PS}(\alpha)$ and $\Delta x_{PS}(\alpha)$ measured in wide-azimuth surveys provide useful constraints on the model parameters. The asymmetry attributes, however, are redundant for large tilts because the inversion can be carried out using wide-azimuth PP and SS data alone (Grechka et al., 2002a).

4.3 Summary

The modified PP+PS=SS method introduced in Chapter 3 is applied here to the inversion of multicomponent (PP and PS) data acquired over a dipping TTI layer with the symmetry axis orthogonal to the layer's bottom. As in Chapter 3, the moveout asymmetry attributes of the PSV-wave play a crucial role in the parameter-estimation procedure.

To analyze the moveout asymmetry in the vertical plane that contains the symmetry axis (the symmetry-axis plane), I developed the weak-anisotropy, small-offset approximation for the time (Δt_{PS}) and offset (Δx_{PS}) asymmetry factors. Although the anisotropy has a strong influence on both Δt_{PS} and Δx_{PS} even at small offsets, the leading terms in offset depend just on the moveout parameters of the pure (PP and SS) reflection modes. Therefore, independent information for the inversion procedure is contained only in the higher-order terms, which become significant when the offset-to-depth ratio for the PS-waves approaches two.

The stability of the inversion for a given TTI model was predicted using the quality factor (Q) which quantifies the relative magnitude of the cubic and higher-order terms in offset for the time asymmetry Δt_{PS}. Relatively small values of Q ($Q < 1$), resulting in part from a limited offset range of the acquired PP and PS data, typically indicate that the estimated parameters are highly sensitive to noise.

Application of the algorithm to noise-contaminated input data shows that the tilt ν of the symmetry axis is well resolved even when the model approaches VTI ($\nu = 0°$). The accuracy in the symmetry-direction velocities V_{P0} and V_{S0} and the distance z_d from the CMP to the reflector may be sufficient only if the symmetry axis deviates by at least 25° from the vertical. For moderate tilts $25° < \nu < 40°$, however, the inversion for V_{P0}, V_{S0}, and z_d is possible only if the errors in the asymmetry attributes are relatively small. The resolution in the anisotropic parameters ϵ and δ is flat over a wide range of moderate and large tilts, with δ constrained much tighter than is ϵ. For quasi-VTI models with $\nu < 15 - 20°$, the magnitude of the asymmetry attributes is insufficient for reliable estimation of all model parameters, except for the tilt itself.

On the whole, the 2D inversion in the symmetry-axis plane gives acceptable results if the tilt exceeds 40° and, for high-quality input PS data, for the range of moderate tilts $25° < \nu < 40°$. Still, the accuracy of the inverted parameter ϵ is marginal even for large values of ν (i.e., for large dips). Note that the inversion for $\nu > 40°$ can be accomplished even without the asymmetry information, but it requires wide-azimuth PP and PS (or PP and SS) data (Grechka et al., 2002a). The addition of wide-azimuth data (including the asymmetry attributes), however, does not help in the parameter estimation for moderate tilts.

This chapter is submitted for publication in Geophysics (Dewangan & Tsvankin, 2004b).

Chapter 5

Physical modeling

In this chapter, I demonstrate on a physical model that PP and PS data constrain all the model parameters in a horizontal TTI layer. Multicomponent, multioffset 2D seismic lines are acquired in the symmetry-axis plane. As discussed in Chapter 3, converted-wave moveout in this model becomes asymmetric and provides valuable information about the medium parameters. PP and PS data are processed using the modified PP+PS=SS method to obtain pure SS-wave reflection traveltime as well as the asymmetry attributes (see Chapter 3). The time and offset asymmetry attributes are then combined with the pure-mode (P and S) NMO velocities and zero-offset traveltime to estimate the model parameters. The estimated model makes it possible to accurately reproduce the results of a transmission experiment.

5.1 Physical Model

The material used to simulate the TTI medium is XX-paper-based phenolic composed of thin layers of paper bonded with phenolic resin. These layers of paper are analogous to thin layering, producing an effective VTI medium. In the geophysical literature such phenolic materials are reported to be anisotropic (Isaac & Lawton, 1999; Grechka et al., 1999b). The sample was prepared by cutting a large chunk of commercially available phenolic into smaller blocks and pasting them together at an angle to form a TTI medium. To simulate steeply dipping fractures (see Chapter 3), the tilt of the symmetry axis is chosen to be 70° from the vertical. The length, width, and thickness of the sample are 60 cm, 30.5 cm, and 10.8 cm, respectively (Figure 5.1).

The reflection and transmission surveys were acquired in the Institute for Experimental Geophysics (IEG) at Colorado School of Mines (CSM). I collected one set of measurements (2D seismic lines) using source and receiver transducers (flat-faced cylindrical piezoelectric ultrasonic contact transducers). The P- and S-waves are excited by transducers polarized in the vertical and horizontal directions, respectively. The same type of transducer was used as both source and receiver. Shot gathers were collected by fixing the shot transducer and manually moving the receiver transducer along a prescribed line. The waveforms were measured using TDS 420A digitizing oscilloscope and recorded by Wavestar software.

Another set of independent measurements was collected using a transducer as a source and a laser vibrometer as a detector. The wavefield is detected by a scanning laser vibrometer that measures the absolute particle velocity on the surface of the sample via the Doppler shift. The output of the vibrometer-head is a beam of diameter less than 1 mm and

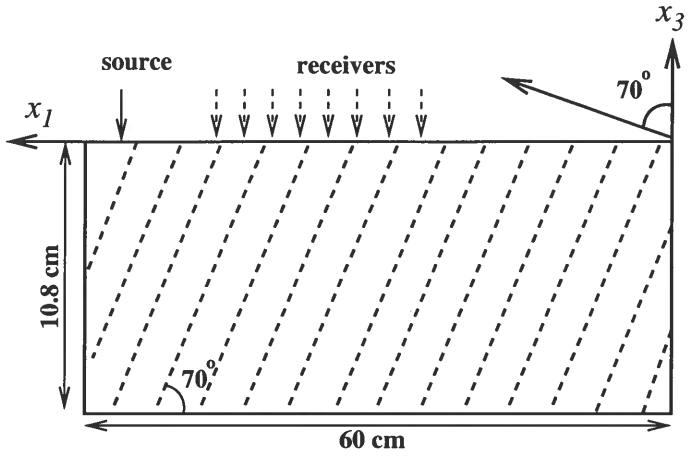

Figure 5.1. Physical model representing a single TTI layer. The coordinate system is chosen in such a way that the symmetry axis is confined to the $[x_1, x_3]$-plane and is dipping in the negative x_1-direction.

a wavelength of 633 nm (red). Once the beam reflects off a moving target, its frequency is Doppler shifted. The beat-frequency of the output and the reflected signal are decoded in the hardware to give an absolute measurement of particle velocity, without contacting the medium. The signal of the vibrometer is amplified with a low-noise preamplifier (SR 560 with 6 db/octave 100 Hz - 1MHz band-pass filter) and digitized at 14-bit resolution using a Gage digital oscilloscope card, attached to a PC. To ensure a high signal-to-noise ratio, a reflective tape is applied to the model to ensure strong reflectivity of the interferometer beam. The stacking (averaging) of multiple shots improves data quality. The scanning head is programmed to move the beam after each measurement, so that dense arrays of data can be recorded automatically. This stands in sharp contrast with time-consuming contact transducer measurements, where relatively large receivers have to be moved manually.

5.2 Seismic reflection experiment

To investigate the moveout asymmetry of PS-wave and test the parameter-estimation algorithm (Chapter 3), I conducted a multichannel, multioffset seismic reflection experiment over a TTI layer. The inversion algorithm requires CMP gathers of PP and PS data with the maximum offset-to-depth ratio no smaller than two. Since the acquisition of a CMP gather involves moving both the source and receiver transducers, it is cumbersome and prone to error in positioning. Therefore, I decided to collect a shot gather (Figure 5.1) and interpret it as a CMP gather. If the medium is laterally homogeneous, a shot gather is equivalent to a CMP gather. This assumption was verified by collecting a constant-offset P-wave section (Figure 5.2). The first arrival (the direct P-wave) and the P-wave multiple around 0.18 ms are clearly reproducible in the lateral direction. The P-wave primary around 0.07 ms shows some lateral variation in the waveform due to its interference with the ground roll. The

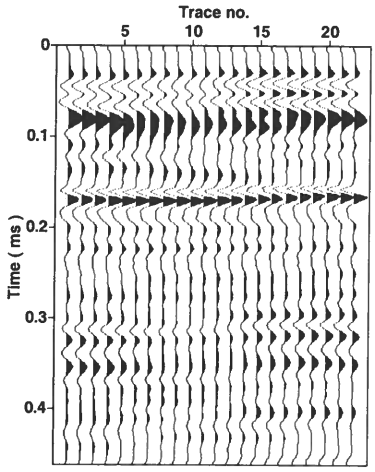

Figure 5.2. Constant-offset reflection P-wave section acquired to validate the assumption of lateral homogeneity.

minor differences in the waveforms might also be related to error in receiver positioning and scattering from air bubbles between imperfectly glued blocks.

I collected PP and PS shot gathers by fixing the P-wave shot transducer at one end of the model and manually placing the P- and S-wave receiver transducer at a constant interval of 1 cm in the symmetry-axis plane (Figure 5.1). The maximum offset-to-depth ratio is 2.8. The whole procedure was repeated by placing the source transducer at the other end of the model to record negative offsets. The traces for positive and negative offsets are than combined to form a split-spread CMP gather. Another independent dataset was obtained by repeating the experiment with detection by the laser vibrometer and a sampling interval of 2 mm. The maximum offset-to-depth ratio for this dataset is 2.5.

5.2.1 Vertical component of the multichannel survey

For the vertical component recorded with the contact transducer (Figure 5.3a), the source-receiver offset ranged from 3 to 30 cm; the offset could not be smaller than 3 cm because of the finite size of the transducers. For the densely spaced data recorded with the laser vibrometer (Figure 5.3b), the source-receiver offset ranged from 2 to 27 cm. Since the laser measures the vertical velocity at a point, it is possible to record close to the source but the signal quality deteriorates at far offsets.

These two datasets have large similarity, with the same major events clearly identified on both gathers. Since the reflections are masked by the ground roll, I decided to suppress it by applying an F-K dip filter (Figure 5.4). The first arrival is the direct P-wave traveling with the horizontal velocity of 2620 m/s. The strong ground roll (Figures 5.3a,b) travels with the velocity of 1285 m/s, slightly smaller than the shear-wave velocity along the symmetry

axis. The P-wave primary from the bottom of the block and first multiple reflection can be identified around 0.064 ms and 0.128 ms, respectively. Since the laser dataset is densely sampled and has better coherency, I used it for manually picking the traveltimes.

The dominant frequency decreases from 200 kHz at near offsets to around 40 kHz at far offsets showing that the medium is strongly attenuative (Figure 5.5). If we assume a dominant frequency of 100 kHz, then all the units of time and distance should be scaled by 5000 from the model size to values corresponding to seismic field data. The scaled seismic data will have a central frequency of 20 Hz and the equivalent thickness of the physical model will be 540 m.

The P-wave normal moveout (NMO) velocity is estimated using conventional hyperbolic velocity analysis (Figure 5.6). To minimize the influence of nonhyperbolic moveout, velocity analysis was performed for maximum offset-to-depth ratio close to one. The NMO velocity for both the primary and multiple P-waves, which flattens the near-offset gather (Figure 5.6b), is 2350±50 m/s. At large offsets, the gather is not flat due to the influence of nonhyperbolic moveout. This deviation from hyperbolic moveout indicates that the medium is anisotropic because the reflection moveout in a single homogeneous isotropic layer is always hyperbolic. An event around $t_0 = 0.11$ ms, which has a lower moveout velocity than the P-wave NMO velocity, may be interpreted as a converted wave, but it is not prominent on the vertical component. In order to clearly identify PS-waves, I recorded the horizontal component, as discussed in the next section.

5.2.2 Horizontal component of the multichannel survey

I used the same reflection settings to record both the horizontal and vertical components. While the source was a P-wave transducer, S-wave transducer was used as the receiver. The receiver transducer was oriented horizontally in the symmetry-axis plane to record SV-waves. Once again, the source-receiver offset ranged from 3 to 30 cm, with an increment of 1 cm. I recorded a shot gather and interpreted it as a CMP gather. The raw horizontal component of the wavefield in the $[x_1, x_3]$-plane is shown in Figure 5.7a. The energy on the crossline component (not shown here) is almost zero, indicating that the data are indeed acquired in a symmetry plane of the medium. Also, the shear-wave splitting along the symmetry axis is negligible, suggesting that the medium is either TI or a special case of orthorhombic media with equal coefficients $\gamma^{(1)}$ and $\gamma^{(2)}$ (Tsvankin, 1997). For either case, the parameter-estimation algorithm proposed in Chapter 3 should be valid.

Although the laser vibrometer system available at CSM can be used to record the horizontal component, so far it has been tested to record only the vertical component. Hence, the current setup could not be used to record the converted PS-waves, but this limitation can be overcome by recording the SP-waves and treating them as PS-waves. Instead of using P-wave transducers, a shear transducer was used as the source and a laser vibrometer as the detector. According to the reciprocity theorem, the SP-wave is kinematically identical to the PS-wave, but with the opposite sign of the offset vector. For further analysis, I will treat the SP-wave as the PS-wave by properly correcting the sign of the offset vector.

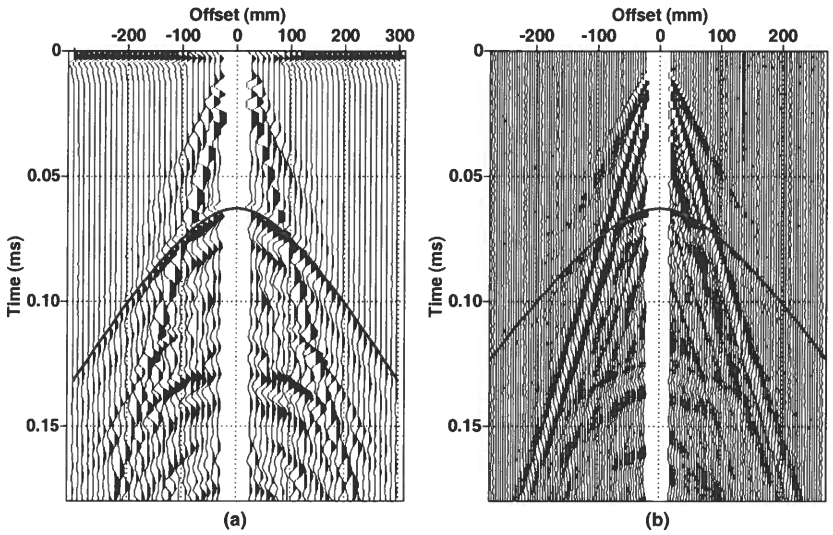

Figure 5.3. Vertical component of the wavefield: (a) Data recoded with the P-wave contact transducers; (b) densely sampled data recorded with the laser vibrometer. The first arrival is the direct P-wave, while the P-wave reflection from the bottom of the block arrives at 0.064 ms (zero-offset time). The solid line is the P-wave primary reflection traveltime picked from the laser dataset.

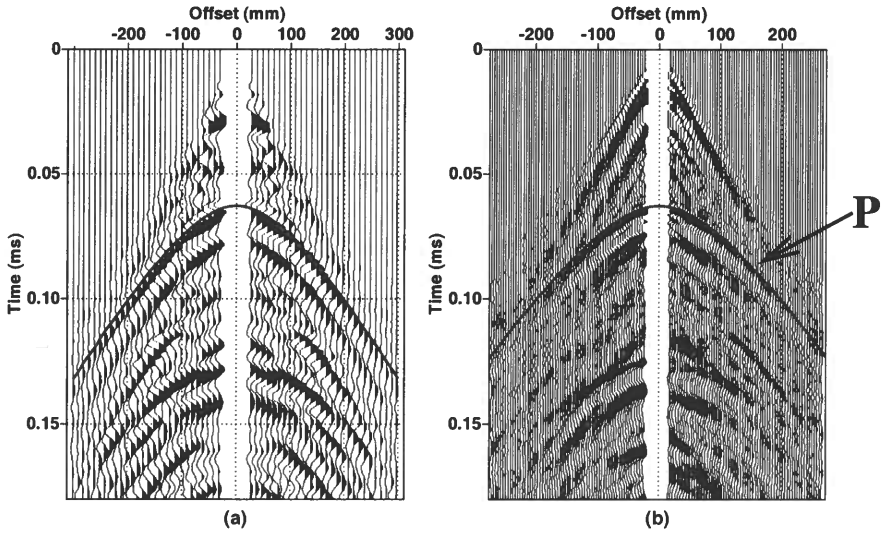

Figure 5.4. Data from Figure 5.3 after application of an FK filter to suppress the ground roll. The P-wave reflection can be more clearly identified at 0.064 ms.

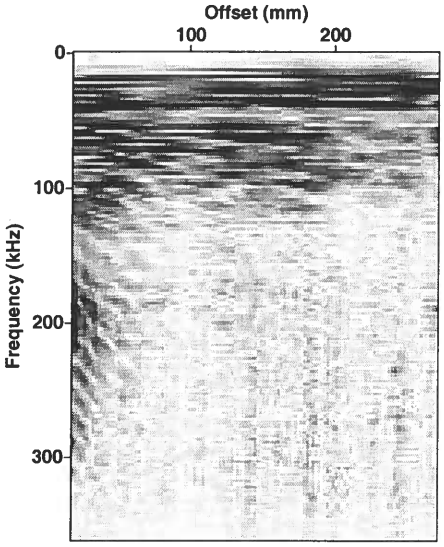

Figure 5.5. Amplitude spectra of the P-wave data showing a decrease in frequency with offset.

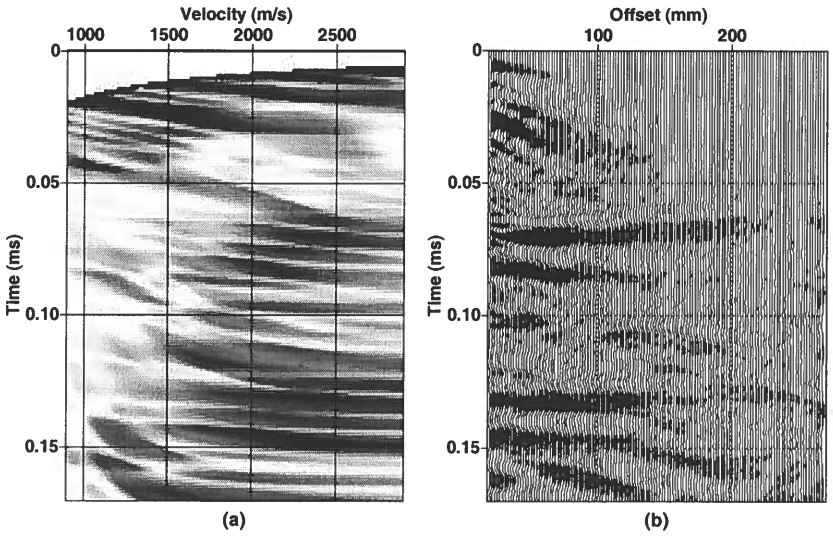

Figure 5.6. Conventional hyperbolic velocity analysis of the P-wave data for the maximum offset-to-depth ratio close to one: (a) Semblance panel; (b) the NMO-corrected gather with a moveout velocity of 2350 m/s.

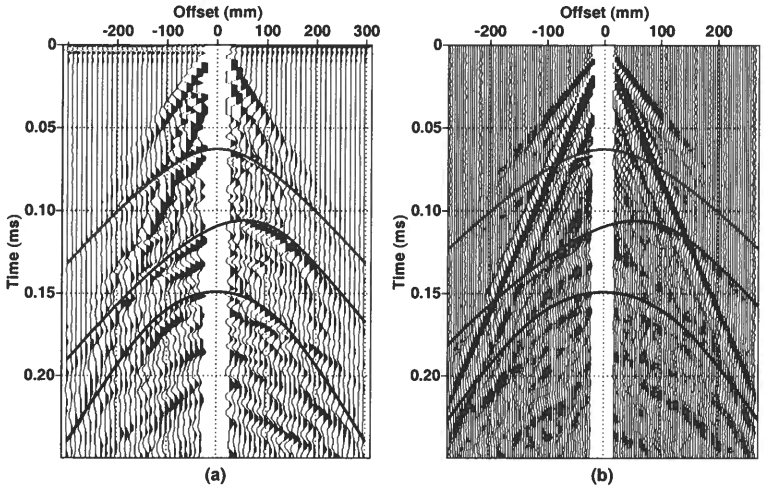

Figure 5.7. Horizontal component of the wavefield: (a) Data recoded with the P-wave source and S-wave receiver transducer; (b) data recorded with the S-wave source and the laser vibrometer as the receiver. The converted wave from the bottom of the model arrives at 0.11 ms and has asymmetric moveout. The solid lines are the picked traveltimes of P-, PSV- and SV-waves arrivals.

Figure 5.7b shows the densely sampled dataset recorded with the laser vibrometer. Since most of the reflections are masked by the ground roll, I suppress that noise by applying FK filtering (Figure 5.8). As before, a close similarity exists between the two datasets recorded with the two different experimental setups. The PSV-wave can be identified at a zero-offset traveltime of 0.11 ms. As expected, it has asymmetric moveout since the traveltime does not remain the same when the source and receiver are interchanged. This asymmetry indicates that the model indeed lacks a horizontal symmetry plane, as should be the case for TTI media. The offset corresponding to the minimum traveltime is shifted from $x = 0$ by 6 cm in the positive direction of the x_1-axis. The converted wave reverses its polarity at an offset close to the minimum traveltime.

The PS-wave traveltime picks were made using the laser dataset (the solid line in Figure 5.8). I intentionally reverse the polarity at negative offsets to facilitate correlation of PS traveltimes. Even on the horizontal component, the P-wave primary reflection can still be identified around the zero-offset time $t_0 = 0.064$ ms. The solid line with apex at 0.064 ms, which marks the picked P-wave traveltime from the vertical component, matches P-wave arrival on the horizontal component. It may also be possible to interpret the SS-wave primary reflection but it is not as prominent as the other modes because the P-wave transducer does not excite enough S-wave energy.

As described in Chapter 3, I used the modified PP+PS=SS method to obtain the kinematics of the pure SS (SVSV) reflections from PP and PS data. The reflection time of

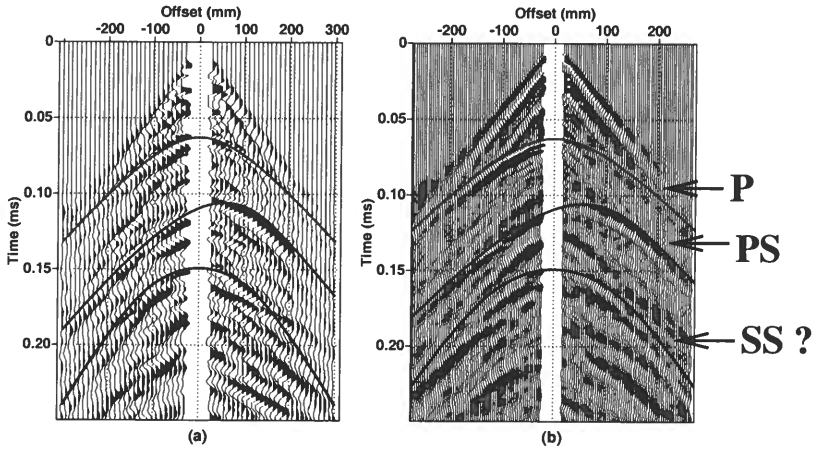

Figure 5.8. To suppress the ground roll, FK filtering is applied to the section from Figure 5.7. The P and PS-wave reflections can be clearly identified at 0.064 ms and 0.11 ms respectively. The negative offset is shown in reverse polarity to facilitate picking of PS-wave traveltime.

both PP (the vertical component) and PS (the horizontal component) data were manually picked from the laser vibrometer dataset. In order to interpolate the traveltimes at near offset and smooth the data, I fitted a polynomial to both PP and PS moveouts using the least-squares method. For this purpose, a 6th-order polynomial gave a sufficiently smooth representation of the traveltime curve. Next, for all desired SS-wave shot-receiver pairs $(x^{(3)}, x^{(4)})$, I constructed the pseudo-shear time function according to equation (3.1):

$$\tau_{SS}(x^{(3)}, x^{(4)}) = \min_{x^{(1)},\, x^{(2)}} \left(t_{PS}(x^{(1)}, x^{(3)}) + t_{PS}(x^{(2)}, x^{(4)}) - t_{PP}(x^{(1)}, x^{(2)}) \right). \quad (5.1)$$

The minimum of the pseudo-shear function in both the $x^{(1)}$ and $x^{(2)}$ directions yields the stationary points. Substituting the traveltimes corresponding to the stationary points into equation (5.1) gives the SS-wave traveltime for that particular offset. By repeating this procedure for different source-receiver pairs, I compute the SS-wave traveltime as a function of the SS-wave offset (Figure 5.9).

Conventional hyperbolic velocity analysis applied to the constructed SS arrivals was used to estimate the stacking velocity ($V_{\text{nmo,S}} \approx 1780$ m/s) and zero-offset traveltime ($t_{S0} \approx 0.149$ ms). Next, I compute the time and offset asymmetry attributes introduced in Chapter 3,

$$\begin{aligned} \Delta t_{PS}(x^{(3)}, x^{(4)}) &= t_{PS}(x^{(1)}, x^{(3)}) - t_{PS}(x^{(2)}, x^{(4)}), \\ \Delta x_{PS}(x^{(3)}, x^{(4)}) &= x_{PS}(x^{(1)}, x^{(3)}) - x_{PS}(x^{(2)}, x^{(4)}). \end{aligned} \quad (5.2)$$

The traveltime asymmetry factor (Δt_{PS}) is normalized with respect to the zero-offset PS-

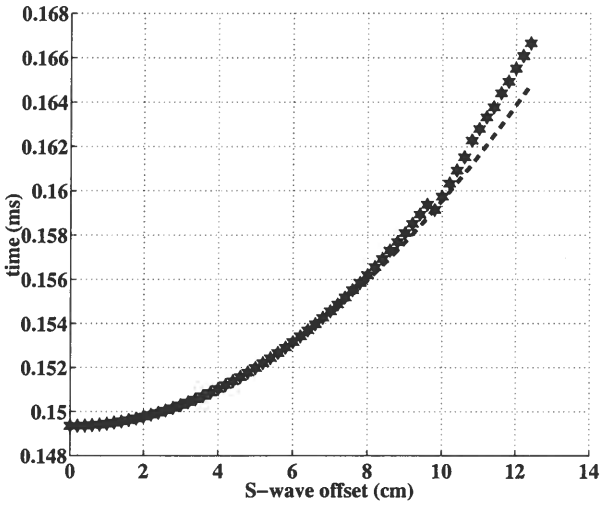

Figure 5.9. The SS-wave traveltime obtained using the PP+PS=SS method (stars) is plotted as a function of the SS-wave offset. The dashed line corresponds to the hyperbolic moveout equation with the NMO velocity equal to 1780 m/s

wave time and expressed as a function of the SS-wave offset (Figure 5.10a). The depth-normalized offset asymmetry, which is significant even at small offsets, is displayed in Figure 5.10b. The offset asymmetry at zero offset is twice the offset corresponding to the minimum traveltime in a PS-wave CMP gather.

5.2.3 Parameter Estimation

The processing of the 2D multicomponent data described above produces the following data vector $\boldsymbol{d}$:

$$\boldsymbol{d} \equiv \left\{ V_{\text{nmo,P}} \, , \, t_{P0} \, , \, V_{\text{nmo,S}} \, , \, t_{S0} \, , \, \Delta t_{PS}(x_{SS}) \, , \, \Delta x_{PS}(x_{SS}) \right\} . \tag{5.3}$$

The analytic expressions needed to model these quantities are discussed in Chapter 3. The model vector $\boldsymbol{m}$ includes the parameters of the TTI layer:

$$\boldsymbol{m} \equiv \left\{ V_{P0} \, , \, V_{S0} \, , \, \epsilon \, , \, \delta \, , \, \nu, \, z \right\} . \tag{5.4}$$

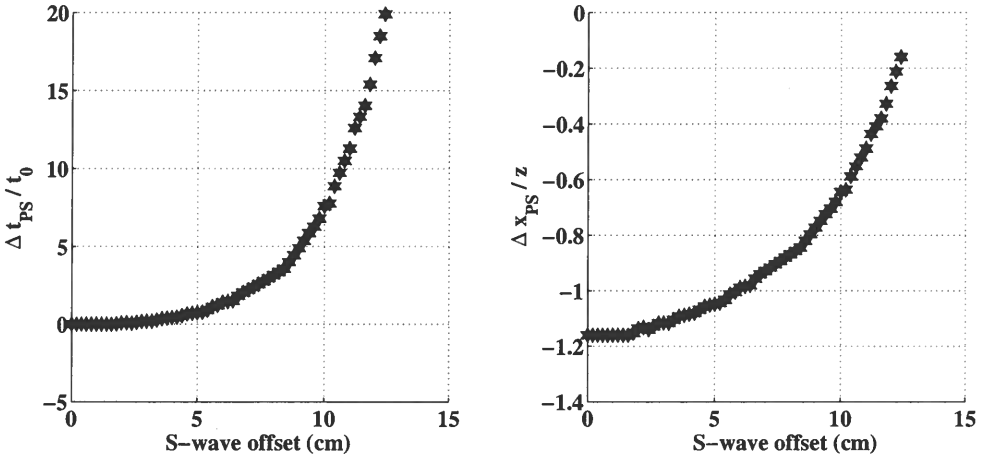

Figure 5.10. Asymmetry attributes obtained from the PP+PS=SS method: (a) The normalized traveltime asymmetry; (b) the corresponding offset asymmetry.

To estimate the vector $\boldsymbol{m}$, I applied the nonlinear inversion algorithm discussed in Chapter 3, with the misfit (objective) function is defined as

$$\begin{aligned}\mathcal{F} \equiv & \frac{(V^{\text{calc}}_{\text{nmo,P}} - V^{\text{meas}}_{\text{nmo,P}})^2}{(V^{\text{meas}}_{\text{nmo,P}})^2} + \frac{(V^{\text{calc}}_{\text{nmo,S}} - V^{\text{meas}}_{\text{nmo,S}})^2}{(V^{\text{meas}}_{\text{nmo,S}})^2} + \frac{(t^{\text{calc}}_{P0} - t^{\text{meas}}_{P0})^2}{(t^{\text{meas}}_{P0})^2} \\ & + \frac{(t^{\text{calc}}_{S0} - t^{\text{meas}}_{S0})^2}{(t^{\text{meas}}_{S0})^2} + \frac{\sum_0^{x^{\max}_{SS}} (\Delta t^{\text{calc}}_{PS} - \Delta t^{\text{meas}}_{PS})^2}{(\sum_0^{x^{\max}_{SS}} \Delta t^{\text{meas}}_{PS})^2} + \frac{\sum_0^{x^{\max}_{SS}} (\Delta x^{\text{calc}}_{PS} - \Delta x^{\text{meas}}_{PS})^2}{(\sum_0^{x^{\max}_{SS}} \Delta x^{\text{meas}}_{PS})^2},\end{aligned} \tag{5.5}$$

where the superscripts "calc" and "meas" denote the calculated and measured quantities, respectively, and $x^{\max}_{SS}$ is the SS-wave offset corresponding to offset-to-depth ratio of PP and PS data close to two. The initial guesses for the vertical velocities and anisotropic coefficients are based on the isotropic relationships,

$$\begin{aligned} V_{P0} &= V_{\text{nmo,P}} = 2.35\,\text{km/s}\,,\ V_{S0} = V_{\text{nmo,S}} = 1.78\,\text{km/s}\,,\ \epsilon = 0,\ \delta = 0, \\ z &= V_{\text{nmo,P}}\, t_{P0}/2 = 7.52\,\text{cm}\,. \end{aligned} \tag{5.6}$$

The initial tilt of the symmetry axis is randomly chosen between 50° and 85°. Although the thickness z was known, it was estimated from the data to simulate a field study. To assess the stability of the inversion, the algorithm was applied to multiple realizations of the input data contaminated by random uncorrelated Gaussian noise with zero mean. The traveltimes were assumed to have been picked with an accuracy of 1/8 of the dominant period. The PP and PS traveltimes were perturbed by the noise, and the inversion was carried out to obtain multiple realizations of the model parameters.

Figure 5.11 shows the inversion results for 200 realizations of the Gaussian noise. The

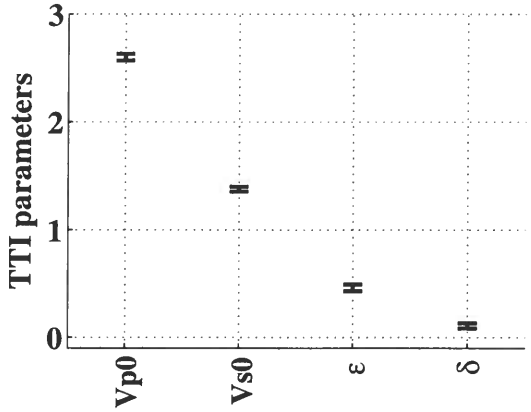

Figure 5.11. Inverted parameters of a horizontal TTI layer obtained from 2D PP and PS data in the symmetry-axis plane. The means of the estimated model parameters are $V_{P0} = 2.6$ km/s, $V_{S0} = 1.38$ km/s, $\epsilon = 0.46$, $\delta = 0.11$, $\nu = 70°$, and $z = 10.9$ cm.

means of the estimated parameters are $V_{P0} = 2.6$ km/s, $V_{S0} = 1.378$ km/s, $\epsilon = 0.46$, $\delta = 0.11$, $\nu = 70°$, and $z = 10.9$ cm with the standard deviations close to 0.03 for ϵ and δ, 2% for V_{P0}, V_{S0}, and z, and 1° for ν. The best-constrained parameter combination is the difference $(\epsilon - \delta)$, which controls both the time- and offset-asymmetry factors (see Chapter 3). For this inversion, which was performed by restricting the offset-to-depth ratio of the PP and PS data to two, the traveltimes computed for the estimated model, are practically indistinguishable from the picked traveltimes at all offsets (Figures 5.4 and 5.8).

5.3 Transmission/calibration experiment

To obtain an independent estimate of the medium parameters, I conducted a transmission experiment. I used the setting of the reflection experiment, but the P-wave source was fixed at the bottom of the model. The laser vibrometer scanned the top of the model at a regular interval of 2 mm. The experiment was set up in such a way that the first-arrival traveltime could be measured for a full range of angles ($0° - 90°$) from the symmetry axis.

The traveltime of the direct P-wave was used to calculate the group velocity expressed in terms of the group angle. The group angle is calculated by assuming a straight ray path between the source and receiver. There is some controversy over which velocity, group or phase, is measured in laboratory experiments employing transducers of finite size (Dellinger & Vernik, 1994). In my experiments, however, the transducer is small (15 mm) compared to the thickness of the model (108 mm), so I assumed that the traveltimes are determined by the corresponding group velocities. The group angle ϕ and the group velocity V_G can

be calculated from the standard TI equations (e.g., Tsvankin, 2001):

$$V_G = V\sqrt{1+\left(\frac{1}{V}\frac{dV}{d\theta}\right)^2}; \qquad (5.7)$$

$$\tan\phi = \frac{\tan\theta + \frac{1}{V}\frac{dV}{d\theta}}{1-\frac{\tan\theta}{V}\frac{dV}{d\theta}},$$

where V and θ are the phase velocity and phase angle.

Figure 5.12 shows the raw transmission data as a function of the receiver coordinate. The zero- and far-offset receiver positions correspond to the directions approximately perpendicular and parallel to the symmetry axis. The first arrival is the direct P-wave followed by the direct S-wave. The solid line marks the P-wave arrival time computed for the inverted TTI model using equation (5.7). The TTI parameters obtained from the reflection experiment accurately predict the P-wave arrival time in the transmission experiment, which suggests that the parameter-estimation procedure is unbiased and stable. Note the presence of a cusp on the group-velocity surface for the direct S-wave arrival. Due to the small S-wave energy generated by the P-wave source, however, the cusp is not prominent.

To clearly identify the cusp, I performed another transmission experiment, this time with the S-wave transducer as the source (Figure 5.13a). The cusp was also reproduced using numerical modeling by the spectral element method (Komatitsch et al., 2000), with the TTI parameters taken from the caption of Figure 5.11. There is excellent similarity between the measured transmitted wavefield (Figure 5.13b) and the one modeled with spectral element method (Figure 5.13a).

The ray-theoretical S-wave traveltimes (solid lines) match the observed S-wave arrivals up to an offset of 100 mm, but they deviate from each other at large offsets. In order to understand this behavior, I applied the spectral element method with a high frequency signal (Figure 5.14). The higher-frequency field exhibits the direct S-wave and the refracted P-wave, whereas, at lower frequency (Figure 5.13a,b), these two arrivals interfere with each other and produce a complex interference pattern. Figure 5.14 also shows the P-wave multiple, which is not clear in the lower-frequency field (Figure 5.13a,b). Note that the extent of the cusp is larger than that predicted by the ray-theory modeling. This is consistent with the observation by Martynov & Mikhailenko (1984) that the S-wave cusp is larger than predicted by ray-theory. The reflection data, however, do not exhibit cuspoidal behavior because the S-wave group angles corresponding to the cusp are not reached in the recorded PS-wavefield.

5.4 Summary

This chapter demonstrates on a physical modeling dataset that PP and PS reflection data are sufficient to recover all parameters of a horizontal TTI layer. The inverted model parameters, obtained from the parameter estimation algorithm introduced in Chapter 3, are validated by comparison with the results of a transmission experiment. The estimated parameters predict both the P- and S-wave direct arrivals in the transmission experiment.

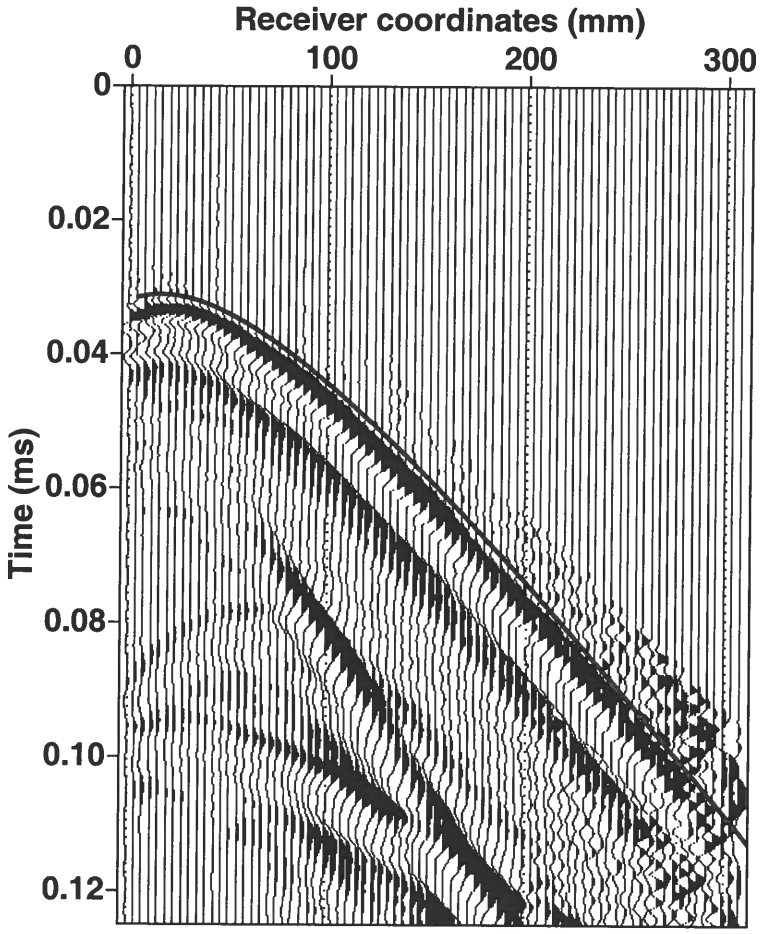

Figure 5.12. Transmitted wavefield recorded by the laser vibrometer at the top of the model. The solid line is the P-wave traveltime modeled using the inverted parameters from Figure 5.11.

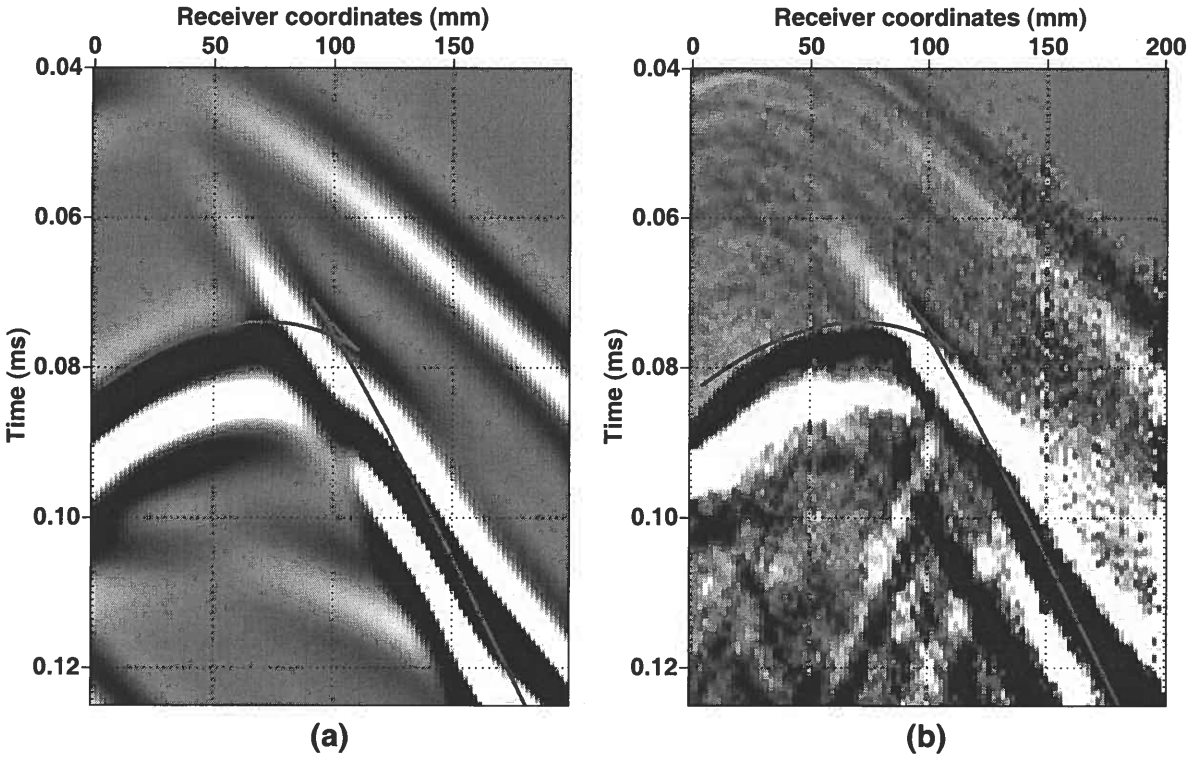

Figure 5.13. S-wave cusp in the transmission experiment: (a) The wavefield simulated with the spectral element method; (b) the wavefield recorded by the laser vibrometer. The solid line is the S-wave time modeled using the inverted parameters from Figure 5.11. The observed cusp is larger than that predicted by the group-velocity surface.

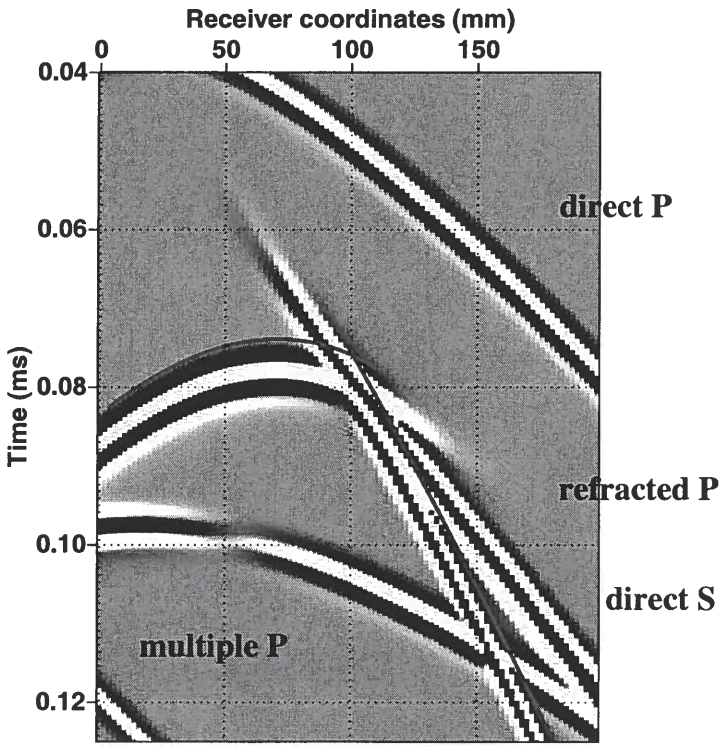

Figure 5.14. Same as Figure 5.13a but the computation was done with a higher frequency wavelet.

Chapter 6

Layer stripping of the asymmetry attributes

In the previous chapters, the model contained a single layer. Here, I show that it is possible to obtain the interval PS-wave asymmetry attributes for multilayered media. The layer-stripping technique is derived and demonstrated, using numerical examples, for a laterally homogeneous medium and for a dipping interface beneath a stack of horizontal layers. The proposed algorithm is exact and can be also used to obtain the interval traveltime for pure modes (PP and SS). The technique also removes the limitation of the general anisotropic Dix equation (Tsvankin, 2001) that includes the interval NMO velocities from non-physical interfaces in the model. This chapter also introduces an approximate expression for the time asymmetry in a heterogeneous, arbitrarily anisotropic media. Additionally, I derive a constraint on the pure mode attributes for a planar reflector under the assumption that the incidence plane coincides with the plane of symmetry.

6.1 Layer stripping in laterally homogeneous media

In a layered medium, the time and offset asymmetry factors obtained from the modified PP+PS=SS method will be effective, as opposed to interval, quantities. The goal here is to obtain the *interval* asymmetry attributes under the assumption that the medium is laterally homogeneous. To facilitate our analysis, the time asymmetry [equation (3.10] of PS-waves is expressed in terms of the horizontal slownesses, which are preserved by Snell's law. Since the traveltimes of the P- and S-legs of both reciprocal PS-waves depends on the same horizontal slownesses ($[p_1, p_2]$) for each layer, the effective time asymmetry attribute for an N^{th} layered medium $[\Delta t_{PS}(N)]$ can be written in the form:

$$\Delta t_{PS}(p_1, p_2, N) = \sum_{i=1}^{N} \Delta t^i_{PS}(p_1, p_2), \tag{6.1}$$

where Δt^i_{PS} is the interval time asymmetry for the i^{th} layer. The time asymmetry in any layer i can be obtained by subtracting the asymmetry attributes from the top $[\Delta t_{PS}(i-1)]$ and bottom $[\Delta t_{PS}(i)]$ of the layer,

$$\Delta t^i_{PS}(p_1, p_2) = \Delta t_{PS}(p_1, p_2, i) - \Delta t_{PS}(p_1, p_2, i-1). \tag{6.2}$$

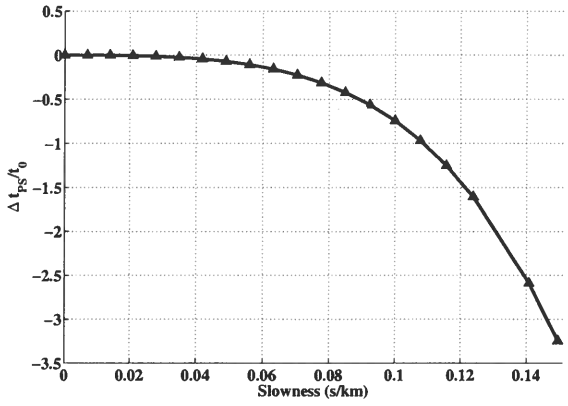

Figure 6.1. Normalized time asymmetry as a function of the horizontal slowness for a three-layer model (solid line) and the single bottom TTI layer (triangles). The first layer is isotropic with $V_P = 2$ km/s, $V_S = 1$ km/s, and $z = 1$ km, the second layer is VTI with $V_{P0} = 4$ km/s, $V_{S0} = 2$ km/s, $\epsilon = 0.15$, $\delta = 0.1$, and $z = 1$ km, and the third (target) layer is TTI with $V_{P0} = 4$ km/s, $V_{S0} = 2$ km/s, $\epsilon = 0.15$, $\delta = -0.15$, $\nu = 70°$, and $z = 1$ km.

The same properties hold for the PS-wave offset asymmetry factor obtained from the modified PP+PS=SS method,

$$\Delta x_{PS}(p_1, p_2, N) = \sum_{i=1}^{N} \Delta x^i_{PS}(p_1, p_2), \tag{6.3}$$

$$\Delta x^i_{PS}(p_1, p_2) = \Delta x_{PS}(p_1, p_2, i) - \Delta x_{PS}(p_1, p_2, i-1). \tag{6.4}$$

Let us consider numerical examples to illustrate this simple layer-stripping technique. To analyze the two-dimensional problem, I assume that the incidence plane coincides with the symmetry plane in each layer. The PP and PS traveltimes are modeled by ray tracing, and the modified PP+PS=SS method is applied to obtain the effective and interval time- and offset-asymmetry attributes (see Chapter 3) in the layered medium.

In first example, the asymmetry is assumed to be generated by anisotropy in the target layer alone. Then the observed asymmetry should be equal to the interval asymmetry of that layer, and no layer-stripping is required. I considered a three-layer model, where the first layer is isotropic, the second layer is VTI, and the third layer is the target TTI horizon. The time asymmetry attribute (Figure 6.1) for the target TTI layer (triangles) is same as that of the three-layer model (solid line).

In the next example, the first layer is VTI, the second layer is TTI with the tilt of the symmetry axis equal to 15°, and the third layer is also TTI but with the tilt equal to 25°. Is inferred from Figure 6.2, the effective asymmetry can be obtained from the interval asymmetry by simply adding the contributions of the individual layers for a fixed ray parameter [equation (6.1)].

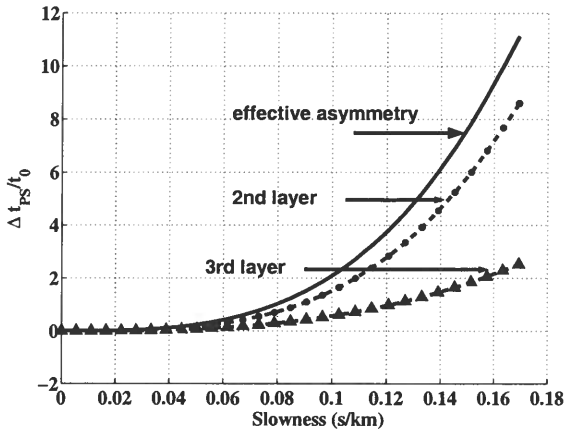

Figure 6.2. Normalized time asymmetry as a function of the horizontal slowness for a three-layer model (solid line), the second layer alone (stars), and the third layer alone (triangles). The first layer is VTI with $V_{P0} = 4$ km/s, $V_{S0} = 2$ km/s, $\epsilon = 0.2$, $\delta = 0.1$, and $z = 0.5$ km, the second layer is TTI with $V_{P0} = 4$ km/s, $V_{S0} = 2$ km/s, $\epsilon = 0.15$, $\delta = -0.1$, $\nu = 15°$, and $z = 0.5$ km, and the third layer is also TTI with the same properties as the second layer but with $\nu = 25°$. The effective asymmetry for any given value of slowness is equal to the sum of the interval asymmetries of the two TTI layers.

6.2 Layer stripping for a dipping reflector

Let us now consider a medium comprised of a stack of horizontal layers above a dipping reflector. The layer immediately above the dipping interface can be heterogeneous and arbitrarily anisotropic but the horizontal layers are assumed to be laterally homogeneous and have a horizontal symmetry plane. Under these assumptions, the converted-wave moveout will be asymmetric for the dipping reflector but not for the reflections in the overburden. The goal of the proposed layer-stripping technique is to obtain the interval traveltime and offset of PP- and PS-waves using the PP+PS=SS method. Once the interval time and offset in the target layer have been computed, the asymmetry attributes can be obtained from the modified PP+PS=SS method as discussed in Chapters 3 and 4.

6.2.1 P-wave layer stripping

Here, I show that the variation of PP+PS=SS method can be used to obtain the interval P-wave traveltime by combining the P-waves from the target reflector and from the interface immediately above it (Figure 6.3). For any output location $[x^{(3)}, x^{(4)}]$, I find $x^{(1)}$ and $x^{(2)}$ by matching the slope of P-wave from the dipping reflector with the slope of P-waves from the overburden. Matching the slopes ensures that the P-wave from the dipping interface and the interface above have the same P-wave leg in the overburden (Figure 6.3).

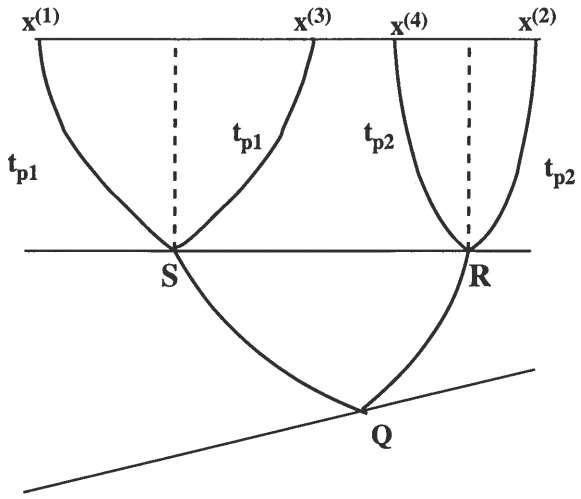

Figure 6.3. Ray diagram of the layer-stripping algorithm (same as Figure 2.1). Instead of operating with PP and PS data from the same interface, the algorithm operates with the P-wave data from the target reflector and the interface immediately above it.

As a result, the interval P-wave traveltime in the target layer can be expressed as

$$t^{i}_{PP}(S,R) = t^{eff}_{PP}(x^{(1)},x^{(2)}) - \frac{1}{2}\left(t^{o}_{PP}(x^{(2)},x^{(4)}) + t^{o}_{PP}(x^{(1)},x^{(3)})\right), \tag{6.5}$$

where the superscripts '*eff*' and '*o*' refer to the effective and overburden P-wave traveltimes. Equation (6.5) is valid only if the upgoing traveltime in the overburden is same as the downgoing traveltime, which requires the assumption that the overburden is laterally homogeneous and has a horizontal symmetry plane. Note that the interval traveltime is obtained for the "shot-receiver" pair $[S,R]$ with the coordinates

$$S = \frac{\left(x^{(1)}+x^{(3)}\right)}{2}\ ,\ R = \frac{\left(x^{(2)}+x^{(4)}\right)}{2} \tag{6.6}$$

on the interface at the top of the dipping layer.

The implementation of this layer-stripping algorithm is similar to the PP+PS=SS method. The P-wave traveltime function (τ_{PP}) for the output location $[x^{(3)},x^{(4)}]$ is found as

$$\tau_{PP}(x^{(3)},x^{(4)}) = t^{o}_{PP}(x^{(1)},x^{(3)}) + t^{o}_{PP}(x^{(2)},x^{(4)}) - t^{eff}_{PP}(x^{(1)},x^{(2)}). \tag{6.7}$$

As discussed in Chapter 3, the minimum of the τ_{PP} function with respect to $x^{(1)}$ and $x^{(2)}$ yields the stationary points. The interval P-wave traveltime can be obtained by substituting the traveltime corresponding to the stationary points into equation (6.5). Similarly, the shot and receiver coordinates can be computed by substituting the stationary points into equation (6.6). By repeating the above procedure for a number of output points $[x^{(3)},x^{(4)}]$,

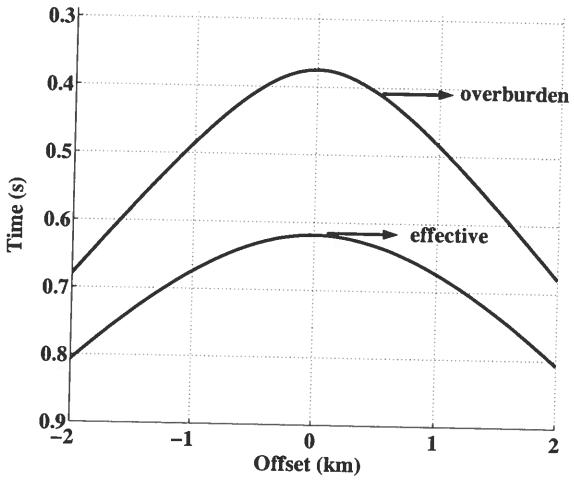

Figure 6.4. CMP gather of the P-wave reflections from the second interface (overburden) and the bottom of a three-layer model with the following parameters: the first layer is VTI with $V_{P0} = 2$ km/s, $V_{S0} = 1$ km/s, $\epsilon = 0.2$, $\delta = 0.1$, and $z = 0.25$ km, the second layer is also VTI with $V_{P0} = 4$ km/s, $V_{S0} = 2$ km/s, $\epsilon = 0.15$, $\delta = 0.05$, and $z = 0.25$ km, and the third layer is dipping TTI with $V_{P0} = 4$ km/s, $V_{S0} = 2$ km/s, $\epsilon = 0.25$, $\delta = -0.05$, $\nu = 25°$, $\phi = 10°$, and $z = 0.5$ km.

one can obtain the interval P-wave traveltime for a range of shot-receiver pairs defined by the stationary points. These shot-receiver pairs may not form a CMP, common-shot, or common-receiver gather and need to be sorted to form the interval traveltime gather in a specified configuration. This is in contrast with the PP+PS=SS method, where the output SS-wave traveltime can be generated in any configuration.

To test this technique, let us consider a three-layer model with the parameters given in the caption of Figure 6.4. The P-wave traveltime from the bottom of the model and the overburden (second interface) are generated by anisotropic ray tracing with a shot spacing of 25 m and a receiver spacing of 100 m. The P-wave traveltime function $[\tau_{PP}(x^{(3)}, x^{(4)})]$ is obtained for a random selection of output locations, and the stationary points are estimated by locating the minimum of the function τ_{PP} in both the $x^{(1)}$ and $x^{(2)}$ directions. The shot-receiver coordinates and the interval P-wave traveltime are found by substituting the stationary points into equations (6.6) and (6.5). For comparison, I compute the exact shot-receiver coordinates and the interval P-wave traveltime for the corresponding stationary points from anisotropic ray tracing in the dipping layer alone. The agreement between my method and the ray-tracing results is excellent (Figures 6.5 and 6.6). The minor differences are related to the interpolation error due to the finite shot and receiver sampling. This layer-stripping technique is exact and works for all offsets. Similar to the PP+PS=SS method, this technique can be extended to 3D, as discussed in Chapter 2.

An interesting application of the proposed algorithm is the extraction of the interval NMO velocity for a dipping layer. As discussed by Tsvankin (2001), the normal-moveout

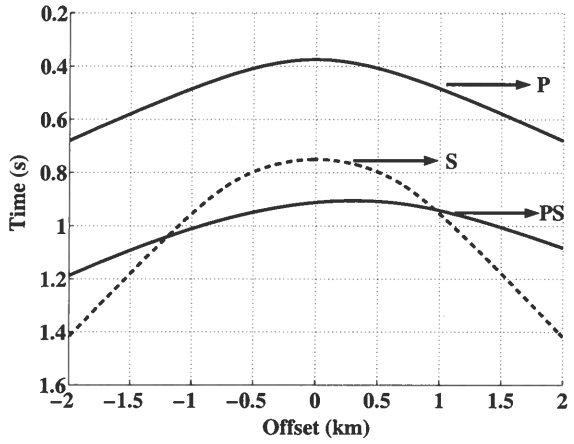

Figure 6.8. PP-wave (solid line) and SS-wave (dashed line) CMP gathers from the overburden and a CMP gather of the PS-wave from the bottom of the three-layer model from Figure 6.4. The converted-wave moveout is asymmetric due to the reflector dip ($\phi = 10°$) and the tilt of the symmetry axis ($\nu = 25°$).

assumed that the SS-wave overburden traveltime (t^o_{SS}) is already obtained by applying the PP+PS=SS method to the overburden PP- and PS-waves. The interval PS-wave traveltime for the shot-receiver coordinates S and R [equation (6.6)] can be expressed as

$$t^i_{PS}(S,R) = t^{eff}_{PS}(x^{(1)},x^{(2)}) - \frac{1}{2}\left(t^o_{SS}(x^{(2)},x^{(4)}) + t^o_{PP}(x^{(1)},x^{(3)})\right). \qquad (6.9)$$

Implementation of this layer-stripping algorithm for PS-waves is similar to that described above for PP-waves. The PS-wave traveltime function (τ_{PS}) for the output location $[x^{(3)},x^{(4)}]$ is found as

$$\tau_{PS}(x^{(3)},x^{(4)}) = t^o_{PP}(x^{(1)},x^{(3)}) + t^o_{SS}(x^{(2)},x^{(4)}) - t^{eff}_{PP}(x^{(1)},x^{(2)}). \qquad (6.10)$$

The stationary points are estimated by locating the minimum of τ_{PS} in both the $x^{(1)}$ and $x^{(2)}$ directions. The interval traveltime and shot-receiver coordinates are then computed by substituting the stationary points into equations (6.9) and (6.6).

The accuracy of the layer-stripping technique for PS-waves is verified for the three-layer model in Figure 6.4. The ray-traced traveltimes (Figure 6.8) were generated for the PP- and SS-waves in the overburden and for the PS-waves from the bottom of the model. The interval PS-wave traveltimes and the shot-receiver coordinates obtained from the layer-stripping algorithm almost coincide with the ray-tracing results (Figures 6.9 and 6.10).

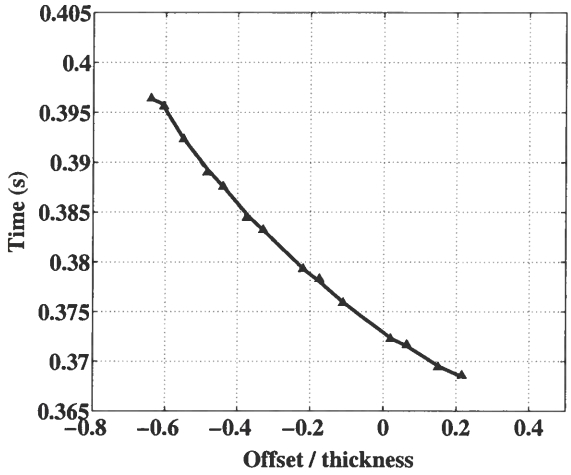

Figure 6.9. Interval PS-wave traveltime in the bottom layer of the model from Figure 6.4 as a function of offset for the shot-receiver coordinates shown in Figure 6.10. The ray-traced traveltime (solid line) practically coincides with that computed from the layer-stripping algorithm (triangles).

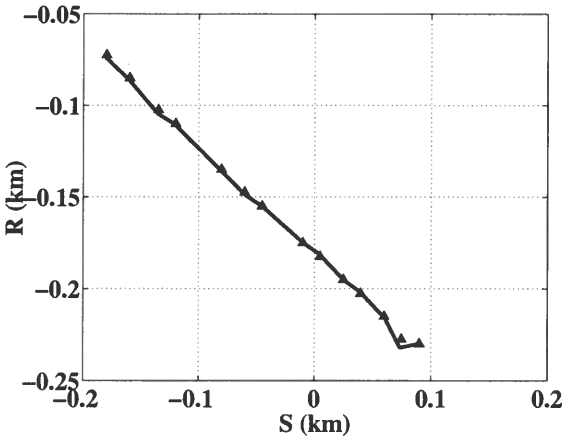

Figure 6.10. Shot and receiver coordinates obtained from a random selection of output points $[x^{(3)}, x^{(4)}]$ using the data from Figure 6.8.

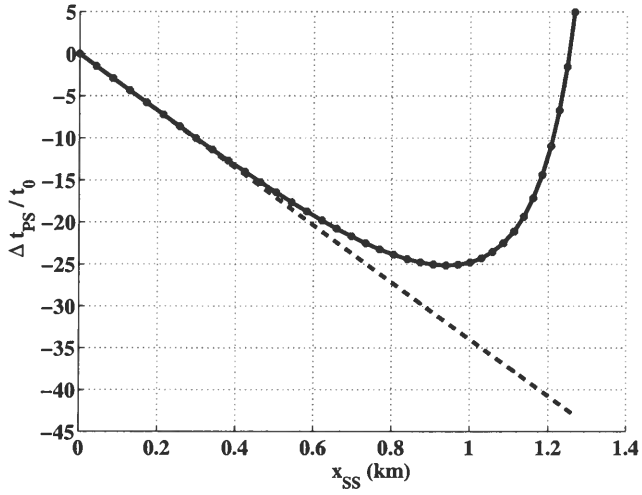

Figure 6.11. Normalized time asymmetry Δt_{PS} for the PSV-wave in a dipping TTI layer. The exact asymmetry factor and the weak-anisotropy approximation (6.11) are marked by the solid and dashed lines, respectively. The asymmetry attributes are computed using the offset-to-depth ratio of PP and PS data close to two. The medium parameters are $V_{P0} = 4$ km/s, $V_{S0} = 2$ km/s, $\epsilon = 0.1$, $\delta = -0.1$, $\nu = 25°$, $\phi = 40°$, and $z_d = 1$ km.

6.3 Remarks on moveout asymmetry in arbitrary anisotropic media

The weak-anisotropy, small-offset approximation for time and offset asymmetry were derived in Chapter 3 and 4 for a TTI layer. In Appendix H, the leading-order term of the time asymmetry attribute for arbitrarily anisotropic media is expressed in terms of pure-mode attributes (NMO velocities, zero-offset traveltimes, and slopes):

$$\Delta t_{PS} = \left(p_{P0} \frac{V^2_{\text{nmo,P}}\, t_{P0}}{V^2_{\text{nmo,S}}\, t_{S0}} - p_{S0} \right) x_{SS}. \tag{6.11}$$

Although the equation is valid for arbitrary reflector shape, the horizontal slowness and NMO velocity of the PP-wave correspond to a different CMP location than those of the SS-wave. For a planar reflector, however, the horizontal slowness and NMO velocity are independent of the CMP location.

The accuracy of equation (6.11) is verified using the following numerical example. For a plane dipping TTI layer with the properties given in the caption of Figure 6.11, I computed the time-asymmetry factor (Δt_{PS}) of the PS wave using the exact equation from Chapter 4. The pure-mode attributes and approximated Δt_{PS} [equation (6.11)] are also computed. Figure 6.11 shows that the linear approximation (dashed line) is accurate for small SS-offsets but deviates from the exact solution with increasing offset due to the influence of higher-order terms.

If the goal is to estimate the model parameters by including the asymmetry information, then it is necessary to include higher-order terms that contribute to the time asymmetry at long offsets. Indeed, the leading term [equation (6.11)] is predicted by the pure-mode signatures and does not contain independent information. This result is consistent with the equations for the asymmetry attributes in the previous chapters. In Chapter 3, I showed that the linear term in x_{SS} for Δt_{PS} in a horizontal TTI layer goes to zero. In Chapter 4, equation (6.11) was derived for the model of a dipping TTI layer with the symmetry axis orthogonal to the reflector.

The results of Appendix H help to find the relationship between the PP- and SS-wave offsets obtained from the PP+PS=SS method. If the layer is horizontal, laterally homogeneous, and anisotropic with a horizontal symmetry plane, the PP- and SS-waves will have the same CMP location, and equation (H.12) can be used to determine the lateral position of the conversion point (x_c) as a function of the converted-wave offset (x):

$$\frac{x_c}{x} \equiv \frac{x_{PP}}{x_{PP}+x_{SS}} = \frac{1}{1+\frac{V^2_{\text{nmo,S}}\, t_{S0}}{V^2_{\text{nmo,P}}\, t_{P0}}}. \tag{6.12}$$

This result is same as the expression for the lateral coordinate of the conversion point in a VTI medium [Thomsen, 1999, equation (27)],

$$\begin{aligned} \frac{x_c}{x} &= \frac{1}{1+\frac{1}{\gamma_{eff}}}, \\ \gamma_{eff} &\equiv \frac{V^2_{\text{nmo,P}}\, t_{P0}}{V^2_{\text{nmo,S}}\, t_{S0}}. \end{aligned} \tag{6.13}$$

Therefore, Thomsen's (1999) result is valid for any anisotropic medium with a horizontal symmetry plane.

As discussed above, the elements of the data vector obtained from pure mode processing are the P- and S-wave NMO velocities, zero-offset traveltimes, and reflection slopes. In general, the data vector has six independent elements, but for the special case of a planar reflector, where the incidence plane coincides with the symmetry plane, the pure-mode attributes are related to each other by the following constraint (Appendix I),

$$\frac{t_{P0}}{p_{P0}} = \frac{t_{S0}}{p_{S0}}. \tag{6.14}$$

Therefore, the pure modes provide at most five independent data elements. In Chapter 4, equation (6.14) was obtained for the special case of a dipping TTI layer with the symmetry axis orthogonal to the layer's bottom.

6.4 Summary

In this chapter, I showed that the interval asymmetry attributes of PS-waves can be obtained in a laterally homogeneous medium as well as for a dipping layer beneath a stack of horizontal layers. The proposed layer-stripping technique is exact and can also be used to obtain the interval time and offset for pure modes. I also approximated the time asymmetry in a heterogeneous, arbitrary anisotropic medium and derived a constraint on the pure-mode attributes for a homogeneous layer above a planar reflector, which is valid when the incidence plane coincides with a symmetry plane of the medium.

Chapter 7

Discussion and Conclusions

The moveout asymmetry of mode-converted waves causes complications in seismic processing and can be removed by applying the PP+PS=SS method introduced by Grechka & Tsvankin (2002b). This method makes it possible to compute the traveltimes of primary SS reflections (if S-waves are not excited in the survey) from PP and PS data prior to anisotropic velocity analysis. In the PP+PS=SS method, however, one needs to pick prestack reflection traveltimes of PP and PS-waves along a selected horizon. Although this is feasible in principle (Grechka et al., 2002b), prestack traveltime picking is known to be tedious, labor-intensive, and noise prone.

I described a technique that not only makes traveltime picking unnecessary but also produces seismograms that resemble pure shear-wave reflection data for all horizons. This automatic procedure generates ΨS data that have the kinematics of pure shear-wave primaries. As a result, conventional velocity analysis performed on ΨS CMP gathers yields SS-wave NMO velocities. These velocities, along with those of the PP-waves and the corresponding reflection slopes, can be used for building elastic (usually anisotropic) interval-velocity models.

To construct the ΨS data, one has to integrate specially designed convolutions of PP and PS traces [equations (2.5) and (2.10) in 2D and 3D, respectively]. Successful implementation of this technique requires selecting time gates that enforce the correspondence of PP and PS events and restricting the integration limits.

The maximum offset of ΨS data is always limited by the critical offset for SS-wave data. Although this result directly follows from Snell's law, it has the following important practical implication. When the SS- to PP-wave velocity ratio is small, the corresponding small ratio of the maximum ΨS offset to reflector depth will invariably compromise the quality of shear-wave velocity analysis.

The methodology was tested on both synthetic and field data. The presented case study from the Gulf of Mexico demonstrated that the processing flow can produce useful velocity analysis results. I showed that the anisotropic parameter χ quantifies the effective anisotropy in layer-cake VTI media and can be unambiguously estimated from PP and PS event correlation and the NMO velocities of P- and SV-waves.

A relevant issue not discussed here in detail relates to the errors in establishing event correspondence. Substantial errors in correlating PP and PS events lead to convolving the wrong PP and PS arrivals and, therefore, produce erroneous SS-wave NMO velocities. Sometimes those errors are relatively easy to recognize. I also examined the influence of small deviations from correct event correlation on the output shear-wave zero-offset times

and NMO velocities. I found that the ratio of errors in t_{SS0} and $V_{S,\mathrm{nmo}}$ is always positive. Therefore, when the velocity $V_{S,\mathrm{nmo}}$ increases with t_{SS0} (which is often the case), it will not be severely distorted because the erroneous values of $V_{S,\mathrm{nmo}}$ and t_{SS0} tend to fall relatively close to the correct trend $V_{S,\mathrm{nmo}}(t_{SS0})$.

Several issues related to the PP+PS=SS method were not addressed in this thesis. First, subhorizontally propagating ΨP-waves generated by this procedure might be used to get more accurate estimates of anisotropic coefficient η than those obtained from P-wave nonhyperbolic moveout. A similar idea, although for PS- rather than ΨP-waves, was proposed by Grechka & Tsvankin (2002a). A second potential research area lies in making use of the ΨS-wave AVO behavior. I derived an equation that governs the amplitudes of ΨS-waves in a heterogeneous anisotropic model and showed its weak-contrast, weak-anisotropy approximation for a special case of isotropic halfspace. For anisotropic models, the approximation for ΨS-waves amplitudes is complicated, and it is easier to work with the original PS-wave amplitudes. Also, the PP+PS=SS method can be used to resort PS data in a common-conversion-point (CCP) gather. Finally, generating ΨS-waves and estimating shear-wave velocities provides a basis for performing migration of ΨS data.

While the replacement of converted waves with pure-mode SS reflections is convenient for processing purposes, it removes the PS-wave moveout asymmetry that can help in estimating the anisotropic parameters. I presented a modification of the PP+PS=SS method designed to supplement the computed SS data with such asymmetry attributes of the converted waves as the difference Δt_{PS} between the "reciprocal" traveltimes and the vector sum of the corresponding offsets (Δx_{PS}). These asymmetry attributes of PS(PSV)-waves were combined with the NMO velocities and zero-offset traveltimes of PP-waves and the constructed SS-waves in a nonlinear inversion algorithm. Without the asymmetry information, the parameter estimation for this model is strongly nonunique. However, including the PS-wave moveout asymmetry attributes removes this ambiguity and makes the 2D inversion sufficiently stable if the symmetry axis deviates by 10° or more from the vertical (VTI) and horizontal (HTI) directions.

The inversion algorithm developed here can be used for characterizing a system of obliquely dipping penny-shaped cracks embedded in a layer-cake isotropic medium (Angerer et al., 2002). Grechka & Tsvankin (2004) demonstrate that wide-azimuth seismic data can be inverted even for the parameters of the more complicated model that includes penny-shaped cracks in a VTI background. Their method operates with only pure-mode reflections but the vertical velocities are assumed to be known. It is possible that the addition of the asymmetry attributes of PS-waves to the signatures of pure PP and SS reflections can make *a priori* information for their model unnecessary. Note that according to the feasibility study by Grechka & Tsvankin (2003), seismic data can constrain the parameters of up to four dipping systems of penny-shaped cracks embedded in either isotropic or VTI host rock.

The modified PP+PS=SS method was also applied to the inversion of multicomponent (PP and PS) data acquired over a dipping TTI layer with the symmetry axis orthogonal to the layer's bottom. Such a model is used to describe dipping shale layers in fold-and-thrust belts (such as the Canadian Foothills).

The weak-anisotropy, small-offset approximation for the time (Δt_{PS}) and offset (Δx_{PS})

asymmetry factors show that the independent information for the parameter-estimation procedure is contained only in the higher-order terms. The stability tests for noise-contaminated input data indicate that the 2D inversion in the symmetry-axis plane gives acceptable results if the tilt exceeds 40° and, for high-quality input PS data, for the range of moderate tilts $25° < \nu < 40°$.

It should be emphasized that 2D moveout inversion of just pure-mode (PP and SS) data in the symmetry-axis plane is nonunique, and even 3D inversion breaks down for small and moderate tilts ν of the symmetry axis. The addition of the PS-wave asymmetry attributes to the NMO velocities, zero-offset traveltimes, and reflection time slopes of the recorded PP-waves and the constructed SS-waves can help to invert 2D data in the symmetry-axis plane without *a priori* information. The inversion algorithm is designed as a two-stage procedure, with the factors Δt_{PS} and Δx_{PS} computed only for the family of plausible models that fit the pure-mode data.

The inversion algorithm developed here can be used to build TTI velocity models in depth from multicomponent reflection data. Taking tilted transverse isotropy into account is particularly important in the presence of dipping shale layers, which are common in fold-and-thrust belts and near salt domes. The estimated parameters can help not only in imaging beneath TTI layers, but also in qualitative lithology discrimination.

Using a physical modeling dataset, I showed that PP and PS reflection data are indeed sufficient to recover all parameters of a horizontal TTI layer. I collected multicomponent, multioffset data with different experiment settings, one with a contact transducer and another with a laser vibrometer. The data were processed using the modified PP+PS=SS method and the model parameters were estimated by combining the asymmetry attributes with the pure-mode NMO velocities, zero-offset traveltimes, and reflection slopes. The inverted model parameters were validated by comparison with the results of transmission experiments. The estimated parameters not only predict the traveltime of the direct P-wave arrival but also indicate the presence of a cusp in S-wave transmission data. The transmitted wavefield was reproduced using the spectral element method with the model parameters estimated from the reflection experiment.

I also showed that the interval asymmetry attributes of PS-waves can be obtained in multilayered media. This layer-stripping algorithm is valid for laterally homogeneous media and a dipping interface beneath a stack of horizontal layers. For the model with a dipping interface, the layers above the target horizon must be laterally homogeneous and have a horizontal symmetry plane. The proposed technique is exact and can also be used to obtain the interval time and offset for pure modes. I also found an approximation for the time asymmetry in heterogeneous arbitrary anisotropic media and derived a constraint on the pure-mode attributes for a homogeneous layer above a planar reflector.

The proposed parameter-estimation algorithm is designed for anisotropic velocity analysis in TTI medium. The estimated anisotropic parameters can help in sorting the PS-wave data into common-conversion-point gathers using anisotropic ray tracing. The CCP-sorted PS-waves gathers can be used for migration, AVO analysis, and other conventional processing steps. If the medium is assumed to be laterally homogeneous and anisotropic with a horizontal symmetry plane, then the lateral position of the conversion point can

be directly obtained from the PP+PS=SS method, which can be used for more accurate depth-dependent CCP binning.

In the PP+PS=SS method, the SS-wave traveltimes and asymmetry attributes are obtained for a limited range of offsets, restricted by the acquisition geometry of the P-wave data. Hence, not all information contained in the PS-wave gathers is captured by either the SS-wave traveltimes or the asymmetry attributes. These additional information of PS-wave data can be utilized in imaging or AVO analysis with the help of the estimated anisotropic parameters.

References

Aki, K., and Richards, P.G., 1980 Quantitative seismology. Vol. 1, W.N. Freeman & Co.

Alkhalifah, T., and Tsvankin, I., 1995 Velocity analysis for transversely isotropic media. *Geophysics*, **60**, 1550–1566.

Angerer, E., Horne, S. A., Gaiser, J. E., Walters, R., Bagala, S. and Vetri, L., 2002 Characterization of dipping fractures using PS mode-converted data. 72th Annual International Meeting, Society of Exploration Geophysicists, Expanded Abstracts, 1010–1013.

Bakulin, A., Grechka, V., and Tsvankin, I., 2000 Estimation of fracture parameters from reflection seismic data – Part I: HTI model due to a single fracture set. *Geophysics*, **65**, 1788–1802.

Cohen, J. K., 1998 A convenient expression for the NMO velocity function in terms of ray parameter. *Geophysics*, **63**, 275–278.

Dellinger, J. and Vernick, L., 1994 Do traveltimes in pulse-transmission experiments yield anisotropic group or phase velocities?. *Geophysics*, **59**, 1774–1779.

Dewangan, P., & Tsvankin, I. 2004a Application of PS-wave moveout asymmetry in parameter estimation for tilted TI media – Part I: Horizontal TTI layer. *Geophysics, under review.*

Dewangan, P., & Tsvankin, I. 2004b Application of PS-wave moveout asymmetry in parameter estimation for tilted TI media – Part II: Dipping TTI layer. *Geophysics, under review.*

Dix, C.H., 1955 Seismic velocities from surface measurements. *Geophysics*, **20**, 68–86.

Isaac, H. J., & Lawton, D., 1999 Image mispositioning due to dipping TI media: A physical seismic modeling study. *Geophysics*, **64**, 1230–1238.

Komatitsch, D., Barnes, C., and Tromp, J., 2000 Simulation of anisotropic wave propagation based upon a spectral element method. *Geophysics*, **65**, 1251–1260.

Lawton, D. C., Issac, J. H., Vestrum, R. W., and Leslie, J. M., 2001 Slip-sliding away - some practical implications of seismic velocity anisotropy on depth imaging. *The Leading Edge*, **20**, 70–73.

Martynov, V. N., and Mikhailenko, B.G., 1984 Numerical modelling of elastic waves in anisotropic inhomogeneous media for the halfspace and the sphere. *Geophys. J. R. Astr. Soc*, **76**, 53–63.

Pelissier, M. A., Thomas-Betts, A., and Vestergaard, P. D., 1991 Azimuthal variations in scattering amplitudes induced by transverse isotropy. *Geophysics*, **56**, 1584–1595.

Grechka, V., and Dewangan, P., 2003 Generation and processing of pseudo shear-wave data: Theory and case study. *Geophysics*, **68**, 1807–1816.

Grechka, V., and Tsvankin, I., 1998 3-D description of normal moveout in anisotropic inhomogeneous media. *Geophysics*, **63**, 1079–1092.

Grechka, V., and Tsvankin, I., 1999 3-D moveout inversion in azimuthally anisotropic media with lateral velocity variation: Theory and a case study. *Geophysics*, **64**, 1202–1218.

Grechka, V., and Tsvankin, I., 2000 Inversion of azimuthally dependent NMO velocity in transversely isotropic media with a tilted axis of symmetry. *Geophysics*, **65**, 232–246.

Grechka, V., and Tsvankin, I., 2002a The joint nonhyperbolic moveout inversion of PP and PS data in VTI media. *Geophysics*, **67**, 1929–1932.

Grechka, V., and Tsvankin, I., 2002b PP+PS=SS. *Geophysics*, **67**, 1961–1971.

Grechka, V., and Tsvankin, I., 2003 Feasibility of seismic characterization of multiple fracture sets. *Geophysics*, **68**, 1399–1407.

Grechka, V., and Tsvankin, I., 2004 Characterization of dipping fractures in a transversely isotropic background. *Geophysical Prospecting*, **52**, 1–10.

Grechka, V., Tsvankin, I., and Cohen, J. K., 1999a Generalized Dix equation and analytic treatment of normal-moveout velocity for anisotropic media. *Geophysical Prospecting*, **47**, 117–148.

Grechka, V., Theophanis, S. and Tsvankin, I., 1999b Joint inversion of P- and PS-waves in orthorhombic media: Theory and a physical modeling study. *Geophysics*, **64**, 146–161.

Grechka, V., Pech, A., Tsvankin, I., and Han, B., 2001 Velocity analysis for tilted transversely isotropic media: A physical-modeling example. *Geophysics*, **66**, 904–910.

Grechka, V., Pech, A., and Tsvankin, I., 2002a Multicomponent stacking-velocity tomography for transversely isotropic media. *Geophysics*, **67**, 1564–1574.

Grechka, V., Tsvankin, I., Bakulin, A., and Hansen, J.O., 2002b Joint inversion of PP and PS reflection data for VTI media: A North Sea case study. *Geophysics*, **67**, 1382–1395.

Hale, D., 1992, Imaging salt with turning seismic waves. *Geophysics*, **57**, 1453–1462.

Sarg, J. F., and Schuelke, J. S., 2003 Integrated seismic analysis of carbonate reservoirs: From the framework to the volume attributes. *The Leading Edge*, **22**, 640–645.

Thomsen, L., 1986 Weak elastic anisotropy. *Geophysics*, **51**, 1954–1966.

Thomsen, L., 1999, Converted-wave reflection seismology over inhomogeneous, anisotropic media. *Geophysics*, **64**, 678–690.

Tsvankin, I., 1995 Normal moveout from dipping reflectors in anisotropic media. *Geophysics*, **60**, 268–284.

Tsvankin, I., 1997 Reflection moveout and parameter estimation for horizontal transverse isotropy. *Geophysics*, **62**, 614–629.

Tsvankin, I., 2001 Seismic signatures and analysis of reflection data in anisotropic media. Elsevier Science Publ. Co., Inc.

Tsvankin, I., and Grechka, V., 2000 Dip moveout of converted waves and parameter estimation in transversely isotropic media. *Geophysical Prospecting*, **48**, 257–292.

Tsvankin, I., and Grechka, V., 2002 3D description and inversion of reflection moveout of PS-waves in anisotropic media. *Geophysical Prospecting*, **50**, 301–316.

Tsvankin, I., and Thomsen, L., 1994 Nonhyperbolic reflection moveout in anisotropic media. *Geophysics*, **59**, 1290–1304.

Vestrum, R. W., Lawton, D. C., and Schmid, R., 1999 Imaging structures below dipping TI media. *Geophysics*, **64**, 1239–1246.

Appendix A

Kinematics of ΨS-waves

Here I prove that integral (2.5) applied to PP and PS data produces waves that have the kinematics of pure SS-wave primaries when the input PP and PS traces contain only primaries events. Applying the Fourier transform to equation (2.5) yields

$$W_{\Psi S}(\omega, x^{(3)}, x^{(4)}) = \iint \Big[\quad W_{PS}(\omega, x^{(1)}, x^{(3)})\, W^{\star}_{PP}(\omega, x^{(1)}, x^{(2)}) \times W_{PS}(\omega, x^{(2)}, x^{(4)}) \Big]\, dx^{(1)}\, dx^{(2)}, \tag{A.1}$$

where ω is radial frequency, W_{PP}, W_{PS}, and $W_{\Psi S}$ are the spectra of PP, PS, and ΨS traces, respectively, and the star denotes complex conjugate.

If the input PP and PS traces consist of primaries reflected from the interface, their spectra have the form

$$W^{\star}_{PP}(\omega, x^{(1)}, x^{(2)}) = F^{\star}_{PP}(\omega)\, A^{\star}_{PP}(x^{(1)}, x^{(2)})\, e^{-i\omega t_{PP}(x^{(1)}, x^{(2)})} \tag{A.2}$$

and

$$W_{PS}(\omega, x^{(s)}, x^{(r)}) = F_{PS}(\omega)\, A_{PS}(x^{(s)}, x^{(r)})\, e^{i\omega t_{PS}(x^{(s)}, x^{(r)})}. \tag{A.3}$$

Here, A_{PP} and A_{PS} represent the amplitudes of the reflected PP- and PS-waves, F_{PP} and F_{PS} denote the spectra of their wavelets, and the indexes r and s take two pairs of values $\{s = 1,\ r = 3\}$ and $\{s = 2,\ r = 4\}$. Substituting equations (A.2) and (A.3) into integral (A.1), I obtain

$$W_{\Psi S}(\omega, x^{(3)}, x^{(4)}) = \quad F^{2}_{PS}(\omega)\, F^{\star}_{PP}(\omega) \times \iint \Big[A_{PS}(x^{(1)}, x^{(3)})\, A^{\star}_{PP}(x^{(1)}, x^{(2)})\, A_{PS}(x^{(2)}, x^{(4)}) \times e^{i\omega\tau} \Big]\, dx^{(1)}\, dx^{(2)}. \tag{A.4}$$

The time τ in this equation is given by

$$\begin{aligned} \tau \quad &\equiv \tau(x^{(1)}, x^{(2)}, x^{(3)}, x^{(4)}) \\ &= t_{PS}(x^{(1)}, x^{(3)}) + t_{PS}(x^{(2)}, x^{(4)}) - t_{PP}(x^{(1)}, x^{(2)}). \end{aligned} \tag{A.5}$$

Since the goal is to show that the ΨS event has the kinematics of the pure SS-wave

primary, integral (A.4) has to be evaluated in the limit $\omega \to \infty$. This can be done with the stationary phase method. According to this method, the main contributions to the integral occur around the points $\{x^{(1)}, x^{(2)}\}$ that satisfy the conditions of stationarity:

$$\frac{\partial \tau}{\partial x^{(1)}} = \frac{\partial \tau}{\partial x^{(2)}} = 0\,. \tag{A.6}$$

Note that equations (A.6) coincide with expressions (2.2) and (2.3), which represent the requirement of matching the reflection slopes of the reflected PP- and PS-waves (Figure 2.1). If equations (A.6) have a solution

$$\left\{x^{(1)}, x^{(2)}\right\} \equiv \boldsymbol{x}_0 \equiv \left\{x^{(1)}(x^{(3)}, x^{(4)}),\ x^{(2)}(x^{(3)}, x^{(4)})\right\}\,, \tag{A.7}$$

the time function τ defined by equation (A.5) becomes equal to the traveltime t_{SS} given by formula (2.4). Therefore, in the high-frequency limit the kinematics of a pure SS-wave primary is, indeed, represented by integral (A.4).

Appendix B

Weak-contrast, small-offset approximation for P-, PS-, and ΨS-wave amplitudes in isotropic half-space

Here, I derive the weak-contrast, small-offset approximation for ΨS-wave amplitdes in an isotropic half-space. The approximate reflection coefficient for plane P-waves (Aki & Richards, 1980) can be expressed as

$$R_{PP} \approx \frac{1}{2}\left(1-4\beta^2p^2\right)\frac{\Delta\rho}{\bar{\rho}}+\frac{1}{2\cos^2 i}\frac{\Delta\alpha}{\bar{\alpha}}-4\beta^2p^2\frac{\Delta\beta}{\bar{\beta}}, \tag{B.1}$$

where α, β, ρ are the P- and S-wave velocities and density, respectively. The bar refers to the mean value and 'Δ' to the difference between the properties of the two halfspaces; p is the horizontal slowness. Using Snell's law,

$$\frac{\sin i}{\alpha}=\frac{\sin j}{\beta}=p, \tag{B.2}$$

where i and j are the P- and S-wave incidence angles, we can express equation (B.1) in terms of the S-wave incidence angle,

$$\begin{aligned} R_{PP} &\approx \frac{1}{2}\frac{\Delta Z}{\bar{Z}}+\left(\frac{1}{2}\frac{\Delta\alpha}{\bar{\alpha}}g^2-2\frac{\Delta G}{\bar{G}}\right)\sin^2 j+\frac{1}{2}\frac{\Delta\alpha}{\bar{\alpha}}g^4\sin^4 j; \\ g &\equiv \frac{\alpha}{\beta}. \end{aligned} \tag{B.3}$$

Here Z and G are the values of the P-wave impedance and shear modulus, respectively. The approximate reflection coefficient for PS-waves (Aki & Richards, 1980) can be expressed in a similar way,

$$\begin{aligned} R_{PS} &\approx -\left(\frac{g}{2}\frac{\Delta\rho}{\bar{\rho}}+\frac{\Delta G}{\bar{G}}\right)\sin j+\left(\frac{g^2}{2}\frac{\Delta G}{\bar{G}}+g\frac{\Delta G}{\bar{G}}-\frac{g}{4}\frac{\Delta\rho}{\bar{\rho}}\right)\sin^3 j \\ &+ \left[\frac{1}{8}g\frac{\Delta G}{\bar{G}}\left(g^3+2g+4\right)\right]\sin^5 j. \end{aligned} \tag{B.4}$$

The amplitude of the ΨS-wave can be obtained by substituting equations (B.3) and (B.4) into equation (2.8),

$$
\begin{aligned}
R_{\Psi S} &\approx T_1 \sin^2 j + T_2 \sin^4 j + T_3 \sin^6 j; \qquad \text{(B.5)}\\
T_1 &= \frac{1}{8}\left(g\frac{\Delta\rho}{\bar{\rho}} + 2\frac{\Delta G}{\bar{G}}\right)^2 \frac{\Delta Z}{\bar{Z}},\\
T_2 &= -2\left(\frac{\Delta G}{\bar{G}}\right)^3 + \frac{g}{4}\left(-8(\frac{\Delta G}{\bar{G}})^2\frac{\Delta\rho}{\bar{\rho}} - (\frac{\Delta G}{\bar{G}})^2\frac{\Delta Z}{\bar{Z}} + R\right)\\
&+ \frac{g^2}{2}\left(-\frac{\Delta G}{\bar{G}}(\frac{\Delta\rho}{\bar{\rho}})^2 + (\frac{\Delta G}{\bar{G}})^2\frac{\Delta\alpha}{\bar{\alpha}} - (\frac{\Delta G}{\bar{G}})^2\frac{\Delta Z}{\bar{Z}} - R\right)\\
&+ \frac{g^3}{4}\left(2\frac{\Delta G}{\bar{G}}\frac{\Delta\rho}{\bar{\rho}}\frac{\Delta\alpha}{\bar{\alpha}} - R\right),\\
T_3 &= \frac{g}{2}\left(8(\frac{\Delta G}{\bar{G}})^3 - (\frac{\Delta G}{\bar{G}})^2 K\right)\\
&+ \frac{g^2}{4}\left(8(\frac{\Delta G}{\bar{G}})^3 + 8(\frac{\Delta G}{\bar{G}})^2\frac{\Delta\rho}{\bar{\rho}} + (\frac{\Delta G}{\bar{G}})^2\frac{\Delta Z}{\bar{Z}} - R\right)\\
&+ \frac{g^3}{2}\left(3(\frac{\Delta G}{\bar{G}})^2\frac{\Delta\rho}{\bar{\rho}} - (\frac{\Delta G}{\bar{G}})^2\frac{\Delta\alpha}{\bar{\alpha}}\right)\\
&+ \frac{g^4}{2}\left(-\frac{\Delta G}{\bar{G}}\frac{\Delta\rho}{\bar{\rho}}\frac{\Delta\alpha}{\bar{\alpha}}\right)\\
&+ \frac{g^5}{16}\left(4\frac{\Delta G}{\bar{G}}\frac{\Delta\rho}{\bar{\rho}}\frac{\Delta\alpha}{\bar{\alpha}} - R\right),\\
K &\equiv 3\frac{\Delta\rho}{\bar{\rho}} + \frac{\Delta\alpha}{\bar{\alpha}},\\
R &\equiv \frac{\Delta G}{\bar{G}}\frac{\Delta\rho}{\bar{\rho}}\frac{\Delta Z}{\bar{Z}}.
\end{aligned}
$$

Since the derivation is carried out for small offsets, where all angles are real, the P-wave reflection coefficient is also real.

Appendix C

Approximate time asymmetry factor for the PSV-wave in a horizontal TTI layer

For a weakly anisotropic TTI layer ($|\epsilon| \ll 1$ and $|\delta| \ll 1$), the asymmetry factor Δt_{PS} in the slowness domain [equations (3.10) and (3.4)] can be linearized in the anisotropic coefficients ϵ and δ. Without losing generality, the symmetry axis (unit vector $\boldsymbol{a}$) is assumed to lie in the coordinate plane $[x_1, x_3]$ (Figure C.1):

$$\boldsymbol{a} \equiv [a_1, 0, a_3] = [\sin\nu, 0, \cos\nu]\,, \tag{C.1}$$

where ν is the tilt of the symmetry axis from the vertical direction. To obtain the vertical slowness q as a function of the horizontal slowness components p_1 and p_2 for both legs of the PS reflected ray, I use the approach suggested by Grechka and Tsvankin (2000, Appendix B). The component q can be represented as the sum of the isotropic value $\tilde{q}$ and the anisotropy-induced correction term Δq:

$$q \equiv p_3 = \tilde{q} + \Delta q\,. \tag{C.2}$$

For P-waves in an isotropic medium with velocity V_{P0}, the vertical slowness is given by

$$\tilde{q} = \sqrt{\frac{1}{V_{P0}^2} - p_1^2 - p_2^2}\,. \tag{C.3}$$

In the weak-anisotropy approximation Δq can be treated as the linear term in a Taylor series expansion of q in ϵ and δ for fixed horizontal slownesses p_1 and p_2:

$$\Delta q = -\frac{1}{\partial\mathcal{F}/\partial q}\left(\frac{\partial\mathcal{F}}{\partial\epsilon}\,\epsilon + \frac{\partial\mathcal{F}}{\partial\delta}\,\delta\right), \tag{C.4}$$

where $\mathcal{F}(q, p_1, p_2, V_{P0}, V_{S0}, \epsilon, \delta, \nu) = 0$ is the Christoffel equation for P- and SV-waves in TTI media.

Next, I obtain the partial derivatives $q_{,i} \equiv \partial q/\partial p_i$ $(i = 1, 2)$ for the P-wave, substitute them into equation (3.6) and then (3.10), and carry out further linearization using symbolic software Mathematica. The weak-anisotropy approximation for the contribution of the P-leg of the PS-wave to the asymmetry factor has the form

$$\Delta t_P = 4\,z\,(\delta - \epsilon)\,p_1 V_{P0}^2\,\sin 2\nu\,[p_2^2 + (2p_1^2 + p_2^2)\cos 2\nu]\,. \tag{C.5}$$

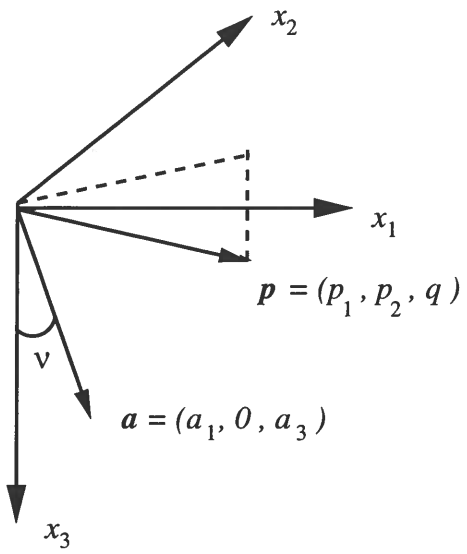

Figure C.1. The symmetry axis is defined by the unit vector $\boldsymbol{a}$ confined to the $[x_1, x_3]$-plane. The slowness vector $\boldsymbol{p}$ has an arbitrary orientation.

The linearized asymmetry contribution of the S-leg can be found from the P-wave equation (C.5) by using the following general transformation rule (Tsvankin, 2001, p. 26):

$$V_{P0} \to V_{S0},\ \epsilon \to 0,\ \delta \to \sigma\,;$$

$$\sigma \equiv \frac{V_{P0}^2}{V_{S0}^2}\,(\epsilon - \delta)\,.$$

Taking into account that the asymmetry for the S-leg of a given PS-ray has to be computed for the opposite sign of the horizontal slowness [so p_1 in equation (C.5) has to be replaced with $-p_1$, and p_2 with $-p_2$], I find

$$\Delta t_S = -4\,z\,(\epsilon - \delta)\,p_1 V_{P0}^2 \sin 2\nu\,[p_2^2 + (2p_1^2 + p_2^2)\cos 2\nu] = \Delta t_P\,. \tag{C.6}$$

Appendix D

Azimuthal variation of the offset $x_{\min}$

The slope dt/dx of the CMP moveout curve for any pure or converted reflection mode is determined by the difference between the projections onto the CMP line of the slowness vectors at the source and receiver locations[1] (Tsvankin and Grechka, 2000; Tsvankin, 2001, Appendix 5B). This general result, which is valid for any heterogeneous, anisotropic medium, can be used to find the offset $x_{\min}$ of the PS-wave traveltime minimum where the moveout slope goes to zero. For a horizontal, laterally homogeneous layer, the horizontal slowness has the same absolute value for both legs of the reflected ray, and the slope can vanish only for a ray with the slowness vector orthogonal to the CMP line.

Suppose p_α is the projection of the slowness vector onto the CMP line that makes the angle α with the x_1-axis, and p_t is the slowness projection onto the orthogonal $(\alpha + 90°)$ direction. The offset $x_{\min}(\alpha)$ then corresponds to the PS ray for which $p_\alpha = 0$. Rotating the slowness vector by the angle α in the horizontal plane yields

$$p_1 = p_\alpha \cos\alpha - p_t \sin\alpha\,, \tag{D.1}$$

$$p_2 = p_\alpha \sin\alpha + p_t \cos\alpha\,. \tag{D.2}$$

The offset x can be parametrically represented as [equations (3.7) and (3.8)]

$$x = z\sqrt{(q_{,1P} - q_{,1S})^2 + (q_{,2P} - q_{,2S})^2}\,. \tag{D.3}$$

To find $x_{\min}$ from equation (D.3), the derivatives $q_{,i} \equiv \partial q/\partial p_i$ $(i = 1, 2)$, which are derived for weakly anisotropic TTI media in Appendix C, have to be evaluated for $p_\alpha = 0$.

Substituting $q_{,i}$ from Appendix C into equation (D.3) and further linearizing the result in ϵ and δ produces x as a function of p_1 and p_2, which can be replaced by p_α and p_t using equations (D.1) and (D.2). The component p_α is then set to zero, while p_t can be found from equation (3.9) for the azimuth α. Linearizing equation (3.9) and using equations (D.1) and (D.2) with $p_\alpha = 0$ allows us to obtain p_t:

$$p_t = \frac{x_0 \sin\alpha}{V_{S0} - V_{P0}}\,, \tag{D.4}$$

where $x_0 = x_{\min}(\alpha = 0°)$ is the value of $x_{\min}$ in the symmetry-axis plane.

[1] In this formulation both legs of the reflected ray are treated as upgoing waves.

Since the slowness vectors of reflected rays propagating in the symmetry-axis plane cannot have out-of-plane components, the offset x_0 corresponds to the ray with the vertical slowness vector ($p_\alpha = p_t = p_1 = p_2 = 0$). Evaluating x from equation (D.3) with $p_1 = p_2 = 0$ gives

$$x_0 = -z \left[\epsilon \sin 2\nu - \frac{1}{2} (\epsilon - \delta) \left(1 + \frac{V_{P0}^2}{V_{S0}^2} \right) \sin 4\nu \right] . \tag{D.5}$$

Finally, I substitute $p_\alpha = 0$ and p_t from equations (D.4) and (D.5) into equation (D.3) to obtain the following expression for the azimuthally varying offset of the moveout minimum:

$$x_{\min}(\alpha) = x_0 \cos \alpha . \tag{D.6}$$

Appendix E

Approximate moveout asymmetry factor in the offset domain

To describe the moveout asymmetry in the offset domain defined in equation (3.14), I express the PS traveltime through the components x_1 and x_2 of the PS-wave offset vector $\boldsymbol{x}_{PS}$ [equation (3.7)]. An approximation for the asymmetry factor in a horizontal TTI layer can be found by expanding the traveltime $t(x_1, x_2)$ in a double Taylor series in the vicinity of the offset $(x_0, 0)$ of the moveout minimum [equation (D.5)],

$$\begin{aligned} t(x_1,x_2) &= t(x_0,0) + \frac{\partial t}{\partial x_1}(x_1-x_0) + \frac{\partial t}{\partial x_2}x_2 \\ &+ \frac{1}{2}\frac{\partial^2 t}{\partial x_1^2}(x_1-x_0)^2 + \frac{1}{2}\frac{\partial^2 t}{\partial x_2^2}x_2^2 + \frac{\partial^2 t}{\partial x_1 \partial x_2}(x_1-x_0)\,x_2 \\ &+ \frac{1}{3!}\frac{\partial^3 t}{\partial x_1^3}(x_1-x_0)^3 + \frac{1}{3!}\frac{\partial^3 t}{\partial x_2^3}x_2^3 \\ &+ \frac{1}{2}\frac{\partial^3 t}{\partial x_1^2 \partial x_2}(x_1-x_0)^2\,x_2 + \frac{1}{2}\frac{\partial^3 t}{\partial x_1 \partial x_2^2}(x_1-x_0)\,x_2^2 + \ldots \end{aligned} \tag{E.1}$$

The traveltime derivatives in equation (E.1) should be evaluated at $(x_1 = x_0\,,\, x_2 = 0)$. Note that the first derivatives $\partial t/\partial x_1$ and $\partial t/\partial x_2$ at $(x_0, 0)$ are equal to zero.

The moveout asymmetry factor in the offset domain can be found from equation (E.1) as

$$\begin{aligned} \Delta t_{PS}(x_1,x_2) &= t_{PS}(x_1,x_2) - t_{PS}(-x_1,-x_2) \\ &= -2\frac{\partial^2 t}{\partial x_1^2}x_1\,x_0 - 2\frac{\partial^2 t}{\partial x_1 \partial x_2}x_2\,x_0 + \frac{1}{3}\frac{\partial^3 t}{\partial x_1^3}(x_1^3 + 3x_1\,x_0^2) \\ &+ x_2\left[\frac{\partial^3 t}{\partial x_1^2 \partial x_2}(x_0^2 + x_1^2) + \frac{\partial^3 t}{\partial x_1 \partial x_2^2}x_1\,x_2 + \frac{1}{3}\frac{\partial^3 t}{\partial x_2^3}x_2^2\right]. \end{aligned} \tag{E.2}$$

Since $[x_1, x_3]$ is a plane of symmetry, $\Delta t_{PS}(x_1, x_2)$ has to be an even function of x_2,

$$\Delta t_{PS}(x_1,x_2) = \Delta t_{PS}(x_1,-x_2)\,. \tag{E.3}$$

Therefore, equation (E.2) should not contain terms linear and cubic in x_2, and

$$\frac{\partial^2 t}{\partial x_1 \partial x_2} = \frac{\partial^3 t}{\partial x_1^2 \partial x_2} = \frac{\partial^3 t}{\partial x_2^3} = 0\,. \tag{E.4}$$

The second- and third-order derivatives in equation (E.2) are convenient to represent in terms of the slowness components of the ray with $p_1 = p_2 = 0$, which corresponds to the offset x_0 (see Appendix D). The time slopes $\partial t/\partial x_i\,(i = 1,2)$ can be expressed through the the horizontal slownesses p_1 and p_2 of the PS-wave using the results of Tsvankin (2001, Appendix 5B):

$$\frac{\partial t}{\partial x_i} = -\,p_i\,(i = 1,2)\,. \tag{E.5}$$

Differentiating $\partial t/\partial x_1$ from equation (E.5) with respect to x_1 and using equation (3.7) yields

$$\frac{\partial^2 t}{\partial x_1^2} = \frac{\partial}{\partial x_1}\frac{\partial t}{\partial x_1} = \frac{-1}{\partial x_1/\partial p_1} = \frac{-1}{z\,(q_{,1P,1P} - q_{,1S,1S})}\,, \tag{E.6}$$

where $q_{,jP,iP} \equiv \partial^2 q_P/(\partial p_j \partial p_i)$ and $q_{,jS,iS} \equiv \partial^2 q_S/(\partial p_j \partial p_i)$.

The third-order derivatives of the traveltime t needed in equation (E.2) can be obtained in a similar fashion:

$$\begin{aligned}\frac{\partial^3 t}{\partial x_1^3} &= \frac{\partial}{\partial x_1}\left(\frac{-1}{\partial x_1/\partial p_1}\right) = \frac{\partial}{\partial p_1}\left(\frac{-1}{\partial x_1/\partial p_1}\right)\left(\frac{\partial p_1}{\partial x_1}\right)\\ &+ \frac{\partial}{\partial p_2}\left(\frac{-1}{\partial x_1/\partial p_1}\right)\left(\frac{\partial p_2}{\partial x_1}\right) = \frac{q_{,1P,1P,1P} - q_{,1S,1S,1S}}{z^2\,(q_{,1P,1P} - q_{,1S,1S})^3}\,,\end{aligned} \tag{E.7}$$

$$\begin{aligned}\frac{\partial^3 t}{\partial x_1 \partial x_2^2} &= \frac{\partial}{\partial x_1}\left(\frac{-1}{\partial x_2/\partial p_2}\right) = \frac{\partial}{\partial p_1}\left(\frac{-1}{\partial x_2/\partial p_2}\right)\left(\frac{\partial p_1}{\partial x_1}\right)\\ &+ \frac{\partial}{\partial p_2}\left(\frac{-1}{\partial x_2/\partial p_2}\right)\left(\frac{\partial p_2}{\partial x_1}\right)\\ &= \frac{q_{,2P,2P,1P} - q_{,2S,2S,1S}}{z^2\,(q_{,2P,2P} - q_{,2S,2S})^2\,(q_{,1P,1P} - q_{,1S,1S})}\,.\end{aligned} \tag{E.8}$$

Here $q_{,jP,iP,kP} \equiv \partial^3 q_P/(\partial p_j \partial p_i \partial p_k)$, $q_{,jS,iS,kS} \equiv \partial^3 q_S/(\partial p_j \partial p_i \partial p_k)$, and the derivative $(\partial p_2/\partial x_1)$ vanishes because $p_2 = 0$ on the x_1-axis.

Using the linearized derivatives of the vertical slowness q from Appendix C leads to

$$\frac{\partial^2 t}{\partial x_1^2} = \frac{2}{z}\left\{ V_{P0}\left[2+\delta+\epsilon+2\epsilon\cos 2\nu+3(\delta-\epsilon)\cos 4\nu\right] \right. \tag{E.9}$$

$$\left. + \; V_{S0}\left(2+\sigma+3\sigma\cos 4\nu\right)\right\}^{-1}, \tag{E.10}$$

$$\frac{\partial^3 t}{\partial x_1^3} = -\frac{12(\epsilon-\delta)\,V_{P0}^2\,\sin 4\nu}{z^2\,(V_{P0}+V_{S0})^3}, \tag{E.11}$$

$$\frac{\partial^3 t}{\partial x_1 \partial x_2^2} = -\frac{4(\epsilon-\delta)\,V_{P0}^2\,\sin 2\nu}{z^2\,(V_{P0}+V_{S0})^3}. \tag{E.12}$$

Substituting equations (E-9)–(E-12) into equation (E.2) and further linearizing the result, I obtain the asymmetry factor as

$$\Delta t_{PS} = -\frac{2\,x_1\,x_0}{z\,(V_{P0}+V_{S0})} - \frac{4(\epsilon-\delta)\,V_{P0}^2\,\sin 4\nu}{z^2\,(V_{P0}+V_{S0})^3}\,x_1^3 - \frac{4(\epsilon-\delta)\,V_{P0}^2\,\sin 2\nu}{z^2\,(V_{P0}+V_{S0})^3}\,x_1\,x_2^2. \tag{E.13}$$

Finally, equation (E.13) can be rewritten in terms of the offset x and the azimuth α of the source-receiver line ($x_1 = x\cos\alpha$, $x_2 = x\sin\alpha$):

$$\Delta t_{PS}(x,\alpha) = -\frac{2\,x\,x_0\,\cos\alpha}{z\,(V_{P0}+V_{S0})} - \frac{4(\epsilon-\delta)\,V_{P0}^2\,\sin 4\nu}{z^2\,(V_{P0}+V_{S0})^3}\,x^3\cos^3\alpha - \frac{4(\epsilon-\delta)\,V_{P0}^2\,\sin 2\nu}{z^2\,(V_{P0}+V_{S0})^3}\,x^3\cos\alpha\,\sin^2\alpha,$$

or

$$\Delta t_{PS}(x,\alpha) = -\frac{2\,x\,x_0\,\cos\alpha}{z\,(V_{P0}+V_{S0})} - \frac{4\,x^3\,(\epsilon-\delta)\,V_{P0}^2\,\sin 2\nu\,\cos\alpha}{z^2\,(V_{P0}+V_{S0})^3}\left(2\cos 2\nu\,\cos^2\alpha+\sin^2\alpha\right). \tag{E.14}$$

Appendix F

Approximate time asymmetry factor for the PSV-wave in a dipping TTI layer

To derive explicit expressions for the PSV-wave time and offset asymmetry factors in a TTI layer, I use the exact parametric representation of converted-wave moveout developed in Tsvankin (2001, Chapter 5) and Tsvankin and Grechka (2002). The PS-wave reflection traveltime in a homogeneous layer above a plane dipping reflector can be found in the following form:

$$t_{PS} \equiv t_P + t_S = z_r \cdot (q_P - p_{1P}\, q_{,1P} - p_{2P}\, q_{,2P} + q_S - p_{1S}\, q_{,1S} - p_{2S}\, q_{,2S}), \tag{F.1}$$

where t_P and t_S are the traveltimes along the P- and S-legs, respectively, z_r is the depth of the conversion point at the reflector, p_1 and p_2 are the horizontal components of the slowness vector (the subscripts "P" and "S" indicate the wave type), $q \equiv p_3$ is the vertical slowness, and $q_{,i} \equiv \partial q / \partial p_i$ $(i = 1, 2)$. According to the convention in Grechka and Tsvankin (2000) and Chapter 3, the x_3-axis points down, and both legs of the PS ray are treated as upgoing waves (i.e., the slownesses are computed for group-velocity vectors that point toward the earth's surface). The depth of the conversion point can be represented in terms of the vertical distance $z_{\rm CMP}$ from the common midpoint (CMP) to the reflector:

$$z_r = \frac{z_{\rm CMP}}{1 + \Delta z}, \tag{F.2}$$

$$\Delta z = \frac{\tan\phi}{2} \left[(q_{,1P} + q_{,1S})\zeta_1 + (q_{,2P} + q_{,2S})\zeta_2 \right]. \tag{F.3}$$

Here $\{\zeta_1, \zeta_2\}$ is a horizontal unit vector in the updip direction and ϕ is the reflector dip.

The source-receiver offset x_{PS} of the PS-wave and the azimuth α of the source-receiver line with respect to the x_1-axis can be written as

$$x_{PS} = |\boldsymbol{x}_{PS}| = \sqrt{x_1^2 + x_2^2}, \tag{F.4}$$

$$\alpha = \tan^{-1}\left(\frac{x_2}{x_1}\right), \tag{F.5}$$

where x_1 and x_2 are the components of the source-receiver vector $\boldsymbol{x}_{PS}$:

$$x_1 = z_r \cdot (q_{,1P} - q_{,1S}), \tag{F.6}$$

$$x_2 = z_r \cdot (q_{,2P} - q_{,2S}) . \tag{F.7}$$

A detailed derivation of equations (F.1)–(F.7) can be found in Tsvankin (2001, Appendix 5E).

For a weakly anisotropic TTI layer ($|\epsilon| \ll 1$ and $|\delta| \ll 1$), the asymmetry factor Δt_{PS} obtained from the PP+PS=SS method [equations (4.1) and (4.2)] can be linearized in the anisotropic coefficients ϵ and δ under the additional assumption of small offset x_{PS}. Here, I consider a TTI layer with tilt of the symmetry axis equal to the reflector dip (Figure F.1). Since the PP+PS=SS method operates with the PP and PS arrivals that have the same reflection point, Snell's law dictates that the projection of the slowness vector onto the reflector is identical (in absolute value) for all reflected waves.

Using simple trigonometric relationships, the slowness components for the incident and reflected P-waves can be written as

$$p_{i1} = p_{int1} \cos\nu + q^{VTI} \sin\nu, \tag{F.8}$$

$$p_{r1} = -p_{int1} \cos\nu + q^{VTI} \sin\nu, \tag{F.9}$$

$$p_{i2} = p_{int2} = -p_{r2}, \tag{F.10}$$

where p_{int1} and p_{int2} are the slowness components of the incident and reflected waves along the interface in the dip and strike directions, respectively, q^{VTI} is the slowness component in the symmetry-axis direction, p_{i1} and p_{r1} are the horizontal slownesses of the incident and the reflected waves in the symmetry-axis (dip) plane (Figure F.1), and p_{i2} and p_{r2} are the slowness components of the incidence and reflected waves in the strike direction. The above relationships between the slownesses remain valid for the S-wave as well.

In the weak-anisotropy approximation, q^{VTI} can be expressed in terms of p_{int1} and p_{int2} using the VTI equations for P-waves (Tsvankin and Grechka, 2000):

$$q^{VTI} = q_{P0} \left\{ 1 - \frac{(p_{int1}^2 + p_{int2}^2)}{q_{P0}^2} \left[\delta + (\epsilon - \delta) (p_{int1}^2 + p_{int2}^2) V_{P0}^2 \right] \right\} , \tag{F.11}$$

$$q_{P0} = \sqrt{\frac{1}{V_{P0}^2} - (p_{int1}^2 + p_{int2}^2)} . \tag{F.12}$$

Substituting the approximate q^{VTI} from equation (F.11) into equations (F.8) and (F.9) and linearizing the resulting expressions for small offset-to-depth ratio ($|p_{int1} V_{P0}| \ll 1$, $|p_{int2} V_{P0}| \ll 1$), I obtain

$$p_{i1} = \frac{\sin\nu}{V_{P0}} + p_{int1} \cos\nu - \frac{(p_{int1}^2 + p_{int2}^2) V_{P0} \sin\nu (1 + 2\delta)}{2} , \tag{F.13}$$

$$p_{r1} = \frac{\sin\nu}{V_{P0}} - p_{int1} \cos\nu - \frac{(p_{int1}^2 + p_{int2}^2) V_{P0} \sin\nu (1 + 2\delta)}{2} . \tag{F.14}$$

The linearized equation for the vertical slowness components q and their partial derivatives $q_{,i} \equiv \partial q / \partial p_i$ ($i = 1, 2$) are derived from p_{i1} and p_{i1} following the procedure discussed in Chapter 3.

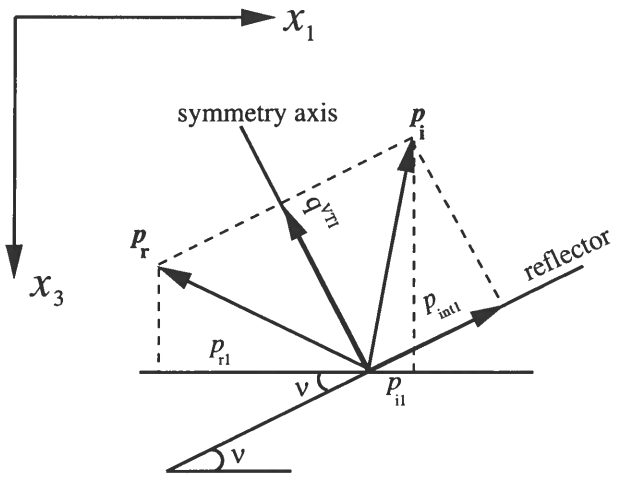

Figure F.1. Geometrical relationships between the slowness components of the incident and reflected P-wave in the dip plane of a TTI layer. The symmetry axis is orthogonal to the dipping interface. $\boldsymbol{p}_\mathbf{i}$ and $\boldsymbol{p}_\mathbf{r}$ are the in-plane slowness vectors of the incident and reflected waves, respectively; p_{i1} and p_{r1} are the horizontal slowness components of the incident and reflected waves. q^{VTI} is the slowness component along the symmetry axis, and p_{int1} is the slowness projection onto the interface in the dip plane.

If the asymmetry attributes are computed on a line with a fixed azimuth α, the relationship between p_{int1} and p_{int2} can be obtained by linearizing equation (F.5),

$$p_{int2} = p_{int1} \frac{\tan\alpha}{\cos\nu}. \tag{F.15}$$

Although this result is derived in the limit of weak anisotropy and small offset, numerical testing shows that it remains valid for arbitrary strength of the anisotropy and the full offset range.

To express the asymmetry attributes as a function of depth beneath the CMP location (z_{CMP}), I simplify equations (F.2) and (F.3) for the depth z_r of the conversion point using the weak-anisotropy, small-offset approximation:

$$z_r = z_{CMP}\left[\cos^2\nu - (1+4\delta)\,p_{int1}^2\,V_{P0}^2\,\sin^2\nu\right]. \tag{F.16}$$

The contribution of the P-leg to the time asymmetry can be obtained by substituting equation (F.1) into equation (4.1). I use equations (F.13) and (F.14) to find the partial derivatives of the vertical slownesses needed in equation (F.1), which yields the traveltime as a function of the slowness components p_{int1} and p_{int2} along the interface. Equation (F.15) then helps to obtain the time asymmetry factor on a line with azimuth α. After further linearization in the parameters ϵ, δ, and the combinations $|p_{int1}\,V_{P0}|$ and $|p_{int2}\,V_{P0}|$ using

symbolic software Mathematica, I find

$$\Delta t_P = 2\, z_{\text{CMP}}\, p_{\text{int1}} \sin\nu \left[1 + 2\delta + p_{\text{int1}}^2\, V_{P0}^2\, (1+4\epsilon) \left(1 + \frac{\tan^2\alpha}{\cos^2\nu}\right)\right] . \tag{F.17}$$

The approximate time asymmetry of the P-leg in equation (F.17) is expressed through the slowness p_{int1}, which cannot be estimated directly from surface reflection data. It is more practical to represent the asymmetry through the offset x_{PP} of the reflected PP-wave. Substituting the derivatives of the vertical P-wave slowness q_P into equations (F.6) and (F.7) and evaluating the result for the slownesses given by equation (F.13) and (F.14), I obtain the PP-wave offset (x_{PP}) from equation (F.4):

$$x_{PP} = p_{\text{int1}}\, V_{P0}\, z_{\text{CMP}}\, \sec\alpha \left[2 + 4\delta + p_{\text{int1}}^2 V_{P0}^2\, (1 - 4\delta + 8\epsilon) \left(1 + \frac{\tan^2\alpha}{\cos^2\nu}\right)\right] . \tag{F.18}$$

Equations (F.17) and (F.18) cannot be used in the strike direction ($\alpha = 90°$), where $p_{\text{int1}} = 0$. To remove this ambiguity, I replace p_{int1} with p_{int2} for $\alpha = 90°$ using equation (F.15).

It is convenient to expand Δt_P in a Taylor series in x_{PP} around zero offset:

$$\Delta t_P = \frac{\partial \Delta t_P}{\partial x_{PP}}\, x_{PP} + \frac{1}{6}\, \frac{\partial^3 \Delta t_P}{\partial x_{PP}^3}\, x_{PP}^3 + \ldots \tag{F.19}$$

Equation (F.19) contains only odd powers of offset because the terms even in x_{PP} do not contribute to the moveout asymmetry. Evaluating the partial derivatives in equation (F.19) using the chain rule applied to equations (F.17) and (F.18), I arrive at

$$\Delta t_P = \frac{\sin\nu\, \cos\alpha}{V_{P0}}\, x_{PP} + \frac{(1-2\delta)\, \sin\nu\, \cos^3\alpha}{8\, V_{P0}\, z_{\text{CMP}}^2} \left(1 + \frac{\tan^2\alpha}{\cos^2\nu}\right) x_{PP}^3 . \tag{F.20}$$

The linearized contribution of the S-leg to the time asymmetry factor can be found from the P-wave equation (F.20) using the general transformation rule valid in the limit of weak anisotropy (Tsvankin, 2001, p. 26):

$$V_{P0} \to V_{S0}, \quad \epsilon \to 0, \quad \delta \to \sigma ;$$

$$\sigma \equiv \frac{V_{P0}^2}{V_{S0}^2}\, (\epsilon - \delta) .$$

The above substitutions give the following expression for the corresponding S-wave asymmetry component Δt_S:

$$\Delta t_S = \frac{\sin\nu\, \cos\alpha}{V_{S0}}\, x_{SS} + \frac{(1-2\sigma)\, \sin\nu\, \cos^3\alpha}{8\, V_{S0}\, z_{\text{CMP}}^2} \left(1 + \frac{\tan^2\alpha}{\cos^2\nu}\right) x_{SS}^3 . \tag{F.21}$$

Although the common midpoints for the PP- and SS-waves processed by the PP+PS=SS method are not exactly the same, the difference between the values of z_{CMP} for Δt_P and Δt_S

can be ignored if the offsets are sufficiently small. Because of the typically large velocity ratios V_{P0}/V_{S0}, the offsets of the constructed SS-wave seldom exceed the reflector depth, so the term x_{SS}^3 in equation (F.21) can be neglected.

The total time asymmetry factor of the PS-wave can be found by substituting equations (F.20) and (F.21) into equation (F.1) and taking into account that the contributions of the P-and S-legs should have opposite signs (Chapter 3):

$$\Delta t_{PS} = \sin\nu \cos\alpha \left(\frac{x_{PP}}{V_{P0}} - \frac{x_{SS}}{V_{S0}}\right) + \frac{(1-2\delta)\sin\nu\cos^3\alpha}{8\,V_{P0}\,z_{CMP}^2}\left(1+\frac{\tan^2\alpha}{\cos^2\nu}\right)x_{PP}^3. \qquad \text{(F.22)}$$

Since the offsets x_{PP} and x_{SS} are related to each other, equation (F.22) can be further simplified by expressing x_{PP} through x_{SS}. Applying the transformation P-to-S rule to equation (F.18) yields the offset x_{SS} as a function of p_{int1} and azimuth α:

$$x_{SS} = p_{\text{int1}}\,V_{S0}\,z_{\text{CMP}}\,\sec\alpha\left[2+4\sigma+p_{\text{int1}}^2\,V_{S0}^2\,(1-4\sigma)\left(1+\frac{\tan^2\alpha}{\cos^2\nu}\right)\right]. \qquad \text{(F.23)}$$

Expanding x_{PP} in a Taylor series in x_{SS} around zero offset leads to

$$x_{PP} = \frac{\partial x_{PP}}{\partial x_{SS}}\,x_{SS} + \frac{1}{2}\frac{\partial^2 x_{PP}}{\partial x_{SS}^2}\,x_{SS}^2 + \frac{1}{6}\frac{\partial^3 x_{PP}}{\partial x_{SS}^3}\,x_{SS}^3. \qquad \text{(F.24)}$$

The derivatives in equation (F.24) can be determined from equations (F.18) and (F.23), which gives the following expression for the PP-wave offset:

$$x_{PP} = \frac{V_{P0}\,(1+2\delta)}{V_{S0}\,(1+2\sigma)}\,x_{SS} + \frac{(1-4\delta+8\epsilon)\,V_{P0}^3\cos^2\alpha}{8\,(1+2\sigma)^3\,V_{S0}^3\,z_{\text{CMP}}^2}\left(1+\frac{\tan^2\alpha}{\cos^2\nu}\right)x_{SS}^3. \qquad \text{(F.25)}$$

Substituting equation (F.25) into equation (F.22), I obtain the final expression for the time asymmetry factor in terms of the offset x_{SS}:

$$\begin{aligned}\Delta t_{PS} &= \frac{-2\sin\nu\cos\alpha}{V_{S0}}\,\chi\,x_{SS} \\ &+ \frac{(1+4\epsilon)\,V_{P0}^2\sin\nu\cos^3\alpha}{4\,(1+2\sigma)^3\,V_{S0}^3\,z_{\text{CMP}}^2}\left(1+\frac{\tan^2\alpha}{\cos^2\nu}\right)x_{SS}^3,\end{aligned} \qquad \text{(F.26)}$$

where $\chi \equiv (\sigma-\delta)/(1+2\sigma)$.

Appendix G

Approximate offset asymmetry factor for the PSV-wave in a dipping TTI layer

Here, I apply the approach described in Appendix F to obtain an approximation for the offset asymmetry factor of the PSV-wave in a TTI layer. Using equations (4.2) and (F.6), I can write the exact parametric equation for the projection of the offset asymmetry vector $\boldsymbol{\Delta x}_{PS}$ onto the x_1-axis as

$$\Delta x_{1_{PS}} \equiv \Delta x_{1_P} - \Delta x_{1_S} = z_r \left[q_{,P_i} + q_{,P_r} - (q_{,S_i} + q_{,S_r}) \right], \tag{G.1}$$

where q is the vertical slowness, $q_{,P_i} \equiv \partial q_P / \partial P_i$, $q_{,P_r} \equiv \partial q_P / \partial P_r$, $q_{,S_i} \equiv \partial q_S / \partial S_i$, and $q_{,S_r} \equiv \partial q_S / \partial S_r$; P_i and P_r are the horizontal slownesses for the incident and reflected legs of the P-wave, and S_i and S_r are the same quantities for the S-wave. The slowness vectors are related to each other by Snell's law at the reflection point.

To express the P-wave component of $\Delta x_{1_{PS}}$ as a function of the slowness projection onto the interface in the dip plane (p_{int1}), I evaluate the derivatives of the vertical slowness from Appendix F using equations (F.13) and (F.14):

$$\Delta x_{1_P} = z_r \left(q_{,P_i} + q_{,P_f} \right) = z_r \sec^2 \nu \tan \nu \left[1 + (2 + 8\delta) \, p_{\text{int1}}^2 \, V_{P0}^2 + \cos 2\nu \right]. \tag{G.2}$$

Of interest, equation (G.2) is independent of p_{int2}. The transformation rule (Tsvankin, 2001, p. 26) gives the corresponding equation for the S-wave:

$$\Delta x_{1_S} = z_r \sec^2 \nu \tan \nu \left[1 + (2 + 8\sigma) \, p_{\text{int1}}^2 \, V_{S0}^2 + \cos 2\nu \right]. \tag{G.3}$$

Substituting the P- and S-wave asymmetry contributions from equations (G.2) and (G.3) into equation (G.1) yields

$$\Delta x_{1_{PS}} = 2 \, z_r \, p_{\text{int1}}^2 \sec^2 \nu \tan \nu \left[(1 + 4\delta) \, V_{P0}^2 - (1 + 4\sigma) \, V_{S0}^2 \right]. \tag{G.4}$$

Expressing the depth of the reflection point z_r in terms of z_{CMP} using equation (F.16), I obtain

$$\Delta x_{1_{PS}} = 2 \, z_{\text{CMP}} \, p_{\text{int1}}^2 \tan \nu \left[(1 + 4\delta) \, V_{P0}^2 - (1 + 4\sigma) \, V_{S0}^2 \right]. \tag{G.5}$$

To find the factor Δx_{1PS} as a function of the SS-wave offset x_{SS}, I substitute p_{int1} from

equation (F.23):

$$\Delta x_{1_{PS}} = \frac{\tan\nu}{2\,z_{\rm CMP}} \left[\frac{(1+4\delta)\,V_{P0}^2}{(1+4\sigma)\,V_{S0}^2} - 1\right] x_{SS}^2 \cos^2\alpha\,. \tag{G.6}$$

The magnitude x_{PS} of the offset asymmetry vector for any azimuth α can be obtained by combining equations (F.4) and (F.5):

$$\Delta x_{PS} = \frac{\Delta x_{1_{PS}}}{\cos\alpha}\,. \tag{G.7}$$

Substituting equation (G.6) into equation (G.7) yields

$$\Delta x_{PS} = \frac{\tan\nu}{2\,z_{\rm CMP}} \left[\frac{(1+4\delta)\,V_{P0}^2}{(1+4\sigma)\,V_{S0}^2} - 1\right] x_{SS}^2 \cos\alpha\,. \tag{G.8}$$

In the presence of moveout asymmetry, the minimum traveltime of PS-waves in a CMP gather occurs at nonzero offset. As discussed in Chapter 3 and Tsvankin (2001, Appendix 5B), the offset $x_{\rm min}(\alpha)$ of the traveltime minimum corresponds to the PS ray for which the projections of the slowness vectors for the P- and S-legs onto the CMP line are equal to each other. The dip component of the slowness projection onto the interface can be found in the limit of weak anisotropy, small offset, and small dip as

$$p_{\rm int1}^{\rm min} = \frac{\sin\nu\,\cos^2\alpha}{2}\left(\frac{1}{V_{S0}} - \frac{1}{V_{P0}}\right). \tag{G.9}$$

Equation (G.9) contains no contribution of the anisotropic parameters and coincides with the expression for $p_{\rm int1}^{\rm min}$ in isotropic or VTI media given in Tsvankin (2001, Appendix 5D.2).

Evaluating the derivatives of the vertical slowness (see Appendix F) at $p_{\rm int1}^{\rm min}$ and substituting the result into equations (F.6), (F.7), and (F.4), I find the azimuthally varying offset of the traveltime minimum:

$$x_{\rm min}(\alpha) = \frac{z_{\rm CMP}}{2\,\cos\nu}\left[\frac{\sin\nu}{V_{P0}} - \frac{\sin\nu}{V_{S0}}\right]\left[V_{P0}\,(1+2\delta) + V_{S0}\,(1+2\sigma)\right]\cos\alpha\,. \tag{G.10}$$

Appendix H

Time asymmetry of PS-waves for arbitrarily anisotropic, heterogeneous media

In this appendix, I derive the small-offset approximation for the time-asymmetry factor in a heterogeneous, arbitrarily anisotropic medium. As in Chapters 3 and 4, the contribution of the S-wave leg to the time asymmetry can be expressed as

$$\Delta t_{SS} = t_{SS}(x_3, R) - t_{SS}(x_4, R), \tag{H.1}$$

where x_3 and x_4 are the S-wave receiver locations and R is the reflection point. Since the output points are arbitrary, it is possible to form a CMP gather for the SS-wave and expand Δt_{SS} for small offsets. This series contains only odd powers of x_{SS} because even powers do not contribute to the asymmetry:

$$\Delta t_{SS} \approx \left.\frac{\partial(\Delta t_{SS})}{\partial x_{SS}}\right|_{x=0} x_{SS} + \left.\frac{\partial^3(\Delta t_{SS})}{6\,\partial x_{SS}^3}\right|_{x=0} x_{SS}^3 + \cdots, \tag{H.2}$$

where the partial derivatives are evaluated for the zero-offset ray. Following the derivation of Tsvankin (2001, Appendix 5B) and ignoring reflection-point dispersal for small offsets, the derivative of Δt_{SS} can be written in the form,

$$\left.\frac{\partial \Delta t_{SS}}{\partial x}\right|_{x=0} = \left.\frac{\partial\,(t_1^{ns} - t_2^{ns})}{\partial x}\right|_{x=0}, \tag{H.3}$$

where t^{ns} is the traveltime along the *non-specular* raypath going through the reflection point corresponding to $x = 0$. Since the non-specular raypaths originate at the fixed reflection point, the gradient of the traveltime surface for each ray segment is equal to the corresponding slowness vector. Hence,

$$\frac{\partial \Delta t_{SS}}{\partial x} = p_{S0}, \tag{H.4}$$

where p_{S0} is the horizontal slowness corresponding to the zero-offset ray. After substituting equation (H.4) into equation (H.2), the linear term of Δt_{SS} can be expressed through zero-offset slope (p_{S0}),

$$\Delta t_{SS} = p_{S0}\, x_{SS}. \tag{H.5}$$

The contribution of the P-wave leg depends on the stationary points $[x^{(1)}, x^{(2)}]$,

$$\Delta t_{PP} = t_{PP}(x_1, R) - t_{PP}(x_2, R). \tag{H.6}$$

For a CMP gather of S-wave, the corresponding gather for P-wave may not be a CMP gather but it will have the same reflection point dispersal as that of the S-wave. Since the reflection-point dispersal can be ignored in obtaining the derivative of Δt_{SS}, it does not contribute to the derivative of Δt_{PP} either. Similar to the SS-wave, the leading-order term of Δt_{PP} can be expressed in terms of zero-offset slope for P-wave (p_{P0}),

$$\Delta t_{PP} = p_{P0}\, x_{PP}. \tag{H.7}$$

The time asymmetry of PS-waves (Δt_{PS}) can be obtained by combining equations (H.5) and (H.7). Let us expand Δt_{PS} for small S-wave offsets and retain only the leading order term,

$$\Delta t_{PS} = \left(p_{P0} \left. \frac{\partial x_{PP}}{\partial x_{SS}} \right|_{x_{SS}=0} - p_{S0} \right) x_{SS}, \tag{H.8}$$

where the derivative is evaluated for zero-offset SS ray. Evaluating the partial derivative using the chain rule and expressing it in terms of the NMO velocity and zero-offset traveltime (Hale, 1992) yields

$$\frac{\partial x_{PP}}{\partial p} = \frac{V^2_{\text{nmo,P}}\, t_{P0}}{2} \tag{H.9}$$

$$\frac{\partial x_{SS}}{\partial p} = \frac{V^2_{\text{nmo,S}}\, t_{S0}}{2}. \tag{H.10}$$

Combining equations (H.8)–(H.10) allows us to obtain the linear term in the time asymmetry in terms of pure-mode attributes,

$$\Delta t_{PS} = \left(p_{P0} \frac{V^2_{\text{nmo,P}}\, t_{P0}}{V^2_{\text{nmo,S}}\, t_{S0}} - p_{S0} \right) x_{SS}. \tag{H.11}$$

Equations H.9 and H.10 can also be used to expand x_{PP} in a Taylor series as a function of x_{SS}. Retaining only the linear term, we find

$$\begin{aligned} x_{PP} &= \frac{\partial x_{PP}}{\partial x_{SS}}\, x_{SS} \\ &\equiv \frac{V^2_{\text{nmo,P}}\, t_{P0}}{V^2_{\text{nmo,S}}\, t_{S0}}\, x_{SS}. \end{aligned} \tag{H.12}$$

Appendix I

Derivation of a constraint on pure-mode attributes for a homogeneous layer above a planar reflector

The elements of the data vector obtained from pure modes are the NMO velocities, zero-offset traveltimes, and reflection slopes for PP- and SS-waves. In general, all these quantities are independent of each other. For the special case of a homogeneous layer above a planar reflector, however, the pure mode attributes acquired in a vertical symmetry plane are related to each other by a constraint. The zero-offset traveltimes for P- and S-waves with the same CMP location (z_{CMP}) can be expressed using the parametric equation (Tsvankin & Grechka, 2002),

$$t_{P0} = 2\,\frac{z_{CMP}}{1+\tan\phi\, q_{,1P}}\,(q_P - p_{P0}\, q_{,1P}), \tag{I.1}$$

$$t_{S0} = 2\,\frac{z_{CMP}}{1+\tan\phi\, q_{,1S}}\,(q_S - p_{S0}\, q_{,1S}). \tag{I.2}$$

where p_{P0} and p_{S0} are the horizontal components of the slowness vector for the zero-offset ray (the subscripts "P" and "S" indicate the wave type), q is the vertical slowness, $q_{,1} \equiv \partial q/\partial p$, and ϕ is the dip of the reflector. For the zero-offset ray, the vertical slowness is related to the horizontal slowness as

$$q_P = \frac{-p_{P0}}{\tan\phi}, \tag{I.3}$$

$$q_S = \frac{-p_{S0}}{\tan\phi}. \tag{I.4}$$

Combining equations (I.1)–(I.4), the zero-offset traveltimes are obtained as

$$t_{P0} = \frac{-2\, z_{CMP}\, p_{P0}}{\tan\phi}, \tag{I.5}$$

$$t_{S0} = \frac{-2\, z_{CMP}\, p_{S0}}{\tan\phi}. \tag{I.6}$$

Taking the ratio of equations (I.6) and (I.6) yields a constraint on the pure mode attributes,

$$\frac{t_{P0}}{p_{P0}} = \frac{t_{S0}}{p_{S0}}. \tag{I.7}$$

Hence, the ratio of the zero-offset traveltime to the zero-offset reflection slope for pure modes is a constant that depends on the dip of the reflector and the depth beneath the CMP location.